University of Massachusetts Amherst
ScholarWorks@UMass Amherst

Doctoral Dissertations 1896 - February 2014

1-1-2003

Models and observations of the millimeter and submillimeter molecular line emission of bright-rimmed clouds.

Christopher H. De Vries
University of Massachusetts Amherst

Follow this and additional works at: https://scholarworks.umass.edu/dissertations_1

Recommended Citation

De Vries, Christopher H., "Models and observations of the millimeter and submillimeter molecular line emission of bright-rimmed clouds." (2003). *Doctoral Dissertations 1896 - February 2014*. 2001.
https://doi.org/10.7275/wctf-5e54 https://scholarworks.umass.edu/dissertations_1/2001

This Open Access Dissertation is brought to you for free and open access by ScholarWorks@UMass Amherst. It has been accepted for inclusion in Doctoral Dissertations 1896 - February 2014 by an authorized administrator of ScholarWorks@UMass Amherst. For more information, please contact scholarworks@library.umass.edu.

UMASS/AMHERST
312066 0288 1109 1

MODELS AND OBSERVATIONS OF THE MILLIMETER AND SUBMILLIMETER MOLECULAR LINE EMISSION OF BRIGHT-RIMMED CLOUDS

A Dissertation Presented

by

CHRISTOPHER H. DE VRIES

Submitted to the Graduate School of the
University of Massachusetts Amherst in partial fulfillment
of the requirements for the degree of

DOCTOR OF PHILOSOPHY

February 2003

Department of Astronomy

© Copyright by Christopher H. De Vries 2003

All Rights Reserved

MODELS AND OBSERVATIONS OF THE MILLIMETER AND SUBMILLIMETER MOLECULAR LINE EMISSION OF BRIGHT-RIMMED CLOUDS

A Dissertation Presented

by

CHRISTOPHER H. DE VRIES

Approved as to style and content by:

Gopal Narayanan, Chair

Ronald L. Snell, Member

Mark H. Heyer, Member

William J. Mullin, Member

Ronald L. Snell, Department Chair
Department of Astronomy

To my mother, taken too soon from this Earth.

ACKNOWLEDGMENTS

When you have been in graduate school as long as I have, which I hope that you never are, you end up meeting and befriending a lot of people. Some of these friends remained in Amherst for most or all of my graduate career, but many, due to the transient nature of the university, came and went as I trudged ever onward towards my degree. As I look back now I see what seem to be generations of friends who helped me become both the astronomer and the man that I am today. I would like to thank all of those people, and as is tradition I will start with my committee.

I would like to thank Gopal for arriving at UMass at just the right time to begin this research project. He helped me develop an exciting research project, provided support when I needed it, and some pressure too. Gopal is a good advisor, mentor, and friend. I would like to thank Ron for his helpful advice, and his ability to maintain an infectiously positive attitude. I would like to thank Mark for making me think critically about the shortcomings of the model. And I wish to thank Bill for agreeing to be my outside member, carefully working through my dissertation while he was on vacation, and trying to make me a better writer.

In the Astronomy department I found an abundance of colleagues who encouraged me throughout the past seven years. I thank the graduate students who came before me, Ted, Amy, Jimmy, and Jess; those who entered with me, Brandon, Kristen, and Lunming; and those who came after me including, Amber, Aimee, Dais, Dan, Dusan, and Irena for making the department a better place. I also thank the postdocs, Ned, Chris, Naomi, Andrew, and Cornelia for their encouragement and for enduring so many cafeteria lunches with me. I also wish to extend a heartfelt thanks to the

department staff, including Denise, Sally, Barb, Terri, Pam, and Karen for always laughing at my jokes and making my life so much easier.

I wish to express my appreciation to Nana, Stefanie, Susan, Richard, Yasin, Sangeeta, Mahmoon, Jennifer, ELBT, Dan, Jitu, Justine, and the rest of the GSS/GEO crew for giving me something else to throw myself into and opening my eyes to so many new experiences. My academic life would have been so dry without the jihads in which we engaged. I would also like to thanks friends who do not fit neatly into the above categories, including Andrew, Allen, Doris, Ray, Mary, Susan, Adam, Sejal, Kate, Greg, another Susan, and Sone. Thank you for the parties, movies, barbecues, distraction, and for putting up with me.

I would like to thank my mom and dad for always encouraging me. My dad has always been proud of my accomplishments and helped me move into so many of the apartments I have occupied in Amherst. My mom provided emotional support to me throughout my college and graduate carrer, as our phone bills will attest, up to the moment she died, and I will always miss her. I would like to thank my brothers, Matt and Tim for providing a connection to the outside world, for the occasional concert, and for understanding how busy I was.

Finally I would like to thank my wife Kim. I can be moody in even the best of times, and Kim has been with me through some of the most stressful times of my life. She has a source of constant support. She has encouraged and motivated me at times when I needed it most, with the exception of those six weeks she spent in China when I was feverishly working on writing this thesis. But she made up for that absence by washing my share of the dishes for a *very* long time and by listening to my rants the night before my defense. She is my love, and I could not have done this without her.

When I was leaving for graduate school I thought I would put my life on hold so I could quickly complete my studies. It is because of the many people I acknowledge

above that life was not put on hold, and although graduate school took longer than I expected, I got more out of it than I ever anticipated.

ABSTRACT

MODELS AND OBSERVATIONS OF THE MILLIMETER AND SUBMILLIMETER MOLECULAR LINE EMISSION OF BRIGHT-RIMMED CLOUDS

FEBRUARY 2003

CHRISTOPHER H. DE VRIES

A.B., CORNELL UNIVERSITY

Ph.D., UNIVERSITY OF MASSACHUSETTS AMHERST

Directed by: Professor Gopal Narayanan

We present the results of a comparison of new millimeter and submillimeter molecular line survey of bright-rimmed clouds, observed at FCRAO in the CO ($J = 1 \rightarrow 0$), $C^{18}O$ ($J = 1 \rightarrow 0$), HCO^+ ($J = 1 \rightarrow 0$), $H^{13}CO^+$ ($J = 1 \rightarrow 0$), and N_2H^+ ($J = 1 \rightarrow 0$) transitions, at the HHT in the CO ($J = 2 \rightarrow 1$), HCO^+ ($J = 3 \rightarrow 2$), HCO^+ ($J = 4 \rightarrow 3$), $H^{13}CO^+$ ($J = 3 \rightarrow 2$), and $H^{13}CO^+$ ($J = 4 \rightarrow 3$), and at the CSO in the HCO^+ ($J = 4 \rightarrow 3$) and $H^{13}CO^+$ ($J = 4 \rightarrow 3$) molecular line transitions with synthetic observations of a hydrodynamic shock driven triggered star formation model. We also present observations of three Bok globules done for comparison with the bright-rimmed clouds. We find that the appearance of the millimeter CO and HCO^+ emission is dominated by the morphology of the shock front in the bright-rimmed clouds. The HCO^+ ($J = 1 \rightarrow 0$) emission tends to trace the swept up gas ridge and overdense regions which may be triggered to collapse as a result of sequential star formation.

The morphologies of the observed bright-rimmed cloud are in good agreement with the our modeled emission. Five of the seven bright-rimmed clouds we observe seem to have an outflow, however only one shows the spectral line blue-asymmetric signature that is indicative of infall, in the optically thick HCO^+ emission. We also present evidence that in bright-rimmed clouds the nearby shock front may heat the core from outside-in thereby washing out the normally observed line infall signatures seen in isolated star forming regions. We find that the derived core masses of these bright-rimmed clouds are similar to other low and intermediate mass star forming regions.

TABLE OF CONTENTS

LIST OF TABLES

LIST OF FIGURES

CHAPTER 1

INTRODUCTION

1.1 Star Formation

Stars are one of the fundamental building blocks of the universe. Their very existence spurred humans to ponder the night sky, beginning an inquiry into the Universe in which we live which continues to this day. Eventually we learned that the stars around us are all distant versions of our own Sun. We learned that stars enrich the Universe around us, providing elements such as carbon and oxygen which are so necessary for our lives. A crowning achievement of astronomy has been our ability to unravel exactly how stars work, and to come up with a framework which accurately describes nearly all the stars we observe. We have even managed to describe the way stars evolve and burn out with tremendous accuracy. The one aspect of stars which we are still struggling to explain is how they form.

There are two basic modes of star formation. First, there is isolated star formation, where a gravitationally bound molecular cloud core collapses in an isolated environment until it forms a star. Typically these stars are thought to dissipate angular momentum through an interaction between the accretion disk and the magnetic field of the protostar (see Shu, Adams, & Lizano, 1987, and references therein). There are distinct stages that a forming star goes through in isolated star formation: (1) forming a gravitationally bound core within a molecular cloud, (2) gravitational collapse of the core, (3) the formation of a central star-like object, (4) dispersal of the remaining cloud material (see Ward-Thompson, 2002, and references therein). Although work within this theoretical framework for isolated star formation has been

developed for some time (Larson, 1969a; Shu, Adams, & Lizano, 1987), it may not fully explain the processes which occur when stars form in clusters.

The second mode of star formation is clustered star formation, where many cores within the same molecular gas envelope collapse into stars at approximately the same time. These stars are subjected to a much more chaotic environment in which the protostellar outflows and ionization fronts of nearby forming or recently formed stars can disrupt or enhance the ability of a particular core to collapse. The bulk of the stars in our galaxy are thought to have formed in clusters (Lada & Lada, 1991), and indeed the formation of high mass stars ($\gtrsim 3M_{\odot}$) is thought to occur almost exclusively in clusters. Within star forming clusters the protostellar nebulae are subjected to winds and turbulence which do not resemble the rather simple initial state of the Shu et al. (1987) model. The clumps within clustered environments constantly risk dissipation by turbulence, or compression and enhancement by a shock front. Once stars start to form they drastically change the nearby environment in ways that may both inhibit or encourage star formation. Star formation can be inhibited by ionizing radiation field of nearby stars, if a cloud core is close to a newly formed star the radiation field or stellar winds can ionize the cloud before it has a chance to condense into a star (Bertoldi, 1989; Vanhala & Cameron, 1998, hereafter VC). A radiation field of lesser intensity or a stellar wind of lower velocity can cause an unbound clump to become bound and collapse, or decrease the amount of time it takes for a clump to form a star by increasing the density (Bertoldi, 1989; VC).

It is important, in building a theoretical framework of star formation, to understand how interactions amongst forming stars affects both current and future star formation nearby. Triggering of star formation by the radiation-driven implosion is thought to be fairly ubiquitous as the gravitational timescale of a molecular cloud is shorter than the lifetime of an O-type star (Elmegreen, 1998). As a result, molecular gas is thought to be induced to collapse in the midst of pressures from HII regions,

stellar winds, and supernova explosions. These processes make the region more difficult to study. The kinematic signatures of ionization fronts and shock fronts along with the resulting bulk motion of the gas can make it difficult to distinguish regions of collapse from transient overdense regions which will not become gravitationally bound. In order to understand the processes which govern triggered star formation we must be able to identify those cores in which triggering is occurring.

1.2 Triggered Star Formation

Triggered star formation is the process by which star formation is initiated or accelerated through compression of a clump in a molecular cloud by a shock front (Elmegreen, 1992). Although a simple theoretical framework for the process of triggered star formation exists, only recently have numerical models become sophisticated enough to yield detailed comparisons with observations. Comparison of hydrodynamic shock induced star formation models to observations of potential triggered star formation regions is complicated by the fact that such regions can be very chaotic. Shocks, outflows, and core rotation all have kinematic signatures which may overwhelm the signatures associated with the triggering mechanism (Elmegreen, 1998).

There are three triggering mechanisms commonly discussed (Elmegreen, 1998). First, there is direct compression of pre-existing globules or density enhancements in a cloud ("globule squeezing"). This occurs when young HII regions begin expanding and start to interact with cloud clumps. The ionization fronts squeeze the cloud clumps and trigger star formation. Second, there is accumulation of gas into a dense ridge which collapses into dense cores via gravitational instability ("collect and collapse"). This occurs at the edges of older HII regions, where molecular gas accumulates into a dense ridge until kinematic instabilities within the dense ridge induce a self-gravitating clump which collapses to form a star or cluster of stars. The third mechanism is "cloud collisions." As two molecular clouds collide, the dense shocked gas between them is

another region in which gravitational instabilities can lead to triggered star formation. Triggered star formation also can be divided into three size scales (Elmegreen, 1998): small scale triggering, which involves the direct squeezing of preexisting clouds or globules by high pressure which nearly surrounds the whole cloud; intermediate scale triggering, which is the compression of a cloud from one side, leading to a dense ridge of gas which eventually collapses or recollects into denser cores in which stars form; and, large scale triggering, which is an accumulation of gas into an expanding shell or ring which partially surrounds the pressure source, a star or supernova. Examples of small scale triggering include proplyds and small cometary globules. Examples of intermediate scale triggering could be the compression of molecular cloud material by a bipolar outflow, and of large scale triggering includes star formation on the shell formed by a supernova.

The study of triggered star formation also has implications in the study of the creation of our own solar system. Cameron & Truran (1977) found an overabundance of the daughter product of ^{26}Al decay (^{26}Mg) in meteorites relative to the stable ^{27}Al isotope. ^{26}Al is a very short-lived radionuclide with a halflife of 750,000 yr. They attribute this abundance to the presence of short-lived radionuclides in the early solar system, which may have been injected into the solar nebula by a nearby supernova. In order for such a short-lived radionuclide to have been introduced into the solar nebula it is assumed that the source of the radionuclide, a supernova, must have been near to the solar neighborhood, or that they were produced locally by cosmic ray irradiation (see Podosek & Nichols, 1997, and references therein). It is assumed that the relative physical and temporal proximity of the supernova explosion which may have produced ^{26}Al as well as other short-lived radionuclides which existed in our early solar nebula is not coincidence. Such a nearby supernova may have triggered the collapse of our solar nebula, carrying the short-lived radionuclides into the solar nebula via injection by Rayleigh-Taylor instabilities (Boss & Foster, 1997). This is a

compelling reason for our study of triggering, as it may help us understand our own solar system.

Triggering on all size scales can be the result of a gravitational instability caused by the density enhancement of a shock front moving through a molecular cloud. A shock front can accelerate the collapse of a clump, thus triggering star formation, in three ways (Elmegreen, 1992). First, the shock increases the density of the gas on small scales, which increases the collapse rate in proportion to $n^{1/2}$ for a density n. Second, the rate of magnetic diffusion is increased by a factor of $n^{1/2}$ to $n^{5/2}$ depending on the angle between the shock front and the magnetic field. Third, shocks tend to move gas parallel to the magnetic field because the magnetic resistance is lowest in that direction. This results in a density increase in the gas, but without a change in the rate of rotation, thus stripping away angular momentum. Observing these effects however, is made more difficult by the fact that the regions which have winds and shock fronts are often kinematically complicated regions in which the formation of any particular star is difficult to detect. We have selected a source catalog of bright-rimmed clouds in order to alleviate this confusion somewhat.

1.3 Examining Triggering Through Observations of Bright-Rimmed Clouds

Bright-rimmed clouds (Sugitani, Fukui, & Ogura, 1991, hereafter SFO) are molecular clouds that border expanding HII regions, and are considered to be good laboratories of the process of triggered star formation (Sugitani & Ogura, 1994) by radiation-driven implosion (Bertoldi, 1989). At the boundary between the ionized gas within the Stromgren sphere, and the molecular cloud is an ionization front, which shows up as the bright rim identified by SFO. Embedded near the rim, and just within the molecular cloud in each of these sources is an Infrared Astronomical Satellite (IRAS) source. The fact that the ionization front is collecting gas into a

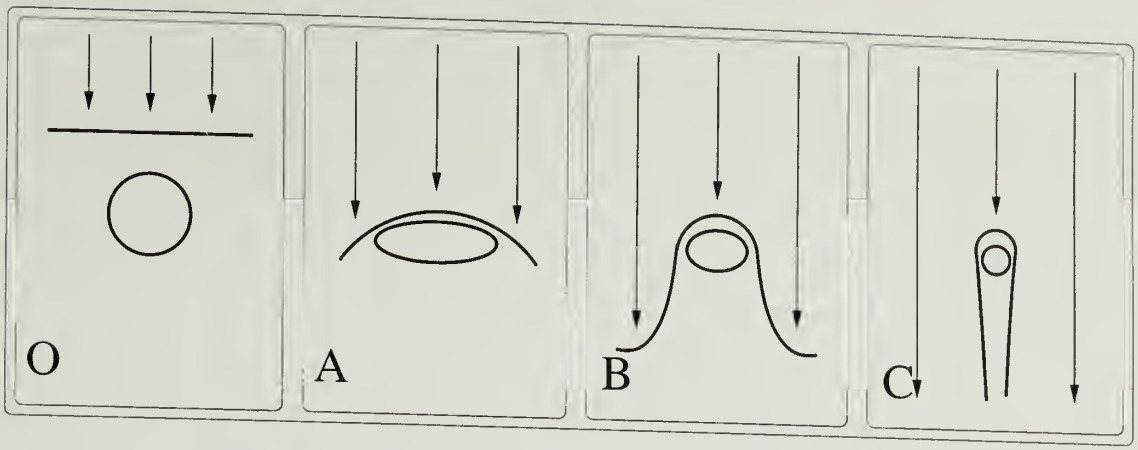

Figure 1.1 A planar shock front approaching a dense clump (0). As the shock front hits the clump it slows down, and the clump flattens out, this corresponds to the type A morphology. The clump contracts under the influence of the shock front, and shields the gas behind it from ionization as the shock front passes, this corresponds to the type B morphology. The clump continues to contract and shield the gas behind it, forming a cometary morphology, this corresponds to the type C morphology.

ridge or core in many of these sources makes them excellent candidates for the globule squeezing or collect and collapse mode of triggered star formation (Elmegreen, 1992, 1998). These clouds are also divided into three morphological types, shown schematically in Figure 1.1. The first is type A, which has a moderately curved rim, and looks much like a shield in three dimensions. The second is type B, which has a more tightly curved rim near the head of the cloud, but which tends to broaden near the tail. Type B is also known as an elephant trunk morphology. The third is type C which has a very tightly curved rim and a well defined tail. Type C is often called a cometary cloud. The shock induced collapse models of VC as well as observations of the expanding ionization front of the Orion OB 1 association (Ogura & Sugitani, 1998) suggest that these morphological types of bright rimmed clouds may actually be a time evolution sequence with clouds evolving from type A through type B to type C.

The Bright-rimmed clouds which we have observed are excellent candidate sources for observing radiation-driven implosion as they contain one Young Stellar Object (YSO) and one shock front which is moving approximately perpendicular to the line

of sight of the observer. What makes this study particularly compelling now is that our observational capabilities are improving to the point where we can start to do surveys of these sources using several millimeter and submillimeter molecular tracers. At the same time, numerical studies are starting to become accurate enough to model shock triggered collapse (Boss, 1995; Foster & Boss, 1996; Foster & Boss, 1997; VC). These studies have found that shocks with velocities less than 45 km s^{-1} can cause cores to collapse, but fast shocks ($>$ 100 km s^{-1}) tend to destroy the principal cooling molecules, leading ultimately to the destruction of the cloud (VC). These models also yield an appreciable number of binary and multiple star systems, which are common in our galaxy, yet difficult to form by spontaneous, isolated star formation. The VC models tend to reproduce characteristics of observed cometary clouds thought to be small scale triggered star formation regions (Elmegreen, 1992, 1998).

In order to perform a detailed study of sites of triggered star formation, that can be compared to the hydrodynamic models of VC, we conducted a survey of bright-rimmed clouds identified by SFO. Bright-rimmed clouds are a good stepping stone towards understanding triggering. They have a simple geometry which can be easily understood. They do not possess the multiple winds and shock-fronts of star formation in clusters. And they resemble the evolving morphology of wind driven collapse (VC). In this work we probe the molecular gas using various molecular transitions in the millimeter and submillimeter wavelengths in order to probe molecular gas in different physical states to build up a picture of how the molecular cloud reacts to the shock front. We also probe the hydrodynamic models by making synthetic observations of them using Local Thermodynamic Equilibrium (LTE) and Large Velocity Gradient (LVG) radiative transfer codes we developed. Through a comparison of our real and synthetic observations we attempt to rate the success of hydrodynamic models at explaining simple triggered star formation. In addition, the synthetic observations will help guide our real observations of bright-rimmed clouds in looking for

predicted structures. We then will be able to apply the lessons we learn in this study to improving the models as well as to studying more complex star formation regions.

1.4 The Classic Blue-shifted Asymmetric Signature of Infall

As we look at both our observed and modeled spectral line profiles, we make comparisons to profiles that have been previously observed in infalling cloud cores. One of the most common spectral signatures of an infalling cloud core is the "classic" asymmetric blue line profile. This occurs whenever an optically thick transition is observed in an infalling cloud core which is not resolved by the telescope beam. The infalling core must also have both a density and excitation temperature gradient which peaks in the center and falls off towards the edges. The origin of the line asymmetry is presented in Figure 1.2. The spherically symmetric, infalling cloud core is divided into hemispheric layers numbered 1 through 8, with layer 1 being closest to the observer, and layer 8 being farthest away. Infall velocities increase as the radius decreases, which is in agreement with free-fall models of collapse (Shu, 1977). Within a given layer, the density, temperature, and velocity are constant. Emission from layers 1 through 4, on the near side of the protostar, appear redshifted to the observer. The emission from layers 5 through 8, on the far side of the protostar, appear blueshifted. The emerging line profile from the collapsing core is shown on the bottom left of the figure. The line is broken into velocity bins, and the layer responsible for the emission in that bin is indicated by its number. The emission from the inner layers on the near (redshifted) side of the protostar is partially absorbed by the cooler foreground layers before reaching the observer. The emission from the far (blueshifted) side of the protostar is not absorbed by the foreground layers because the foreground layers are either hotter than the layer in which the emission originated or at a substantially different velocity than the layer in which the emission originated. Therefore, the

redshifted emission is preferentially absorbed giving the emerging line profile a blue asymmetric self-absorbed signature.

The "classic" asymmetric line profile signature has been used extensively to study infall (Snell & Loren, 1977; Zhou, 1992, 1995; Mardones et al., 1997; Gregersen et al., 2000). However, as we will discuss in §4.2, this signature becomes less effective at identifying regions of infall when we survey kinematically complex regions. Narayanan et al. (2002) have shown that rotation and outflow can also produce blue asymmetric line profiles. It is sometimes possible to distinguish between infall, rotation, and other effects which may result in an asymmetric line profile by observing the asymmetry in its spatial context on the sky. One way of doing this to to create a centroid velocity map. A centroid velocity is defined as the velocity which divides the area under a spectral line profile into two regions of equal area. Narayanan et al. (2002) find that a rotating and infalling cloud has a "blue-bulge" signature in the centroid velocity map of self-absorbed line profiles such as HCO^+ and CS. We will create centroid velocity maps in order to place this aspect of the spectral line profile shape into a spatial context.

1.5 Organization of this Work

In this thesis, we report on our millimeter and submillimeter molecular line observations of bright-rimmed clouds and on comparisons of these observations with the hydrodynamic models of VC. The organization of this work is as follows. In Chapter 2, we present the VC models and describe the radiative transfer calculations we performed to generate synthetic observations of these models. We will generate spectral line data as well as standard observational products such as integrated intensity maps and compare the features we observe with the features present in the input models. In Chapter 3, we present our new observations of seven bright-rimmed clouds from the SFO catalog of bright-rimmed clouds, as well as observations of three

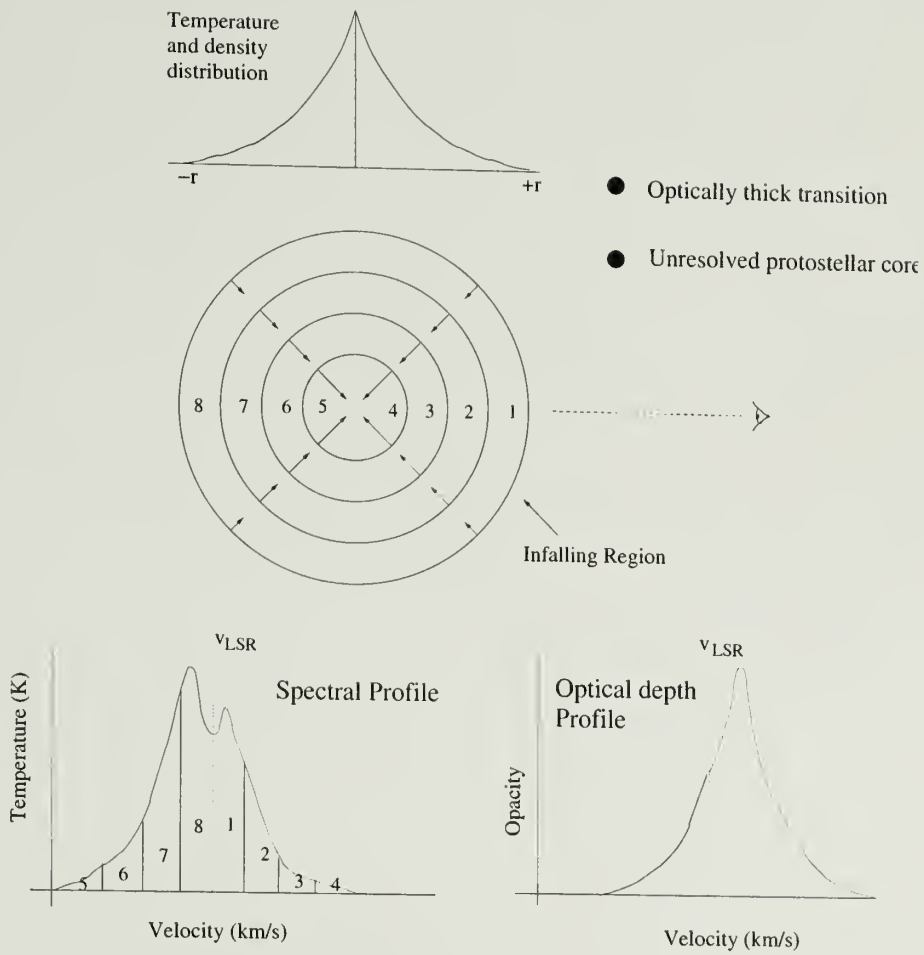

Figure 1.2 Classic blue-shifted asymmetric signature of infall. A schematic view illustrating the formation of the asymmetric blue-shifted line profile towards an infalling cloud core.

Bok globules for comparison. We also present standard observational parameters, and characteristics such as infall signature which is found in several star forming cores. In Chapter 4, we compare the models and observations both qualitatively and quantitatively and identify discrepancies which may indicate shortcomings in the model or discrepancies in our assumptions regarding the physical or chemical conditions in these regions. Finally in Chapter 5, we present the conclusions and outline strategies to improve upon this work.

CHAPTER 2
HYDRODYNAMIC MODELS OF WIND TRIGGERING

2.1 Introduction

The process of triggered star formation can be better understood by comparing models with observations of candidate triggered star formation regions. Theoretical models of normal star formation have been formulated and tested for some time, always pushing the envelope of available computing power. Larson (1969a) created a numerical model of a spherically symmetric collapsing protostar assuming an initially isothermal sphere and used this model to derive the evolution of the spectral energy distribution of the protostar as it evolves (Larson, 1969b). Shu (1977) refined this isothermal collapse model, providing a simple recipe for spherically symmetric protostellar regions. This model while being simplistic is still used as a starting point in many test cases. As the modeling of star formation moved beyond the one dimensional paradigm, dealing with the angular momentum within a collapsing protostar became a problem (Shu et al., 1987). Magnetic interaction between the protostar and an accretion disk was postulated to alleviate this problem. This interaction even helped to explain the presence of jets and bipolar outflows around young stars (Shu et al., 1988).

Attempts to model triggered star formation have also been going on for some time. Bertoldi (1989) developed an analytic model to model the photoevaporation of an interstellar cloud by radiation-driven implosion. This model is quite applicable to the SFO catalog of bright-rimmed clouds which are all being photoevaporated by an ionization front. Bertoldi & McKee (1990) created an analytic model of an equilibrium

cometary cloud, also exposed to the ionizing radiation of a new star. They found that the shape of the resulting cometary cloud depends on the cloud mass, the ionizing flux, and the adiabatic index of the gas. They also found that the rocket effect of the photoevaporating gas causes the cloud to accelerate away from the newly formed star. Lefloch & Lazareff (1994) used a two dimensional hydrodynamic model to simulate the formation, evolution, and morphology of cometary globules formed by radiation-driven implosion. They found that the process typically entails two stages: First, collapse in a short timescale (10^5 yr) with maximal compression occurring early in this phase. After maximal compression the globule tends to undergo free expansions and re-compressions. This stage typically lasts approximately one tenth of the globule's lifetime. Second, a quasi-static cometary phase sets in. The cometary phase is typically terminated when the globule becomes overwhelmed by small scale instabilities and is destroyed. Two observed regions of radiation-driven implosion seem to agree fairly well with the Lefloch & Lazareff (1994) predictions (Lefloch & Lazareff, 1995; Lefloch et al., 1997).

2.2 Hydrodynamic Models of Shock-Triggered Star Formation

Within a collapsing molecular cloud which is forming a star there are several important forces. Like many astronomical phenomena, gravity is very important, however the densities are so great that pressure is also important, so these regions must be treated hydrodynamically. In addition to gravity, magnetic fields also play an important role (Shu et al., 1987) so a full treatment of these regions requires magneto-hydrodynamic simulations.

There are two fundamental numerical techniques which have been developed to numerically simulate hydrodynamics. The first technique involves solving these equations on a grid or series of grids. This method allows us to solve for the physical

conditions within every cell of the grid, but it does not easily allow us to follow collapse to very small resolutions and high density. A more recent implementation of the grid method, which allows for varying resolution during an integration is adaptive mesh refinement (AMR) which has been used to study molecular cloud collapse (Truelove et al., 1998). A second numerical technique, Smoothed Particle Hydrodynamics (SPH) (see Monaghan, 1992, and references therein), allows us to follow collapse over a much wider dynamic range of densities and resolutions. The drawback is that regions of relatively low density compared to the peak density are not as well sampled. As we are interested in following the process of collapse the SPH method seems more suitable than the grid method.

VC have developed a hydrodynamic code for studying molecular cloud collapse, star formation, and wind-blown triggering. It does not simulate the motion of an ionization front into a molecular cloud core, which is the situation we observe in bright-rimmed clouds. There are several reasons why we think that the VC wind-blown triggering model is a valid model to study and compare with the radiation driven implosion which takes place in bright-rimmed clouds. The wind-blown model creates a shock front which moves into the molecular core at a velocity on the order of several km s^{-1} just as the ionization front moves into the molecular core in bright-rimmed clouds. The morphologies of the VC wind-blown triggering models are the same as the bright-rimmed cloud morphologies. The VC wind-blown model simulates the dissociation and ionization of hydrogen which occurs at the shock front, resulting in the molecular gas ridge which is also observed in bright-rimmed clouds. The VC wind-blown triggering model also contains several features that make it particularly adept at studying molecular and atomic gas processes over a large range of temperatures and densities.

The pressure in the hydrodynamic equations is derived from the equation of state. It is important to accurately model the equation of state as fluctuations in the adi-

abatic index below $\gamma = 4/3$ result in an instability which encourages the cloud to collapse. VC assume local thermodynamic equilibrium, and solve a chemical network of 39 elements and 316 ions using the Saha equation. Their calculations assume an equilibrium mix between the ortho and para states of hydrogen. Figure 2.1 shows the adiabatic index in the VC models as a function of temperature at several densities.

VC account for molecular cooling, grain cooling, and atomic line cooling in their hydrodynamic models. They do so under the assumption of thermodynamic equilibrium and low optical depth. At high densities the assumption of low optical depth is not valid, while in the range of densities followed in the models this effect should be negligible (VC). Below approximately 2000 K molecular cooling dominates, however above 2000 K atomic line cooling and dust grain cooling tend to dominate.

Magnetic fields are important in the study of molecular cloud collapse and star formation. The VC hydrodynamic model includes the effect of magnetic fields using a magnetic pseudofluid (Cameron, Vanhala, & Höflich, 1997). The underlying assumption in this case is that the magnetic field is fully tangled and frozen into the gas. This reduces the full magnetohydrodynamic calculations by adding scalar terms for the magnetic energy and pressure that vary as the 4/3 power of the density.

The density ratio across a standard shock front is usually defined as the ratio $(\gamma + 1)/(\gamma - 1)$, however in these shock fronts the adiabatic index changes as a function of temperature and density. VC solve the Rankine-Hugonoit jump equations directly in order to follow the physical condition changes across the shock front. The density jump VC simulate can approach a factor of 40, however the magnetic field tends to lower this factor. The density jump nears this peak in the 10 to 70 km s^{-1} shock velocity range, which is on the order of stellar winds and certain supernova shock front velocities.

The VC simulations consist of a spherically symmetric core embedded in a cloud which is impacted by a cylindrical stream of shock particles. The number of particles

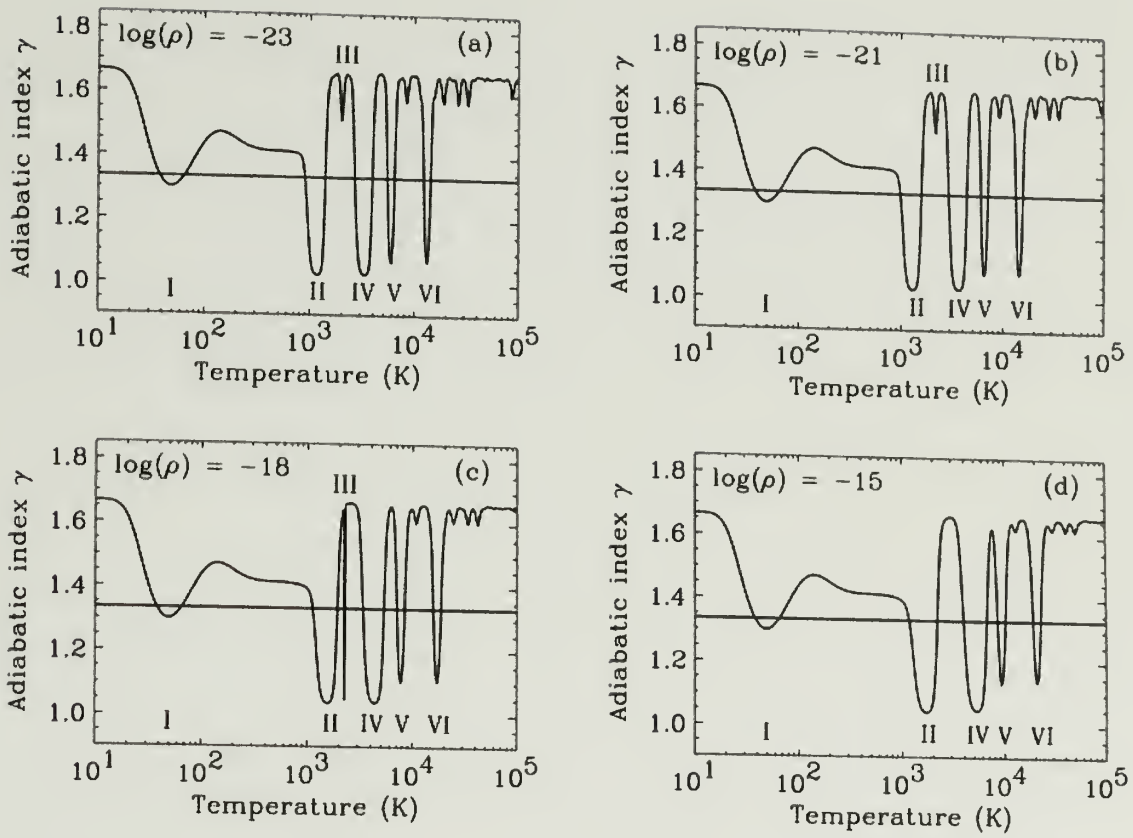

Figure 2.1 Adiabatic index γ in the VC models as a function of temperature at the densities (*a*) 10^{-23} g cm^{-3}, (*b*) 10^{-21} g cm^{-3}, (*c*) 10^{-18} g cm^{-3}, (*d*) 10^{-15} g cm^{-3}, assuming an equilibrium mix of the ortho and para states of hydrogen. The major features are marked in the figure by the roman numerals I–VI, and they correspond to the excitation (I) and dissociation (II) of hydrogen molecules, the dissociation of CO molecules (III), the ionization of hydrogen atoms (IV), and the single (V) and double (VI) ionization of helium atoms. The smaller wiggles at high temperatures are due to multiple ionizations of C, N, and O atoms. The line at $\gamma = 4/3$ marks the boundary between stable ($\gamma > 4/3$) and unstable ($\gamma < 4/3$) systems. Figure and caption are courtesy of VC.

making up the core, and those making up the background cloud remains fixed an numbers approximately 15,000 depending on the simulation. As the stream impacts the core more particles are continuously added to the back of the stream, however as stream particles move beyond the region of interest they are recycled into the back of the stream. In most cases a total of 20,000 to 40,000 particles are involved in each simulation. The core is created by imposing an artificial force on the system which guides the particles into the desired profile. The benefit of this method is that the core density profile rejoins the density of the background gas, 10^{-21} g cm^{-3}, without any discontinuities. This artificial force is removed when the simulation begins, and since the core is gravitationally unbound it initially begins to expand before the shock front begins to effect it. Without the introduction of the shock front the core would dissipate and no star formation would occur.

2.3 Modeling the Radiative Transfer in Hydrodynamic Models

Although VC provide a detailed simulation of the physical evolution of wind-blown triggered star formation, one cannot directly compare the simulation with observations. The VC models simulate the temperature, hydrogen density, the fraction of hydrogen atoms in molecular hydrogen, and the velocity at each point in the simulation. We do not directly observe these quantities, although we do try to infer them. We typically observe the millimeter and submillimeter emission of the rotational transitions of molecular gas tracer molecules such as CO. In order to facilitate a better comparison between the VC models and our observations (see Chapter 3) we have developed a method for simulating the rotational emission of our tracer molecules and creating synthetic observations of a simulation whose physical parameters are known. We do this in three steps: First we populate the rotational excitation quantum levels of the molecule of which we wish to create synthetic observations. We do this in one

of three ways — (i) under the assumption of local thermodynamic equilibrium (LTE), or (ii) we assume that there is a large velocity gradient (LVG) decoupling regions of the simulation radiatively from each other, or (iii) we perform a full Monte Carlo simulation of the radiative transfer. Second, we project the simulation on the sky plane by rotating it into the orientation we want and moving it to the distance at which we wish to observe it. Third, we integrate the total intensity and optical depth along the line of sight in order to build a spectrum at every point in the sky. We also convolve this to the beam size we desire. These steps are discussed in detail below.

2.3.1 Calculating the Rotational Quantum Level Populations

We have three methods of calculating the level populations. Why do we use so many different methods? Why not just use the most accurate method? Unfortunately as the accuracy of the method increases, the computational cost also increases and becomes prohibitive for use on the models we have and with the computers we have at our disposal. Fortunately computational capacity is increasing at such a rate that soon we will be able to use the most accurate method, Monte Carlo, on large simulations. For this work we have used the Monte Carlo method only on spherically symmetric models. The simplest model, LTE, we have applied to all the VC hydrodynamic models for all the observed transitions, while the LVG model has been applied to all the HCO^+ and $H^{13}CO^+$ transitions of the VC models.

The basic equation that governs the excitation of the molecular tracers is the statistical equilibrium equation, which is

$$\sum_j n_j C_{ji} - n_i \sum_j C_{ij} - n_i \sum_{j<i} A_{ij} + \sum_j n_j \frac{B_{ji}}{4\pi} \int I_\nu \phi_{ji} d\nu d\Omega - n_i \sum_j \frac{B_{ij}}{4\pi} \int I_\nu \phi_{ij} d\nu d\Omega = 0. \tag{2.1}$$

This equation expresses the equilibrium condition where collisional excitation, collisional de-excitation, spontaneous de-excitation, stimulated excitation, and stimulated de-excitation are all balanced such that the fraction of molecules at any particular

rotational quantum level is constant. In the equation above n_i is the density of the molecular tracer in the rotational quantum level $J = i$, A_{ij} is the spontaneous emission rate or Einstein A coefficient, B_{ij} is the stimulated emission or absorption rate coefficient also known as the Einstein B coefficient, C_{ij} is the collisional rate coefficient, I_ν is the radiative intensity at frequency ν, ϕ_{ij} is the profile function of the $J = i \rightarrow j$ transition, and Ω is the solid angle. The difficulty in solving this equation is that the level population is necessary in order to determine the radiative intensity, I_ν. However in order to determine the level population we need to know the radiative intensity. Therefore this equation typically is solved in an iterative fashion.

2.3.1.1 LTE

The simplest assumption we can make in populating the rotational levels of the molecular tracer is that the molecule is in thermodynamic equilibrium. This means that collisional excitation and de-excitation dominates over spontaneous de-excitation and stimulated excitation and de-excitation. This reduces equation 2.1 to

$$\sum_j n_j C_{ji} - n_i \sum_j C_{ij} = 0. \tag{2.2}$$

At densities higher than the critical density for each transition this is a valid assumption. The critical density is defined as

$$n_{\text{crit}} = \frac{A_{ul}}{C_{ul}}, \tag{2.3}$$

that is the density at which the collisional de-excitation and spontaneous de-excitation rates are equal. The critical density varies for each transition and is also a dependent on the gas temperature through the dependence on the collisional coefficient C_{ul}. We present the critical densities of the molecular transitions we survey in Table 2.1. The critical densities of the HCO^+ transitions are much higher than the CO transitions.

Table 2.1. Critical Densities

Transition	$n_{\rm crit}$ ($\rm cm^{-3}$)
HCO^+ ($J = 1 \rightarrow 0$)	1.4×10^5
HCO^+ ($J = 3 \rightarrow 2$)	2.5×10^6
HCO^+ ($J = 4 \rightarrow 3$)	6.4×10^6
CO ($J = 1 \rightarrow 0$)	2.4×10^3
CO ($J = 2 \rightarrow 1$)	1.0×10^4

Note. — These critical densities are calculated under the assumption of a kinetic gas temperature of 30 K. HCO^+ collisional coefficients were obtained from Flower (1999). CO collisional coefficients were obtained from Flower (2001). Molecular parameters were obtained from Pickett et al. (2000, 1998).

Typically the molecular hydrogen densities within molecular clouds are around 10^3 $\rm cm^{-3}$ or so, and in the centers of a condensing cloud the molecular hydrogen density can rise to around 10^7 $\rm cm^{-3}$. The assumption of thermodynamic equilibrium is generally more valid for the CO transitions than the HCO^+ transitions in the regions we are observing and theoretically modeling.

The equilibrium equation can further be simplified using the relation between collisional excitation and de-excitation,

$$C_{lu} = \frac{g_u}{g_l}\, e^{-\frac{h\nu}{kT}} C_{ul}, \tag{2.4}$$

where $u > l$, g_i is the degeneracy of the $i^{\rm th}$ energy level, and T is the temperature. By combining these equations we find that the density of the molecular tracer in the rotational quantum state $J = i$ is

$$n_i = n \frac{g_i \exp\left(\frac{-E_i}{kT}\right)}{\sum_j g_j \exp\left(\frac{-E_j}{kT}\right)}, \tag{2.5}$$

where n is the total density of the tracer and E_i is the energy of the $J = i$ quantum level. Since these relations do not depend on the radiation field, we can solve for the quantum level populations using this method without the need for an iterative process. However the assumption of thermodynamic equilibrium is rarely valid for molecular tracers in the interstellar medium.

2.3.1.2 LVG

A slightly more computationally intensive solution is to solve the statistical equilibrium equation (2.1) without assuming that the collisional terms dominate, but to ignore the radiation field that passes between individual cells of the simulation space. We assume the energy density within the cell to be composed both of emission arising from within the cell and background emission. The relative contribution of background emission and emission from within the cell is governed by an escape probability, β. The energy density in the cell is given by the expression

$$u = \frac{4\pi}{c} \left[\beta I_{bg} + (1 - \beta) S\right], \tag{2.6}$$

where I_{bg} is the mean intensity of the background emission, and S is the mean intensity of emission arising within the cell, otherwise known as the source function. The escape probability, β is calculated according to the Sobolev approximation, also known as the Large Velocity Gradient (LVG) approximation (Scoville & Solomon, 1974; Rybicki & Hummer, 1978). An underlying assumption of this method is to assume that the optical depth, τ, across the cell is a function of the velocity gradient, $\frac{dv}{dz}$, across the cell. This assumption arises from the fact that if a gradient does exist the emission from one location will be absorbed only within a region of gas at approximately the same velocity. Once a photon enters a region of gas at a significantly different velocity than the gas at which it was emitted, it has a very low probability of being absorbed

and therefore is likely to escape the cloud. The expression for the optical depth as a function of velocity gradient is

$$\tau = \frac{hc}{4\pi}\left(\frac{dv}{dz}\right)^{-1}(n_l B_{lu} - n_u B_{ul}) \tag{2.7}$$

(Rybicki & Hummer, 1978).

In the case of our models we assign a turbulent velocity width to each cell. We do this because observations of molecular clouds have shown that the lines are much broader than the expected thermal widths. We select a turbulent width of 0.25 km s^{-1} for the VC models on which we chose to make synthetic observations as this yields a fairly good match to observations. This turbulent velocity width becomes our dv. Strictly speaking, dv should be some measure of the velocity gradient across our cell, however we have used the approximation that the velocity gradient in each cell is 0.25 km s^{-1}. In a future iteration of the LVG model we will rectify this situation and assign a measured velocity gradient for each cell. Since our models always involved cubic cells we chose the length across any dimension of the cell as dz. The escape probability, β can be derived from the optical depth using the expression

$$\beta = \frac{1}{4\pi}\int \frac{1 - e^{-\tau}}{\tau}\, d\Omega \tag{2.8}$$

(Rybicki & Hummer, 1978). When β is inserted into equation 2.6 we can derive the energy density within the cell, which is related to the intensity through the equation

$$u = \frac{1}{c}\int I_\nu d\Omega d\nu. \tag{2.9}$$

From this equation we derive the mean intensity, $\frac{1}{4\pi}\int I_\nu d\Omega$ which we can use in equation 2.1 to find the population at each rotational energy level. Of course changing

the level populations changes the optical depths for each transition requiring us to iteratively approach the correct level population.

Since several iterations are typically required in order to for the level populations to converge, the LVG method is more computationally intensive than the LTE method. What we gain from this process is a better solution for regions in which collisional processes do not dominate. Typically in low density regions, such as molecular clouds, collisional processes do not dominate and the full statistical equilibrium problem must be solved. The LVG method described here does not account for the radiative coupling between cells in the simulation. We assume that emission within one cell is either absorbed within that cell or escapes out of the cloud, but in regions where there is not a large velocity gradient photons emitted in one cell can be absorbed into another cell. In order to explore the radiative coupling of cells a much more intensive calculation is required.

2.3.1.3 Monte Carlo

The Monte Carlo is the most numerically intensive radiative transfer model we use. The basic procedure involves creating photon packets either at random locations within the simulation or at random location on the boundary of the simulation and allowing these photon packets to propagate along random vectors through the simulation. As the photon packets interact with each cell they excite and de-excite the various levels through stimulated absorption and stimulated emission. In addition the packets pick up extra photons as a result of spontaneous emission within the cell. As the number of photon packets included in the simulation increases the level populations of the individual cells approach convergence. This technique has been discussed and implemented several times for use in calculating the level populations of molecular clouds (Bernes, 1979; Park & Hong, 1995; Park et al., 1996; Juvela, 1997; Hogerheijde & van der Tak, 2000), however it is still too computationally expensive

to model the VC three dimensional hydrodynamic models using this method. We do however use the one dimensional Monte Carlo radiative transfer model of Hogerheijde & van der Tak (2000) both to check the accuracy of our LVG and LTE methods as well as in an illustrative case in Chapter 4.

We compare the results of each type of model on a spherically symmetric case of an isothermal infalling sphere (Shu, 1977). The sphere has a maximum molecular hydrogen density at its center of 2.5×10^5 cm^{-3} and tapers to a density of 1×10^3 cm^{-3} at the edge. In the LTE, LVG, and Monte Carlo cases we use a sphere of 4×10^{17} cm in radius with 50 logarithmically spaced cells. We modeled the level population of the HCO^+ molecule at two abundances relative to molecular hydrogen, 1×10^{-9} and 1×10^{-8}. Figure 2.2 shows the fractional populations in the first four rotational levels as a function of radius for all three models with the lower relative abundance. In this case there is a relatively low optical depth in all the HCO^+ transitions. The LVG model approaches the accuracy of the Monte Carlo method in this case as over most of the sphere photons either are absorbed at a nearby radius or tend to escape the cloud. Discrepancies between the LVG and Monte Carlo models may be the result of assigning a uniform velocity gradient equal to the turbulent velocity width to each cell. Measuring the actual velocity gradient across the cell would probably result in a better fit of the LVG model to the Monte Carlo model. The LTE method does a poor job as the density is too low over most of the sphere to thermalize the rotational populations.

Figure 2.3 shows the fractional populations in the first four rotational levels of HCO^+ as a function of radius for all three models with a higher relative abundance. In this case the optical depth, especially in the lower transitions, is fairly high. As a result the LVG model does a worse job that the Monte Carlo model at modeling the level populations. There is a higher tendency for photons to be absorbed in a different radial cell than the one they emerged from. The Monte Carlo model appears

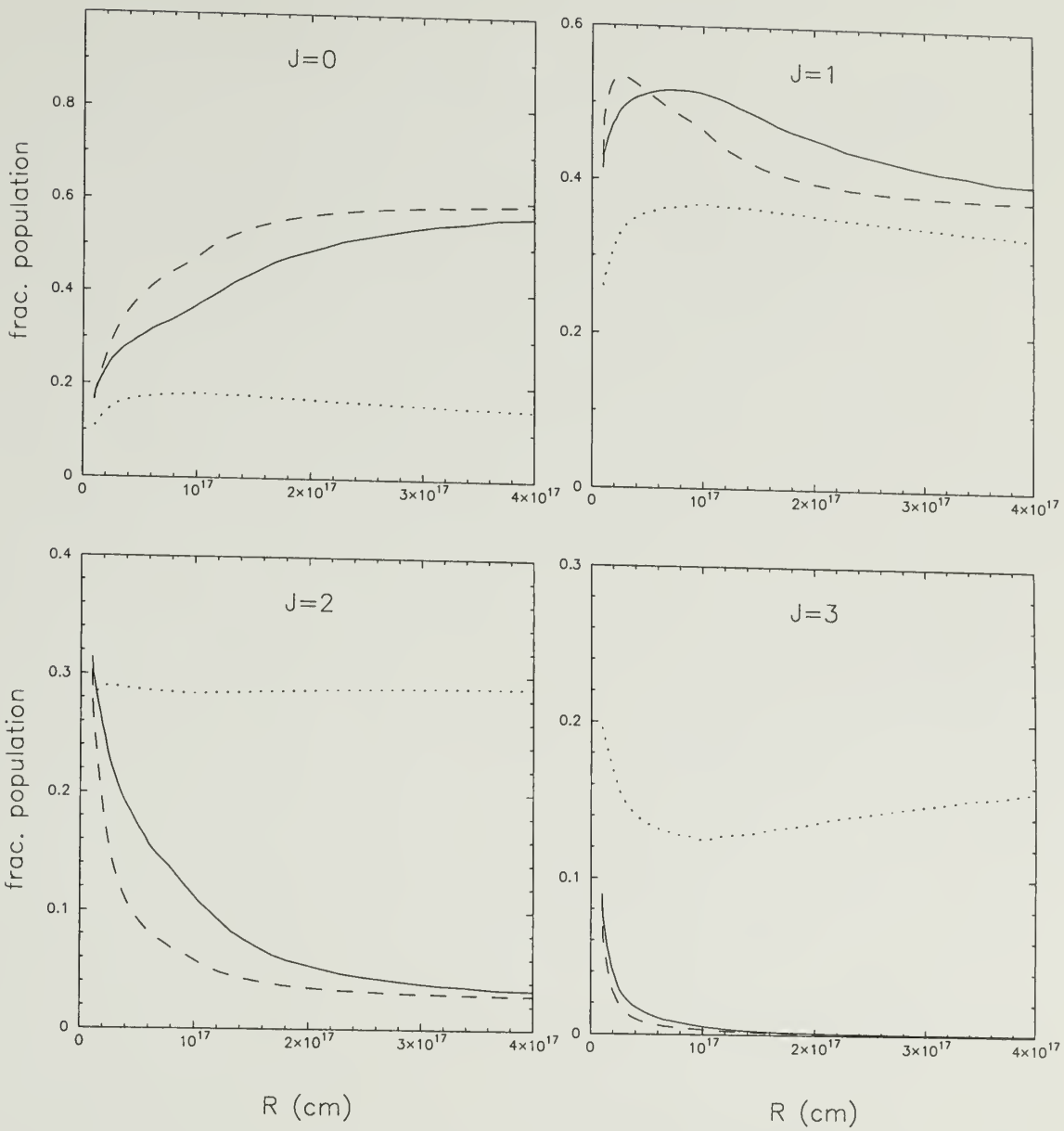

Figure 2.2 Level population models in a one dimensional system at moderate optical depths. A gravitationally collapsing isothermal sphere, following the structure suggested by Shu (1977) has been input into three radiative transfer models. Each assumes a relative abundance of HCO^+ to molecular hydrogen to be 1×10^{-9}. The graphs indicate the fraction of the HCO^+ population in each of the first four excitation levels at different radii within the cloud. The solid line represents the Hogerheijde & van der Tak (2000) Monte Carlo method. The dashed line represents the LVG method discussed in this paper, and the dotted line represents LTE excitation.

to match the LTE model fairly well at small radii where the density is quite high in these regions the HCO^+ rotational quantum levels are nearly thermalized.

2.3.2 Projecting the Model into the Sky Frame

Once the level populations are derived we rotate the molecular cloud model into the orientation in which we wish to observe it. A spherically symmetric model appears the same regardless of the orientation, so we need not manipulate a spherical model before creating synthetic observations, however the VC models are three-dimensional and therefore we must rotate them into the orientation in which we wish to observe them. The bright-rimmed clouds which SFO have observed are typically oriented so that the shock front is moving nearly perpendicular to our line of sight. We choose to rotate the VC models so that their shock fronts are perpendicular to the line of sight in order to make our comparisons with bright-rimmed clouds more direct.

We accomplish the rotation by first rotating the model by an angle θ around the y-axis. We then rotate the cloud around the z-axis by an angle of ϕ. Both of these rotations are in the right handed sense. This results in a coordinate transformation of

$$\begin{pmatrix} x' \\ y' \\ z' \end{pmatrix} = \begin{pmatrix} \cos\theta\cos\phi & -\sin\phi & \sin\theta\cos\phi \\ \cos\theta\sin\phi & \cos\phi & \sin\theta\sin\phi \\ -\sin\theta & 0 & \cos\theta \end{pmatrix} \begin{pmatrix} x \\ y \\ z \end{pmatrix}, \tag{2.10}$$

where (x, y, z) is the coordinate system of the protostellar frame, and (x', y', z') is the coordinate system of the observer. Figure 2.4 illustrates this coordinate transformation. After reprojection the line of sight is in the direction of the z'-axis, and the sky plane is defined by the x',y' plane. The x'-axis points in the direction of increasing right ascension and the y'-axis points in the direction of increasing declination.

At this point we also can resample the data to a higher or lower spatial resolution. We tend to oversample by a small factor (~ 1.2) in order to assure that the model is fully sampled after reprojection.

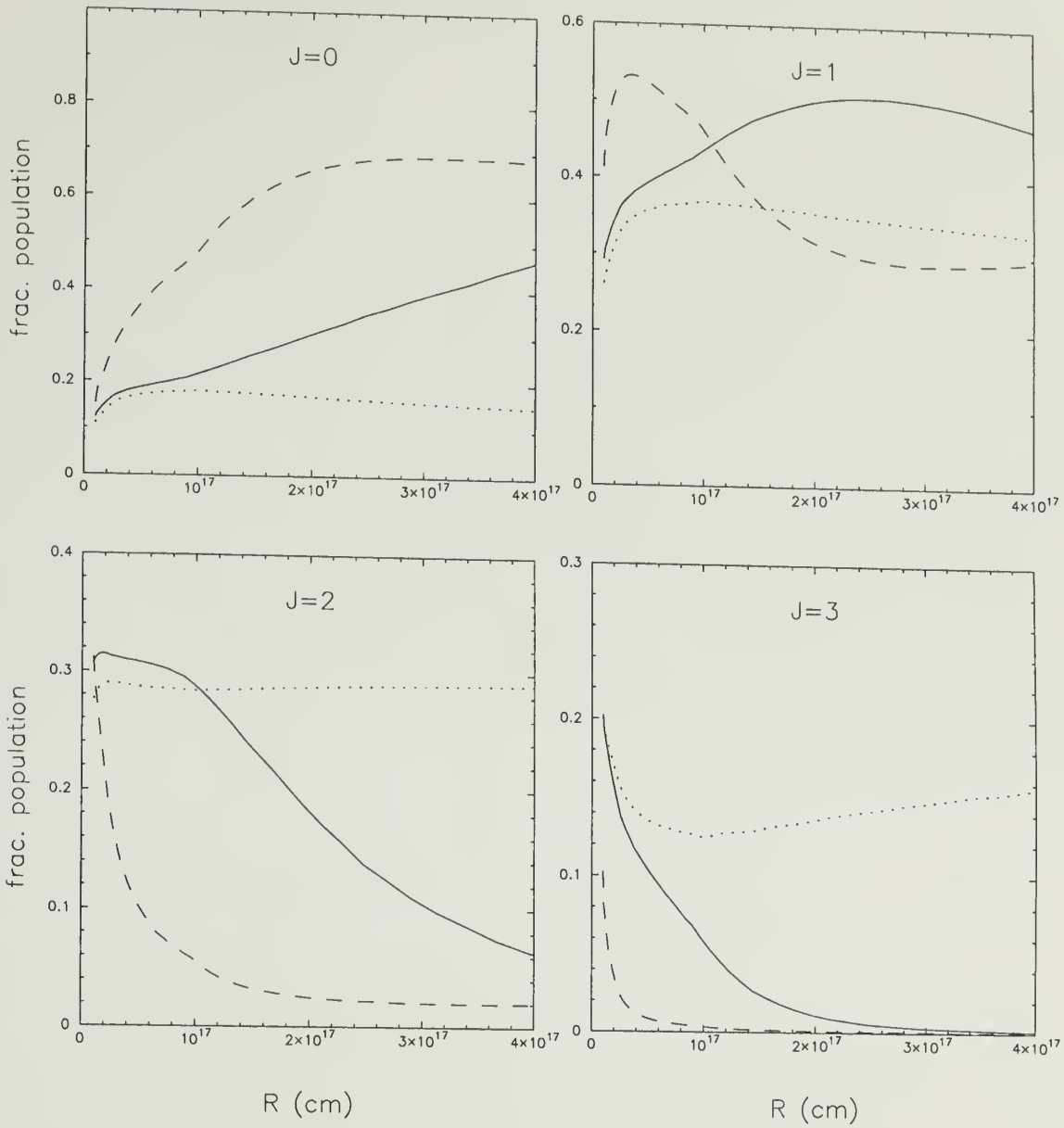

Figure 2.3 Level population models in a one dimensional system at high optical depths. A gravitationally collapsing isothermal sphere, following the structure suggested by Shu (1977) has been input into three radiative transfer models. Each assumes a relative abundance of HCO^+ to molecular hydrogen to be 1×10^{-8}. The graphs indicate the fraction of the HCO^+ population in each of the first four excitation levels at different radii within the cloud. The solid line represents the Hogerheijde & van der Tak (2000) Monte Carlo method. The dashed line represents the LVG method discussed in this paper, and the dotted line represents LTE excitation.

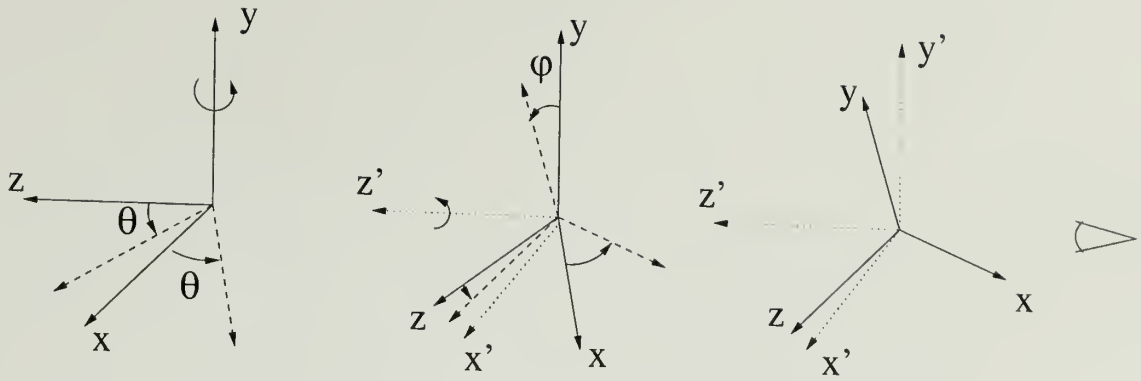

Figure 2.4 Projection of the three dimensional models onto the sky-plane. Projection of the model onto the sky plane involves rotation first around the y-axis, then around the z-axis. We then integrate along the line of sight (z′-axis) to create spectra which populate the sky plane.

2.3.3 Observing the Model

Creating the model spectra along each line of sight involves integrating the intensity for each velocity bin of the spectrum. In each cell along the line of sight we calculate the source function, S_ν, which measures the intensity of radiation resulting from spontaneous emission for a particular transition and frequency within a given cell based upon the physical conditions and level population which we previously calculated. The source function for a transition $J = u \rightarrow l$ is given by the expression

$$S_\nu = \frac{n_u A_{ul}}{n_l B_{lu} - n_u B_{ul}}. \tag{2.11}$$

We also calculate the opacity within each cell which is a measure of the stimulated absorption per unit length minus the stimulated emission per unit length. The opacity is expressed as follows,

$$\alpha_\nu = \frac{h\nu}{4\pi}\,\phi(\nu)(n_l B_{lu} - n_u B_{ul}), \tag{2.12}$$

from which we can derive the optical depth in the cell, $\tau_\nu = \alpha_\nu z$ where z is the length of the cell along the line of sight. The equation of transfer states that the radiative

intensity is

$$\frac{dI_\nu}{d\tau_\nu} = -I_\nu + S_\nu. \tag{2.13}$$

By integrating the equation of transfer along the line of sight we can solve for I_ν, which is what we observe. We convert the radiative intensity into a brightness temperature using the Rayleigh-Jeans law,

$$T_b(\nu) = \frac{c^2}{2k\nu^2}\, I_\nu. \tag{2.14}$$

This allows us to directly compare our synthetic spectra to observational spectra which are typically measured in thermal units.

The final step in the process of creating synthetic observations of models is to convolve our spectra to the beam width of the telescope we use to make real observations. We do this by assigning a distance to the object being modeled and then we apply a gaussian convolving kernel to the spectral line map. In order for our observations to be well sampled there must be several input spectra convolved within any given beam width. We choose distances at which the distance between spectra in our input model is less than 5″, allowing us to convolve down to a beam size of 20″ without undersampling the beam.

2.4 Radiative Transfer Modeling Results

We obtained five models from VC in which we have used the techniques discussed in this chapter to make synthetic observations. We model several time steps in each simulation in order to observe the evolution of the star forming region. For all the models we use molecular abundances relative to molecular hydrogen given by Hogerheijde et al. (1999). The relative abundance of CO to molecular hydrogen is 10^{-4}. The relative abundance of HCO^+ to molecular hydrogen is 10^{-9}. We use isotopic ratios for $[^{12}C]$:$[^{13}C]$ of 64 and $[^{16}O]$:$[^{18}O]$ of 540. We have also assumed a turbulent

velocity width of 0.25 km s^{-1}. We've assumed Local Thermodynamic Equilibrium for CO and its isotopes and used the LVG approximation for HCO^+ and its isotopes. We place the models at a distance of 400 pc and convolve to beam widths equal to the beams of telescopes we use to observe bright-rimmed clouds as discussed in Chapter 3. We have rotated the models so that our line of sight is perpendicular to the propagation direction of the shock front. In all of our maps the shock front travels from east to west. We use molecular parameters from Pickett et al. (2000, 1998) and collisional rate coefficients for the HCO^+ rotational excitation from Flower (1999).

Table 2.2 indicates the parameters of each of the VC models. The table indicates the peak density in the core $\rho_{\rm max}$, the effective magnetic field strength $B_{\rm eff}$, the shock velocity $v_{\rm sh}$, the core mass, if the core collapsed, the time in which it took for the core to collapse or how long the simulation was run if the core did not collapse, and the fraction of the original core mass in the collapsing protostar $f_{\rm core}$. In order to quantify the effect of triggering we have chosen models in which collapse did and did not occur, to see if we can differentiate between them. We also chose models with and without an effective magnetic field, models with different shock front velocities, and a model which formed a binary system. All the models have initial core radii of ~ 0.1 pc and are embedded in a background cloud of density 10^{-21} g cm^{-3}.

For each simulation run we present the spectra in the direction of the core center, integrated intensity maps of the emission in each rotational transition, and centroid velocity maps of the self-absorbed HCO^+ transitions. We present these particular views of the modeled observations because they are commonly presented in observational studies (including our own observational studies of bright-rimmed clouds in Chapter 3). Negative velocities correspond to blue-shifted emission and positive velocities correspond to red-shifted emission. The line profiles often show indications of self-absorption and the "classic" blue asymmetric line profile indicating infall. The integrated intensity maps indicate the morphology of the emission region on the plane

Table 2.2. Simulation Runs: Initial Conditions

Run[a]	ρ_{max} (g cm^{-3})	B_{eff} (μG)	v_{sh} (km s^{-1})	Core Mass ($M_\odot$)	Collapse?	Time (yr)	f_{core}
F	7.35×10^{-17}	0	25	3.317	Yes	5.76×10^4	0.312
O	7.28×10^{-18}	1	50	3.735	No	3.12×10^5	...
Q	6.87×10^{-17}	1	19	4.872	Yes	3.00×10^4	0.333
K	7.28×10^{-18}	1	10	3.735	No	2.45×10^5	...
I	7.49×10^{-19}	1	10	19.87	Yes[b]	9.74×10^4	0.428

[a]Hydrodynamic models were provided by VC and follow the same naming scheme.

[b]Run I actually produced a binary star system.

of the sky. The centroid velocity maps can be used to see trends in the kinematics across the cloud as well as to find the signature of spectral changes which may indicate infall or outflow. One example is the blue bulge signature which is a result of the disruption of an ordered velocity gradient across a rotating cloud by blue asymmetric line profile resulting from infall within the rotating cloud (Narayanan, 1997; Narayanan et al., 1998, 2002). In all the figures below the shock front moves perpendicular to the line of sight from east to west. The ionized gas wind blows directly from the east and the molecular gas is swept into a ridge which is aligned north-south. We will highlight those features which require special attention in each simulation.

2.4.1 Run F

Run F depicts a 3 $M_\odot$ cloud core under the influence of a 25 km s^{-1} wind. The core becomes self gravitating after 5.76×10^4 years to form a star of approximately 1 $M_\odot$. Figure 2.5 shows our modeled spectra for the cloud core position at various time steps in the hydrodynamic simulation. In the earliest timestep, 2.1×10^4 yr, there is some self absorption of the main HCO^+ line relative to $H^{13}CO^+$. In the HCO^+ ($J = 1 \rightarrow 0$) and HCO^+ ($J = 3 \rightarrow 2$) a blue asymmetry is visible, which arises from the infalling

motion around the cloud core. At this point in the simulation the shock front is just reaching the core position, so it corresponds most closely to a SFO type A morphology. The next timestep, 2.7×10^4 yr, also corresponds to a SFO type A morphology, but the shock front has just passed through the core. The linewidths at this timestep are larger, between 3 and 4 km s^{-1}, and the blue asymmetry indicative of infall is more visible in all the transitions. In the third timestep, 4.2×10^4 yr, the asymmetry of the main HCO^+ lines relative to their $H^{13}CO^+$ counterparts is reduced, although infalling motions around the core continue. This may be due to an effect explored in §4.2 where the presence of a temperature gradient which increases away from the core center tends to lessen the blue asymmetric infall signature. The line profiles have become more narrow, though a tail is visible on the HCO^+ $(J = 1 \rightarrow 0)$ transition. In the final time step, 7.0×10^4 yr, the shock front has moved well beyond the simulation space leaving a cometary cloud that resembles a SFO type C morphology. At this point the core is gravitationally bound and the HCO^+ line profiles are nearly gaussian, with potentially a slightly bluer centroid than their $H^{13}CO^+$ counterparts.

Figure 2.6 depicts the evolution over time of the HCO^+ integrated intensity maps of VC simulation run F. The top row is the HCO^+ $(J = 4 \rightarrow 3)$ emission, the middle is the HCO^+ $(J = 3 \rightarrow 2)$ emission, and the bottom is the HCO^+ $(J = 1 \rightarrow 0)$ emission. Each column represents a different time step, evolving from left to right. The shock front approaches from the east in all the maps we will present. At 2.1×10^4 years, the HCO^+ emission region has assumed a shield-like shape, characteristic of a type A morphology. Both the core and the envelope are visible in all the HCO^+ transitions. At 2.7×10^4 years, the core, located at a right ascension offset of approximately $100''$ is the source of the majority of the HCO^+ $(J = 4 \rightarrow 3)$ emission. The movement of the shock front through the core region has had a pronounced effect on the excitation of the HCO^+ molecule. In the HCO^+ $(J = 1 \rightarrow 0)$ transition the emission from the core dominates, but the emission from the swept up gas is significant. At 4.2×10^4 years

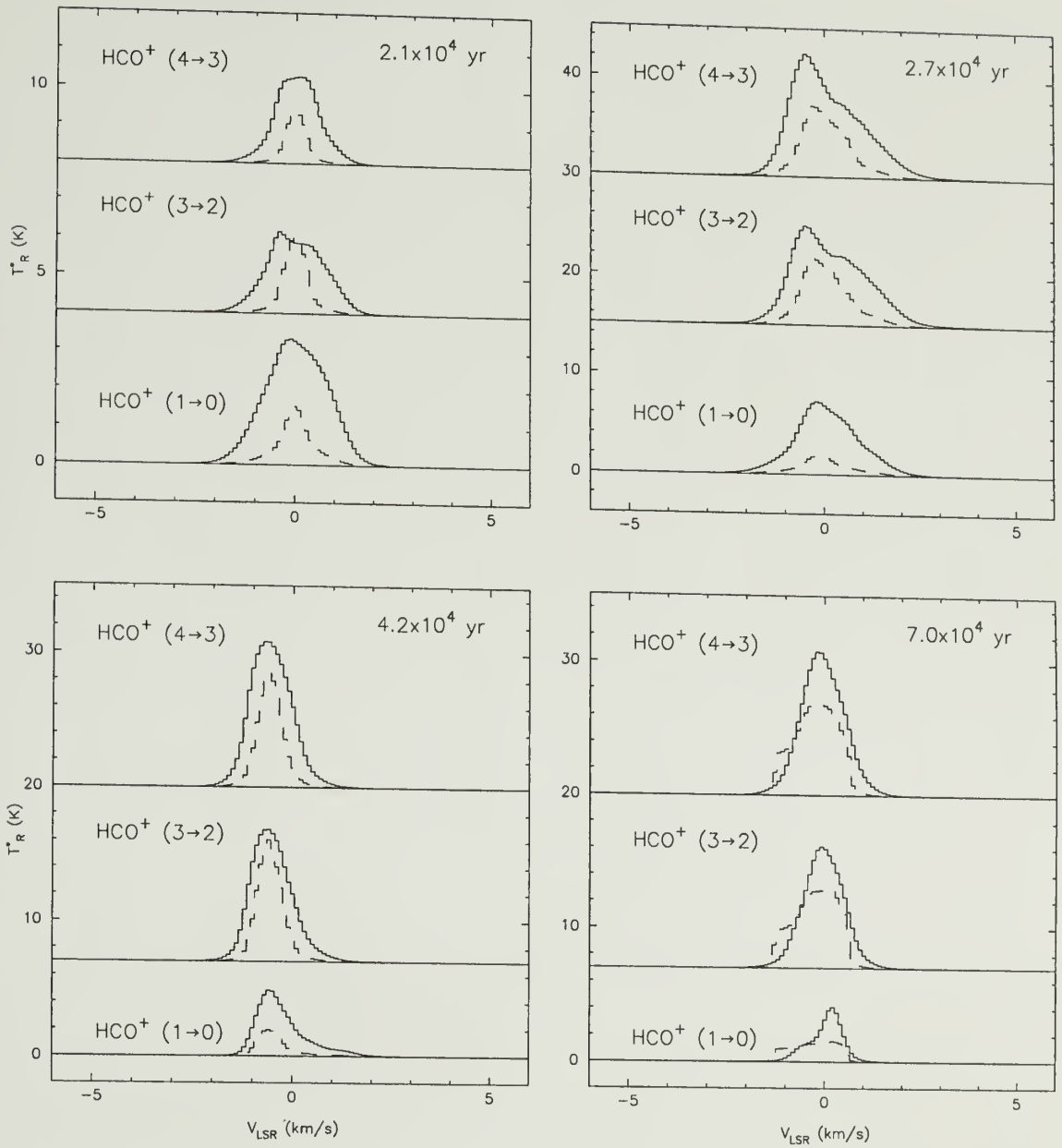

Figure 2.5 HCO^+ and $H^{13}CO^+$ line profiles at various time steps in simulation F. The solid line is the indicated HCO^+ transition, while the dashed line is the corresponding $H^{13}CO^+$ isotopic line. The isotopic line has been magnified relative to the main line by a factor of 5 at 2.1×10^4 yr, and by 10 in all other time steps.

the type B morphology is clearly visible in all the HCO^+ integrated intensity maps, especially in the HCO^+ $(J = 3 \rightarrow 2)$ transition. While the HCO^+ $(J = 4 \rightarrow 3)$ and HCO^+ $(J = 3 \rightarrow 2)$ emission peaks at the star forming core, located at the head of the cloud, the HCO^+ $(J = 1 \rightarrow 0)$ emission is more uniformly distributed over the entire cloud. From this we infer that although the star forming core is very dense, most of the mass from the core has been blown down the tail of the cloud. VC confirm this in their simulation, roughly 2/3 of the core gas gets stripped from the core by the wind. Another interesting feature in the HCO^+ $(J = 4 \rightarrow 3)$ and HCO^+ $(J = 3 \rightarrow 2)$ maps is the presence of a second clump, trailing the star forming core by approximately 60″. Although not bound, this clump may indicate that even with a uniform wind, there can be some fragmentation of the gas stripped from the star forming core. These fragments may later also become self-gravitating and form stars in a process called sequential star formation (Sugitani, Tamura, & Ogura, 1995, 1999). At 7.0×10^4 years the HCO^+ emission morphology resembles a cometary or type C cloud. Once again the HCO^+ $(J = 4 \rightarrow 3)$ and HCO^+ $(J = 3 \rightarrow 2)$ emission peaks at the star forming core, which is at the head of the cometary cloud. The HCO^+ $(J = 1 \rightarrow 0)$ emission peaks near the tail of the cometary cloud, where the density is low, but the column density is fairly high, though emission along the tail of the cloud does not vary much in this transition. At this point the star forming core is self-gravitating and much smaller than our beam sizes.

Figure 2.7 depicts the centroid velocity maps of the modeled HCO^+ spectral line profiles. At early times (2.1×10^4 and 2.7×10^4 years), as the molecular gas is swept into a ridge, there is very little change in the centroid velocity across the emission region. As the shock front engulfs the core, at 4.2×10^4 years, when the cloud enters a type B morphology, an ordered gradient appears in all the HCO^+ transitions, though variations are most visible in the HCO^+ $(J = 4 \rightarrow 3)$ transition. The core region stands out as having a lower centroid velocity than much of the rest of the cloud,

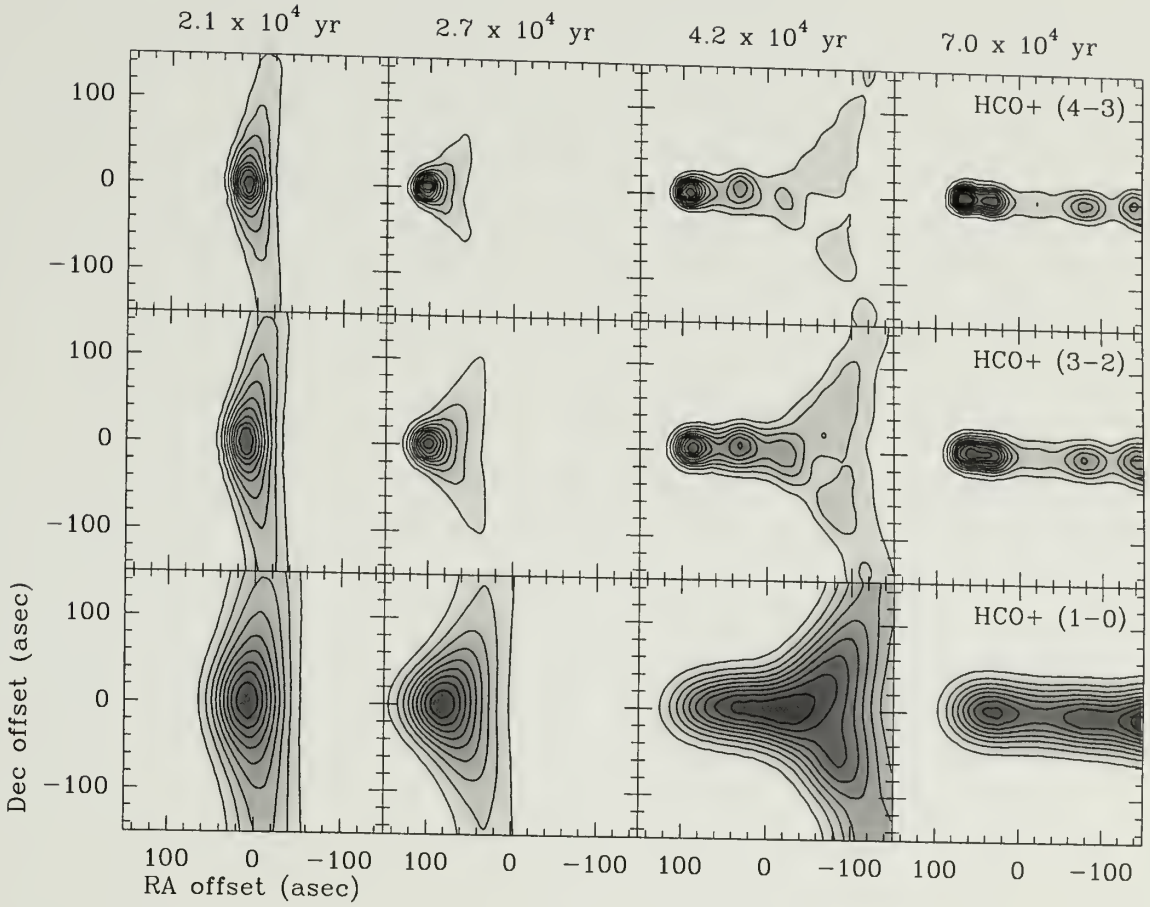

Figure 2.6 Integrated intensity maps of the HCO^+ emission from simulation F. The contours run from 10% to 90% of the peak integrated intensity in increments of 10%.

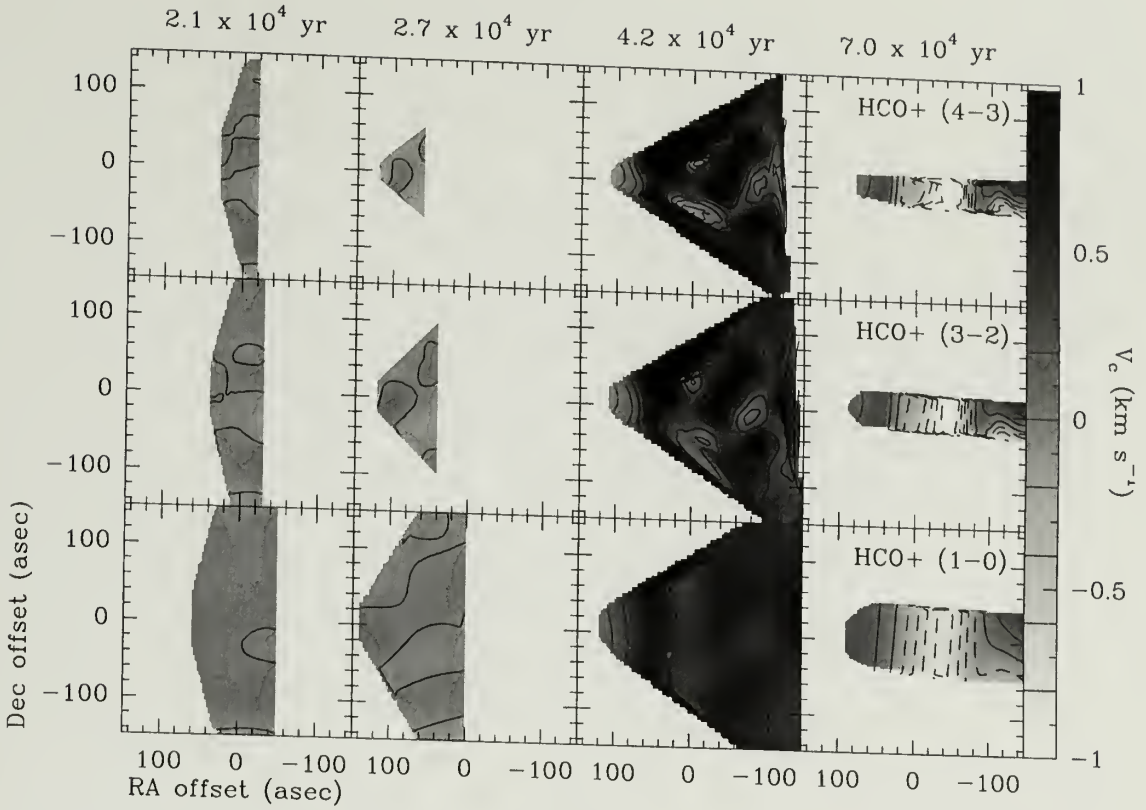

Figure 2.7 Centroid velocity maps of the HCO^+ line emission from simulation F. The wedge to the right of the centroid maps indicates the velocities of the contours. Dashed contours indicate negative velocity centroids and solid contours indicate positive velocity centroids.

while the edges of the emission region seem to have a higher centroid velocity. The low centroid velocity at the core position may be the result of the blue-asymmetric infall profile, while the high centroid velocity at the edges may be due to molecular gas expansion along the shock front interface. At the latest timestep, 7.0×10^4 years, the centroid velocity moves from receding to approaching, then back to receding as we trace emission from the head to the tail of the cometary cloud. This trend is interesting because there appears to be a higher centroid velocity in regions where there is a lot of HCO^+ emission, while the centroid velocity is lower where there is little HCO^+ emission.

Figure 2.8 depicts the evolution over time of the CO integrated intensity maps of VC simulation run F. The top row is the CO ($J = 2 \rightarrow 1$) emission, the bottom is

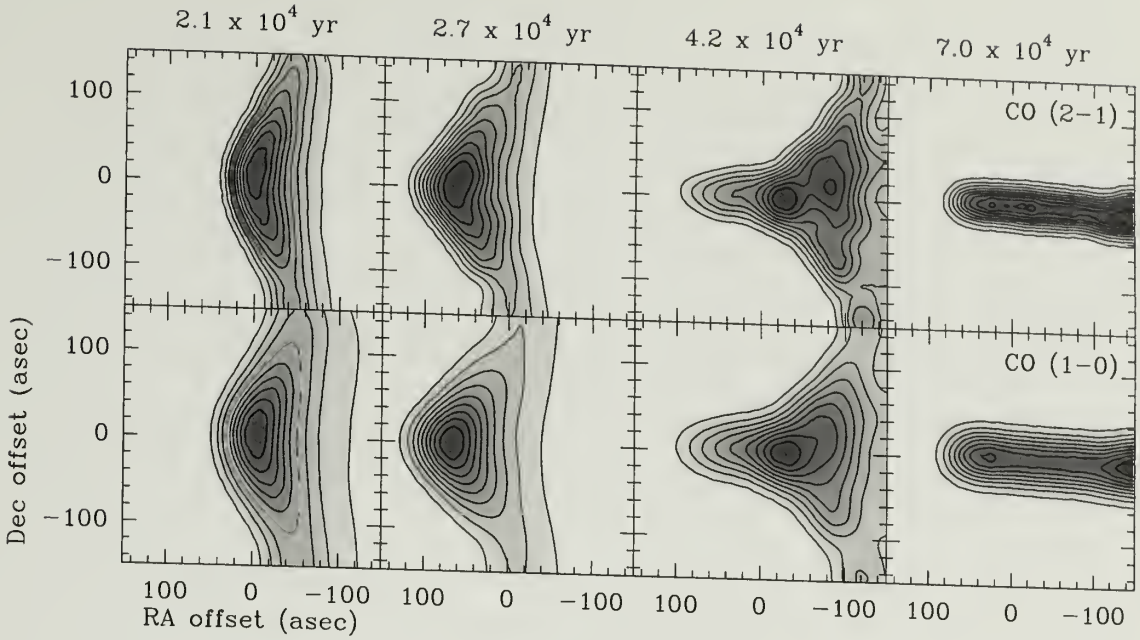

Figure 2.8 Integrated intensity maps of the CO emission from simulation F. The contours run from 10% to 90% of the peak integrated intensity in increments of 10%.

the CO ($J = 1 \rightarrow 0$) emission. Each column represents a different time step, evolving from left to right. At the earliest timestep (2.1×10^4 years) the core as well as the ridge of swept up gas is traced by the CO emission, though a broader region is traced by CO than that traced by HCO^+. The CO emission at this timestep is in a type A morphology. At 2.7×10^4 years the CO emission still is in a type A morphology, but it is evolving towards a type B morphology as the shock front wraps around the dense core. At 4.2×10^4 years the CO emission in both the $J = 2 \rightarrow 1$ and $J = 1 \rightarrow 0$ transitions is in a type B morphology. As with the HCO^+ ($J = 1 \rightarrow 0$) transition at this time, the CO emission does not peak at the core position, but approximately 100″ behind the core where there is a significant amount of swept up gas. Finally at 7.0×10^4 years the CO emission is in a cometary or type C morphology with a rather uniform amount of emission along the entire cloud. Although the density behind the head of the cloud is rather low, the total column density, traced by the CO emission, remains fairly high throughout the cloud.

2.4.2 Run O

Run O depicts a 4 $M_\odot$ cloud core under the influence of a 50 km s^{-1} wind with a 1 μG effective magnetic field. The core gets pulled apart by the wind and does not collapse into a star in this scenario. Figure 2.9 shows our modeled spectra for the cloud core position at various time steps in the hydrodynamic simulation. As the core fragments we define the core position to be the peak integrated intensity position of the $H^{13}CO^+$ ($J = 4 \rightarrow 3$) emission. In the earliest timestep, 2.1×10^4 yr, there appears to be some self absorption, especially in the HCO^+ ($J = 3 \rightarrow 2$) line, but the HCO^+ line profiles appear to share the same centroid positions as their $H^{13}CO^+$ counterparts. At the next timestep, 2.7×10^4 yr, the intensity of all the lines has increased, but there is still very little asymmetry, although the centroid of all the HCO^+ lines are slightly redshifted compared to the $H^{13}CO^+$ lines. At 4.2×10^4 yr the HCO^+ ($J = 4 \rightarrow 3$) and HCO^+ ($J = 3 \rightarrow 2$) lines have more structure which resembles a blue-asymmetry, however the $H^{13}CO^+$ lines show the same structure indicating that this could just be a superposition of cores along the line of sight. At the latest time step the lines have lessened in intensity and are narrower than in the final timestep of run F (Figure 2.5).

Figure 2.10 depicts the evolution over time of the HCO^+ integrated intensity maps of VC simulation run O. The top row is the HCO^+ ($J = 4 \rightarrow 3$) emission, the middle is the HCO^+ ($J = 3 \rightarrow 2$) emission, and the bottom is the HCO^+ ($J = 1 \rightarrow 0$) emission. Each column represents a different time step, evolving from left to right. At 2.1×10^4 years all the HCO^+ integrated intensity maps are peaked at the core position and show a ridge of emission where the molecular gas has been swept up by the shock front. All the HCO^+ integrated intensity maps show a type A morphology. At 2.7×10^4 years the core emission now dominates the HCO^+ ($J = 4 \rightarrow 3$) emission, indicating that the shock front has had a profound effect on the physical state of the core, resulting in the collisional excitation of HCO^+ to higher rotational states in the core. The morphology of all the HCO^+ integrated intensity maps is still type A, though the

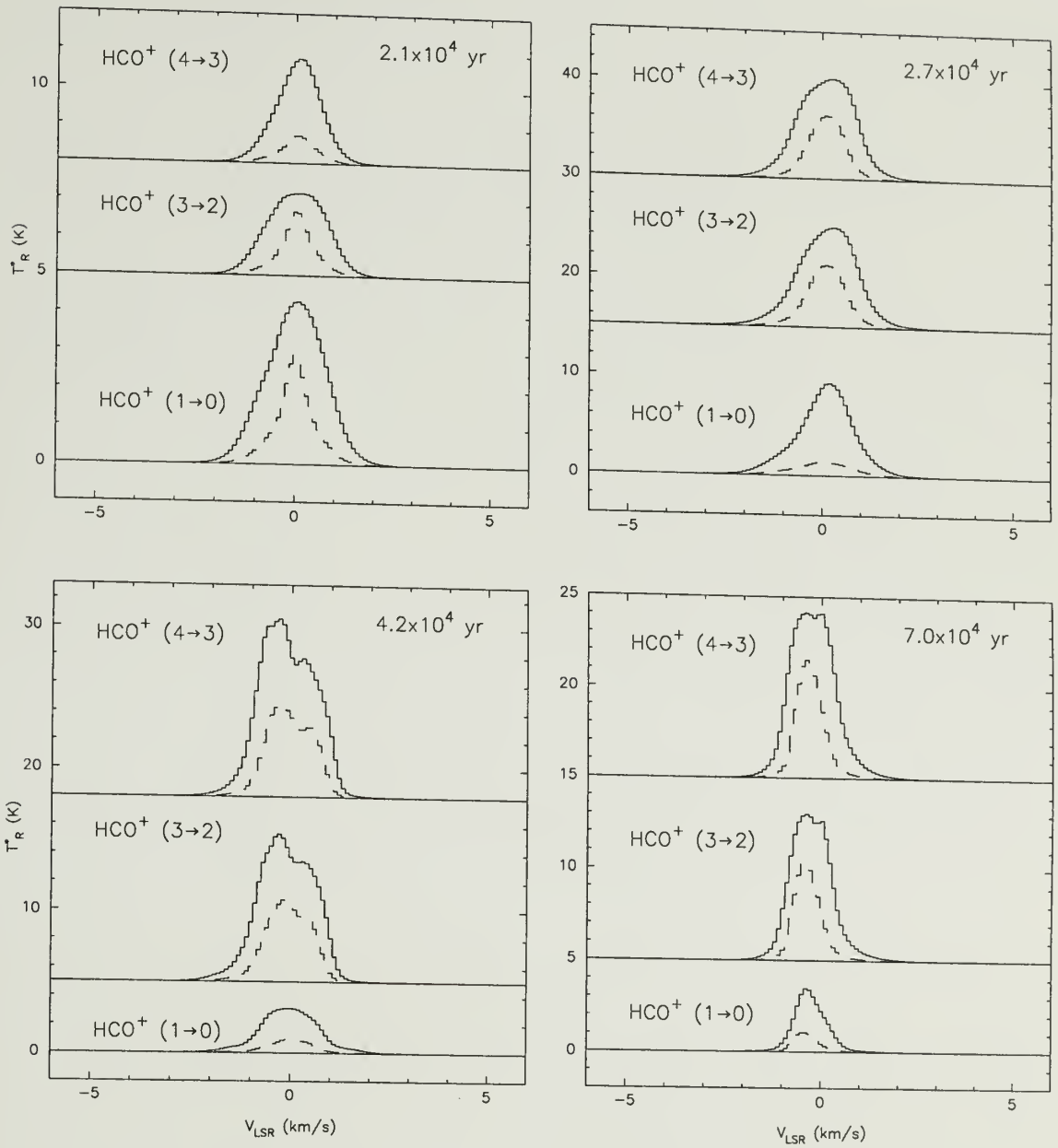

Figure 2.9 HCO^+ and $H^{13}CO^+$ line profiles at various time steps in simulation O. The solid line is the indicated HCO^+ transition, while the dashed line is the corresponding $H^{13}CO^+$ isotopic line. The isotopic line has been magnified relative to the main line by a factor of 10.

head of the elephant trunk is starting to separate from the curved region of swept up gas. The HCO^+ integrated intensity maps achieve a type B morphological type at 4.2×10^4 years. Although the HCO^+ $(J = 4 \rightarrow 3)$ and HCO^+ $(J = 3 \rightarrow 2)$ emission peaks at the core position, there are several other emission peaks behind the core and along the ridge of swept up gas. These indicate positions of relatively high density along the line of sight in those directions. The HCO^+ $(J = 1 \rightarrow 0)$ emission peaks at the point where the elephant trunk emerges from the curved north-south ridge, which is where much of the gas swept from the core position has gone. In the final timestep, 6.9×10^4 years, the HCO^+ integrated intensity maps now show a type C morphology. Only the HCO^+ $(J = 4 \rightarrow 3)$ emission has its highest peak at the core position, the HCO^+ $(J = 3 \rightarrow 2)$ emission has three peaks of nearly equal intensity along the tail of the cometary cloud. This is indicative of the fact that the core did not achieve self-gravitation. The majority of the gas has been swept down the tail of the cloud. The relative intensity of the HCO^+ $(J = 4 \rightarrow 3)$ in the head of the cometary cloud relative to the tail is quite different in this case where there is no collapse compared to run F where the core does collapse under the influence of gravity (Figure 2.6). The HCO^+ $(J = 1 \rightarrow 0)$ integrated intensity at this time, however is quite similar to that of the final timestep of run F. This indicated that the submillimeter HCO^+ transitions may be the best observational tracers to distinguish self-gravitating cores from non-self-gravitating cores in the later stages of bright-rimmed cloud evolution.

Figure 2.11 depicts the centroid velocity maps of the modeled HCO^+ spectral line profiles. At early time steps there is not much variation in the centroid velocity of the HCO^+ lines. There is some velocity gradient along the ridge, but it is small. At 4.2×10^4 years, the centroid velocity maps become more complex, especially in the higher resolution submillimeter transitions. The core position is at a slightly lower velocity than much of the rest of the cloud, however the centroid velocity map is less well ordered than the HCO^+ centroid velocity maps of run F (Figure 2.7). In

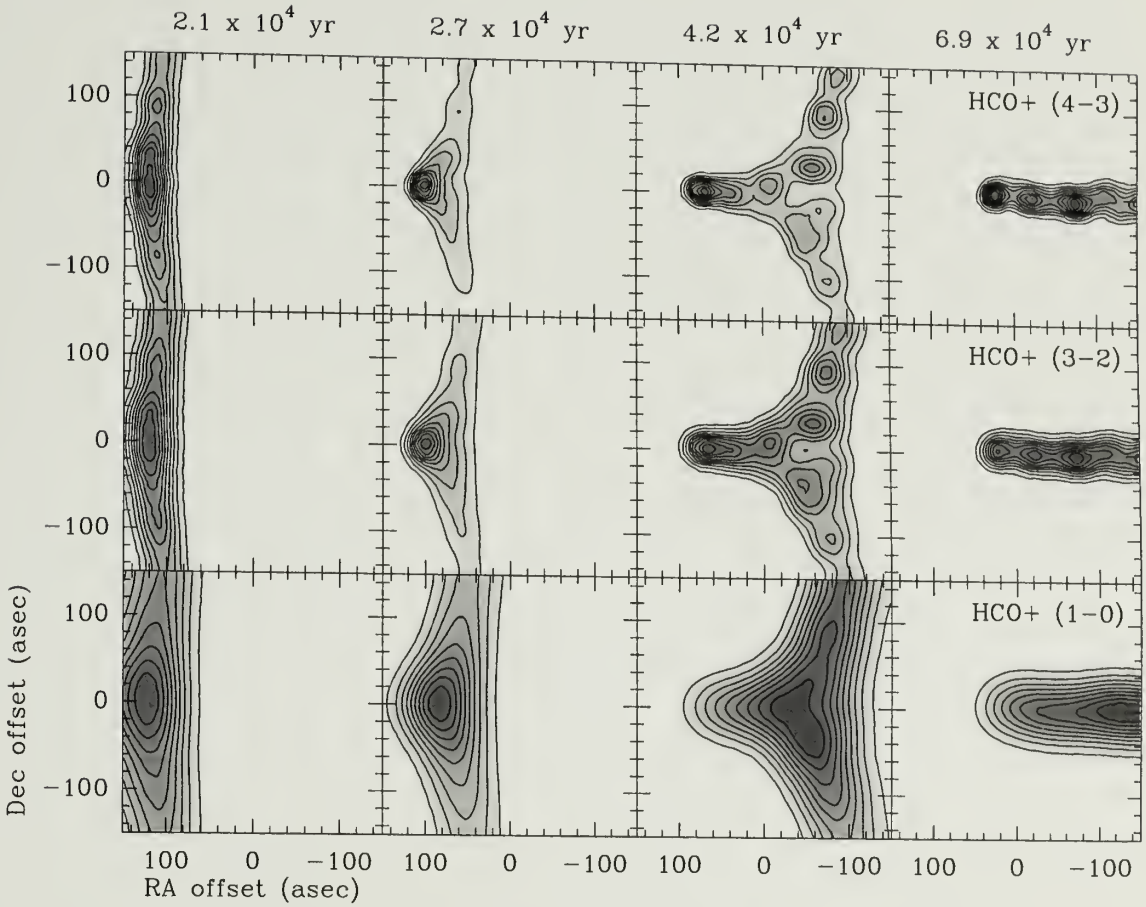

Figure 2.10 Integrated intensity maps of the HCO^+ emission from simulation O. The contours run from 10% to 90% of the peak integrated intensity in increments of 10%.

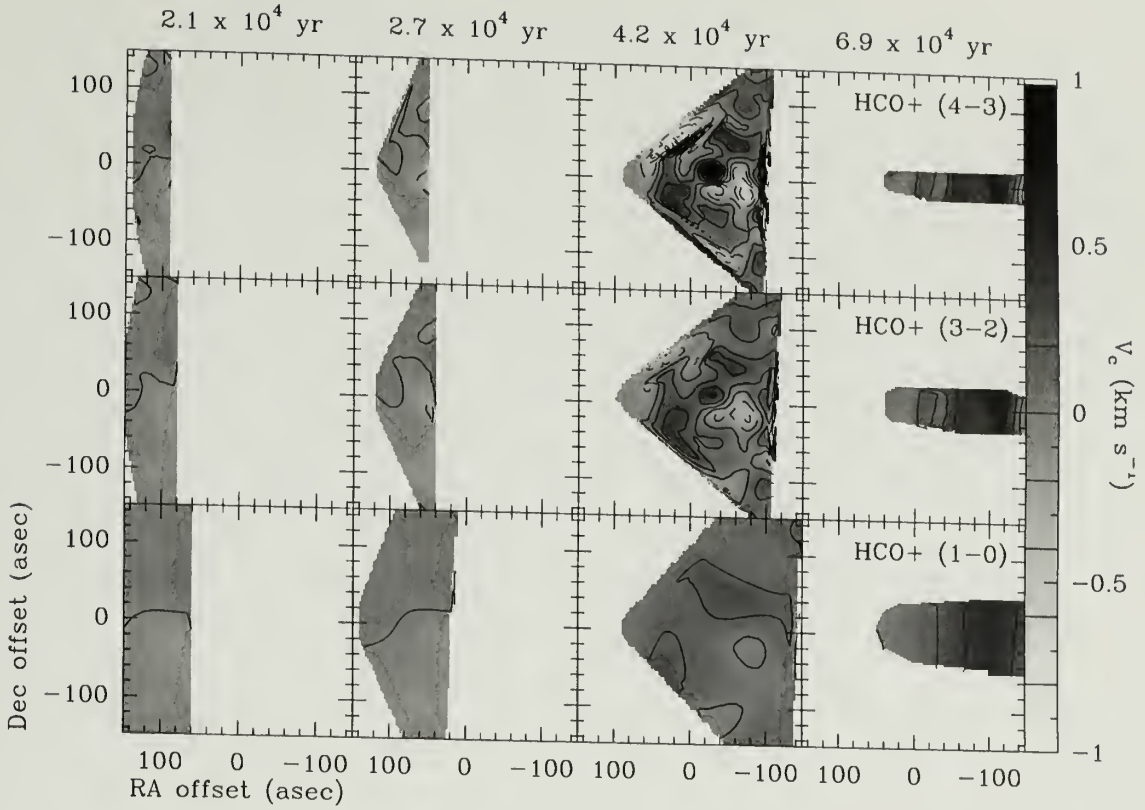

Figure 2.11 Centroid velocity maps of the HCO^+ line emission from simulation O. The wedge to the right of the centroid maps indicates the velocities of the contours. Dashed contours indicate negative velocity centroids and solid contours indicate positive velocity centroids.

the final timestep of the simulation, the centroid velocity shows a gradient that runs predominantly along the cometary cloud.

Figure 2.12 depicts the evolution over time of the CO integrated intensity maps of VC simulation run O. The top row is the CO ($J = 2 \rightarrow 1$) emission, the bottom is the CO ($J = 1 \rightarrow 0$) emission. Each column represents a different time step, evolving from left to right. At 2.1×10^4 years the CO integrated intensity maps exhibit a type A morphology, however they seem a little bit more evolved than their counterparts at the same timestep in the HCO^+ integrated intensity maps (Figure 2.10). This may indicate the presence of ambiguities in the morphological classification scheme which depend upon the observed emission. At 2.7×10^4 years the CO integrated intensity morphology is till type A, as is the HCO^+ morphology. The CO emission

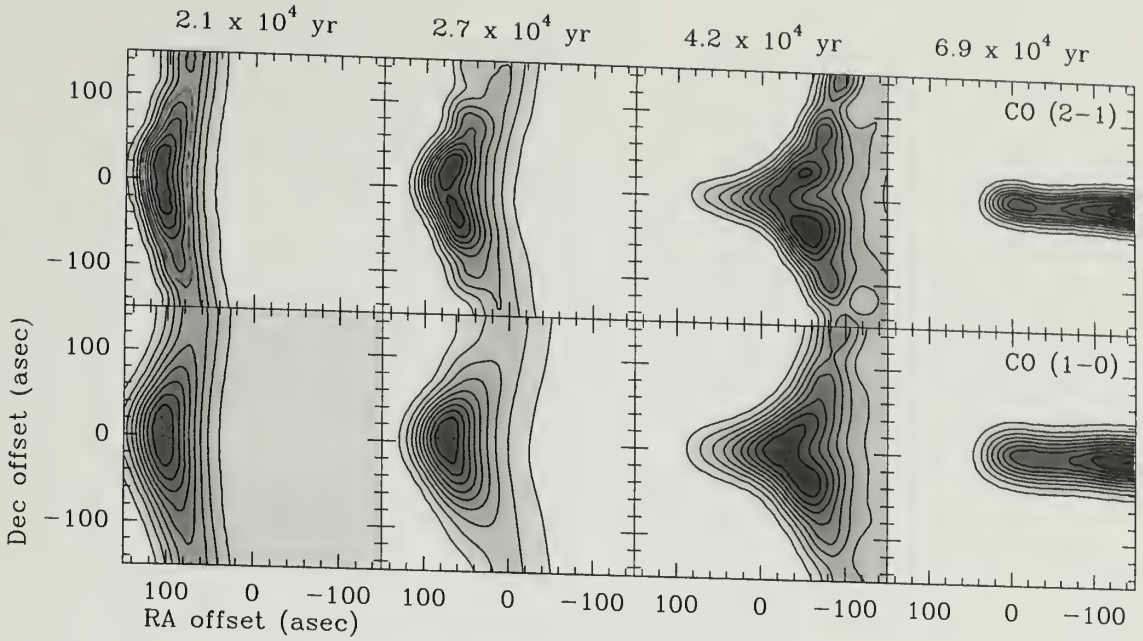

Figure 2.12 Integrated intensity maps of the CO emission from simulation O. The contours run from 10% to 90% of the peak integrated intensity in increments of 10%.

peaks further west than the core position where the HCO^+ ($J = 4 \rightarrow 3$) peaks, and in the CO ($J = 2 \rightarrow 1$) integrated intensity map there is some structure visible along the ridge. By 4.2×10^4 years the CO integrated intensity has assumed a type B morphology. The CO ($J = 1 \rightarrow 0$) peaks at the same location as the HCO^+ ($J = 1 \rightarrow 0$) integrated intensity map, however the CO ($J = 2 \rightarrow 1$) continues to show more structure along the ridge, which correspond somewhat to regions where there are dense knots along the line of sight. Finally, at 6.9×10^4 years the CO emission is in the morphology of a cometary cloud with fairly uniform emission levels along the length of the cloud, much as in the final time step of run F (Figure 2.8).

2.4.3 Run Q

Run Q is a hydrodynamic simulation of a 19 km s^{-1} wind impacting a 5 $M_\odot$ cloud core in a 1 μG effective magnetic field. This core does collapse under the influence of the wind into a gravitationally bound core 1/3 the mass of the original core after 3×10^4 years. Figure 2.13 shows our modeled spectra for the cloud core position at various

timesteps in the hydrodynamic simulation. In the earliest timestep, 2.1×10^4 yr, the HCO^+ lines are all self-absorbed. The HCO^+ $(J = 3 \rightarrow 2)$ and HCO^+ $(J = 4 \rightarrow 3)$ lines show a slight blue-asymmetry relative to their $H^{13}CO^+$ counterparts indicating that the cloud is infalling. At 2.7×10^4 yr, as the shock front reaches the core, the self absorption is still evident, and although the HCO^+ $(J = 3 \rightarrow 2)$ line shows some blue-asymmetry, the HCO^+ $(J = 1 \rightarrow 0)$ line shows red-asymmetry. As the swept-up molecular gas moves past the core at 4.2×10^4 yr, the red-asymmetry becomes quite pronounced in the HCO^+ $(J = 1 \rightarrow 0)$ transition, however the higher frequency HCO^+ transitions still show a blue-asymmetry. This may still indicate that infall is occurring, but that the excitation temperature gradient across the core is such that standard blue-asymmetric lines are replaced by symmetric or red-asymmetric line profiles (see §4.2). In the final timestep, 4.5×10^4 yr, we see wide self absorbed HCO^+ lines as well as wide $H^{13}CO^+$ lines. Although at this final time step the cloud is still in a type B morphology, the core has become self-gravitating and would form a star.

Figure 2.14 depicts the evolution over time of the HCO^+ integrated intensity maps of VC simulation run Q.The top row is the HCO^+ $(J = 4 \rightarrow 3)$ emission, the middle is the HCO^+ $(J = 3 \rightarrow 2)$ emission, and the bottom is the HCO^+ $(J = 1 \rightarrow 0)$ emission. Each column represents a different time step, evolving from left to right. The core stands out in the earliest timestep (2.1×10^4 years) of the HCO^+ $(J = 4 \rightarrow 3)$ integrated intensity map as a circular knot located at an offset of 100″ in right ascension. The dense ridge of swept up gas has not yet reached the center of the core at this time. The HCO^+ $(J = 3 \rightarrow 2)$ map also shows a clearly defined core and ridge, however the core merely shows up as a bulge in the ridge in the HCO^+ $(J = 1 \rightarrow 0)$ integrated intensity map. This early type A morphological type cloud might not even be recognized as a bright-rimmed cloud at all as it is in the very early stages of interacting with the star-forming core. At 2.7×10^4 years the swept up molecular gas is

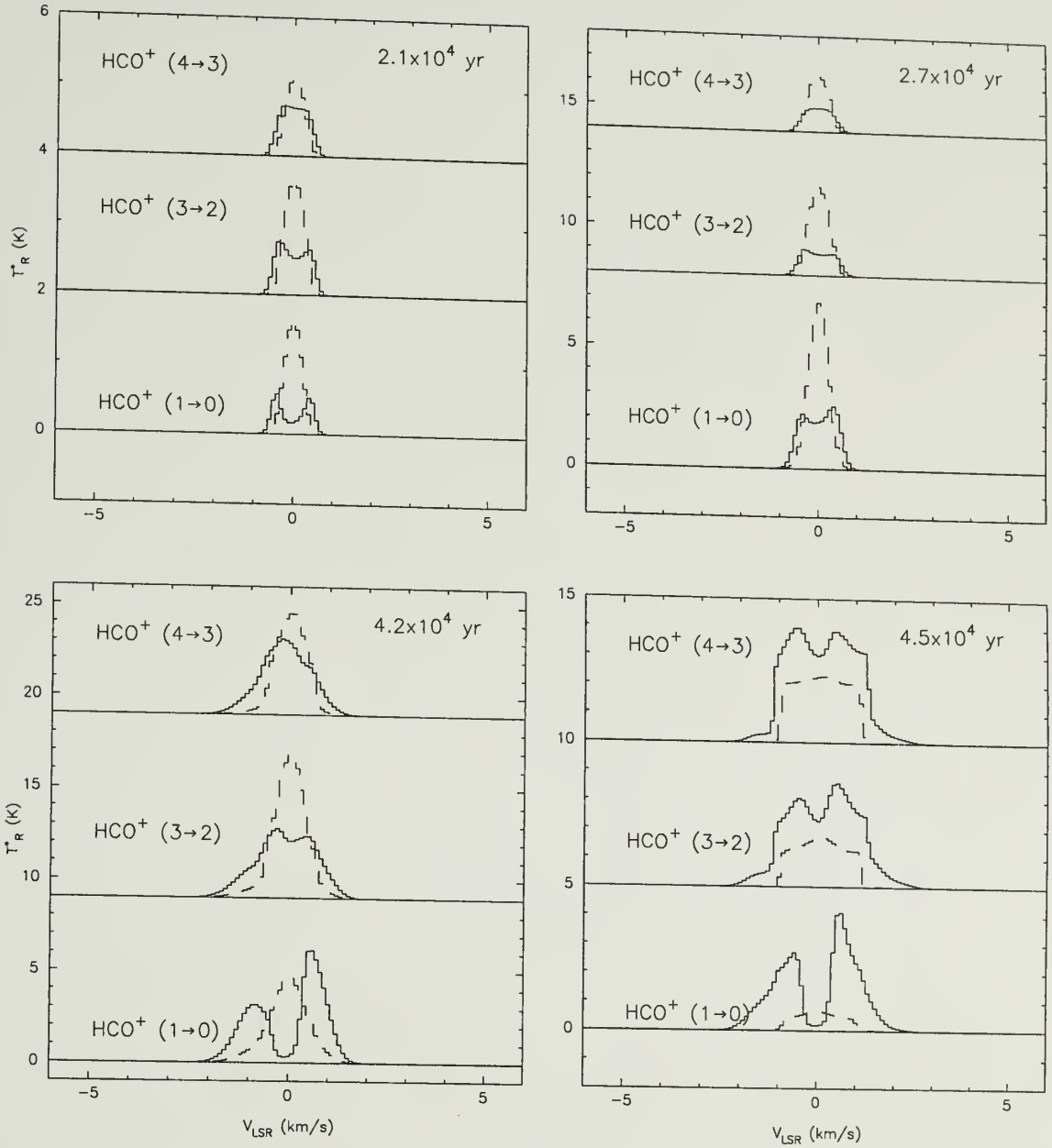

Figure 2.13 HCO^+ and $H^{13}CO^+$ line profiles at various time steps in simulation Q. The solid line is the indicated HCO^+ transition, while the dashed line is the corresponding $H^{13}CO^+$ isotopic line. The isotopic line has been magnified relative to the main line by a factor of 5 at 2.1×10^4 yr, by 10 at 2.7×10^4 yr and at 4.2×10^4 yr, and is unmagnified at 4.5×10^4 yr.

now interacting with the dense core, though the core is still visible at the back edge of the HCO^+ ($J = 4 \rightarrow 3$) integrated intensity map as well as the HCO^+ ($J = 3 \rightarrow 2$) map. As the propagation of the front has slowed at this time due to the core interaction, the developing curvature in the swept up gas makes the morphology a more recognizable type A morphology. At 4.2×10^4 years the majority of the molecular gas has been swept past the core, resulting in an early type B morphology. The dominant source of emission in the HCO^+ ($J = 4 \rightarrow 3$) and HCO^+ ($J = 3 \rightarrow 2$) integrated intensity maps is the core, through a lower level of emission traces the swept up molecular gas. In the HCO^+ ($J = 1 \rightarrow 0$) transition, the gas directly to the west of the core seems to be the dominant emission region. In the final timestep, the core has become gravitationally bound, even though it has not evolved into a cometary cloud. Nevertheless, there are characteristics in the HCO^+ ($J = 4 \rightarrow 3$) map which indicate that this region is forming a star. The core dominates the emission in the HCO^+ ($J = 4 \rightarrow 3$) transition, just like in the final timestep of run F (Figure 2.6). In contrast, the core of run O (Figure 2.10) has emission of a similar magnitude to the tail of the cometary cloud. In other regards the emission patterns of the HCO^+ integrated intensity maps are similar to those of the previous timestep.

Figure 2.15 depicts the centroid velocity maps of the modeled HCO^+ spectral line profiles. Unlike in previous centroid maps, these maps do not show any development of significant centroid velocity gradients across the clouds at any of the timesteps. Although it stars with a slight north-south gradient (2.1×10^4 and 2.7×10^4 years), the gradient starts to become less ordered in later timesteps. This may be due to the magnetic drag imposed in this simulation and the relatively short time the cloud has to evolve before the core collapses.

Figure 2.16 depicts the evolution over time of the CO integrated intensity maps of VC simulation Q. The top row is the CO ($J = 2 \rightarrow 1$) emission, the bottom is the CO ($J = 1 \rightarrow 0$) emission. Each column represents a different time step, evolving from

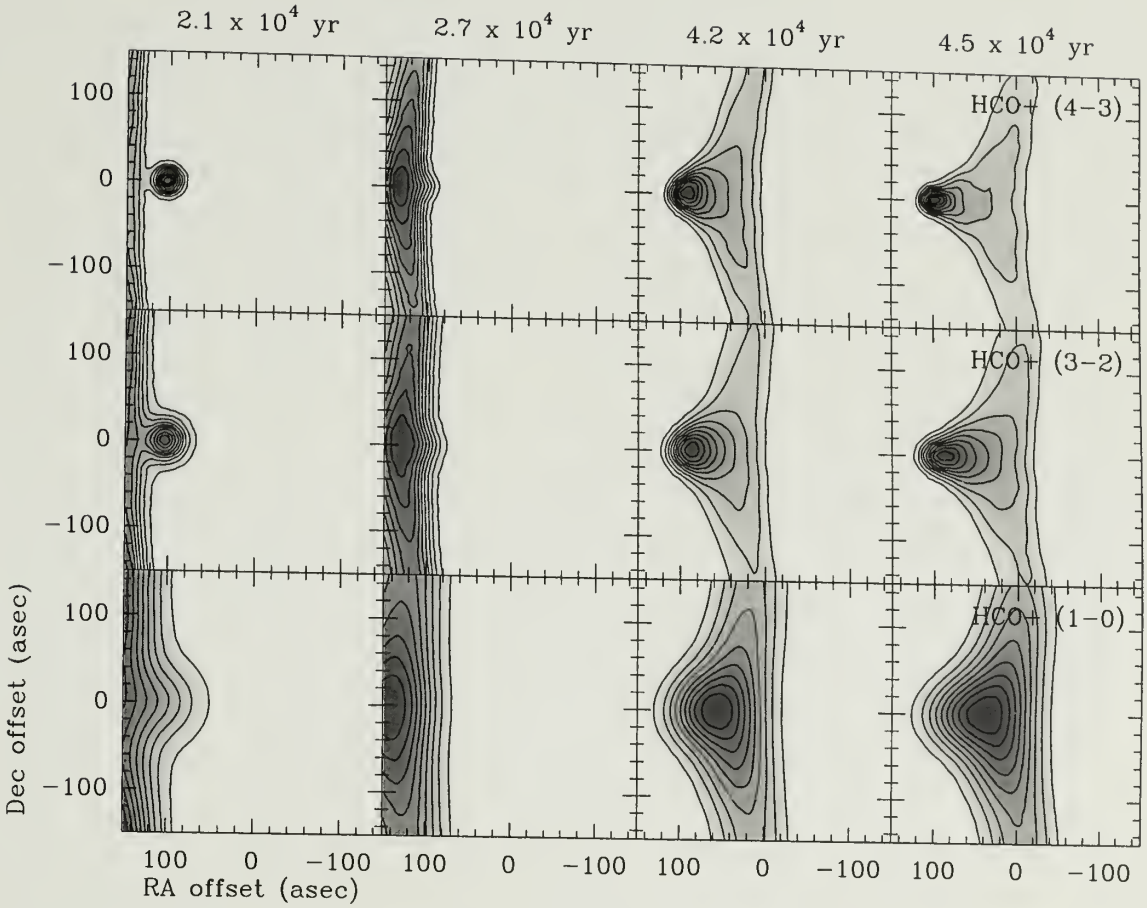

Figure 2.14 Integrated intensity maps of the HCO^+ emission from simulation Q. The contours run from 10% to 90% of the peak integrated intensity in increments of 10%.

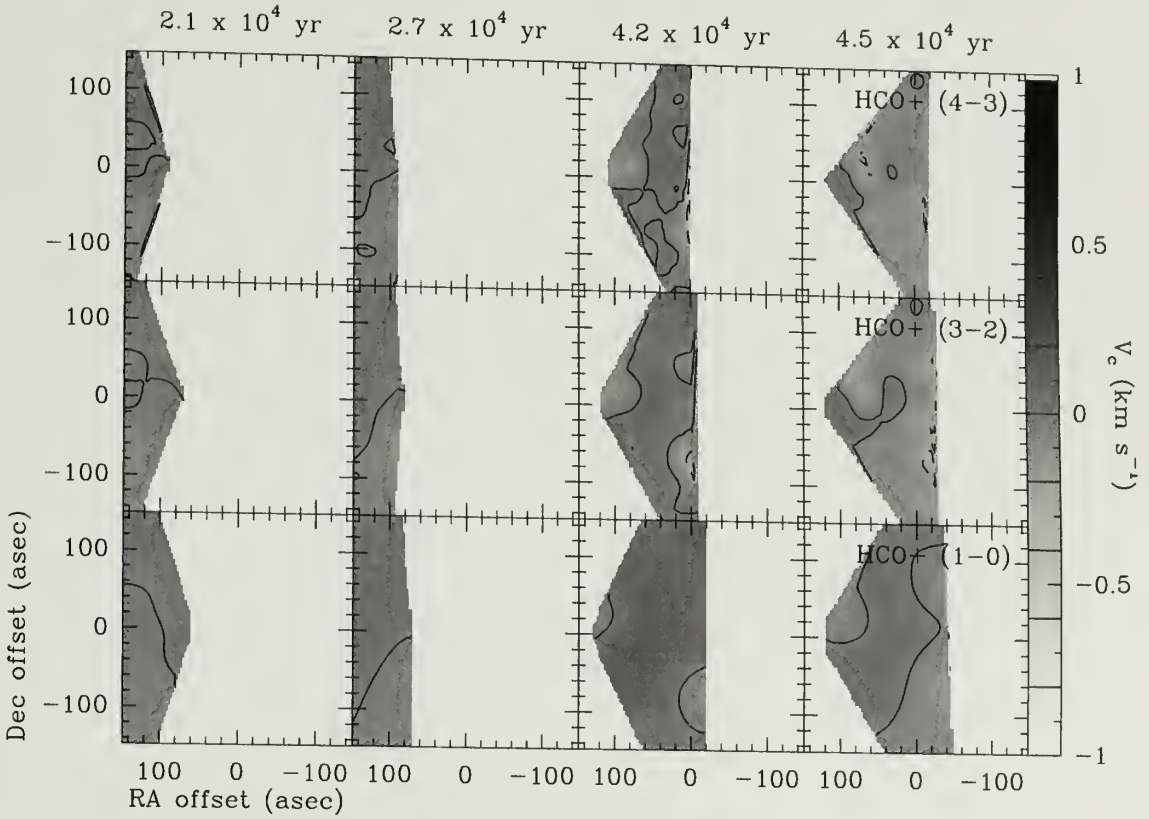

Figure 2.15 Centroid velocity maps of the HCO^+ line emission from simulation Q. The wedge to the right of the centroid maps indicates the velocities of the contours. Dashed contours indicate negative velocity centroids and solid contours indicate positive velocity centroids.

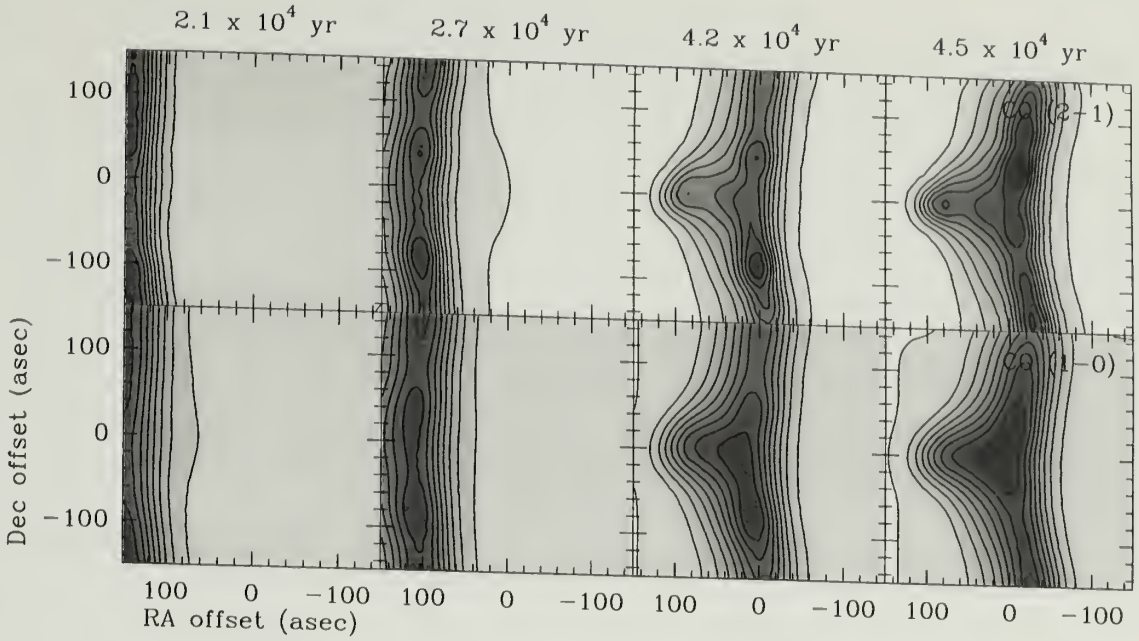

Figure 2.16 Integrated intensity maps of the CO emission from simulation Q. The contours run from 10% to 90% of the peak integrated intensity in increments of 10%.

left to right. Unlike in the HCO^+ integrated intensity maps, we can not differentiate the core from the swept up gas ridge in the CO integrated intensity maps at 2.1×10^4 years. There is also little curvature in the molecular gas ridge, so this may not be recognized as a bright-rimmed cloud in this timestep. At 2.7×10^4 years curvature is starting to develop in the CO integrated intensity maps. Some structure is also developing along the gas ridge, which becomes even more apparent at 4.2×10^4 years, when the cloud evolves to a type B morphology. The swept up gas ridge, and not the core, is the dominant source of CO emission at this time. The CO integrated intensity maps at 4.5×10^4 years appears similar to those at 4.2×10^4 years, however the position of the emission peaks in the CO ($J = 2 \rightarrow 1$) integrated intensity map has changed. This indicates that the knots we see in the molecular gas ridge may only be transient clumps which dissipate on short timescales.

2.4.4 Run K

VC hydrodynamic simulation run K simulates the effect of a 10 km s^{-1} wind on a 4 $M_{\odot}$ cloud core in a 1 μG effective magnetic field. This core does not collapse under the influence of the wind as the wind is not strong enough to induce collapse (VC). Figure 2.17 shows our modeled spectra for the cloud core position at various timesteps in the hydrodynamic simulation. We define the core position as the position where the $H^{13}CO^{+}$ ($J = 4 \rightarrow 3$) integrated intensity peaks which usually corresponds to the position of the densest gas clump. At 2.1×10^4 yr there are obvious self absorption dips in the HCO^{+} ($J = 1 \rightarrow 0$) and HCO^{+} ($J = 3 \rightarrow 2$) transitions. The lines are symmetric, so there is no significant infall motion at this stage. At 2.7×10^4 yr the lines have not changed much. This is because the swept up gas is not yet interacting significantly with the core. At 4.2×10^4 yr the swept up gas begins interacting with the core. Although the line profiles also seem similar to the two previous timesteps, some blue asymmetry has arisen in the HCO^{+} ($J = 3 \rightarrow 2$) and HCO^{+} ($J = 1 \rightarrow 0$) transitions indicating that infall may be occurring. Finally, at 7.2×10^4 yr, the lines are significantly changed. They all show a red asymmetry which may indicate that the core is flowing apart. The other noticeable trait of the final timestep is that these are the lowest emission intensities of all the hydrodynamic models' late timesteps. In those cases where the core becomes gravitationally bound the emission from the core tends to increase as the density increases, but this core does not become gravitationally bound, so the intensity remains low. The only caveat to this observation is that a very self absorbed line has a relatively low intensity, even if it does arise from a dense, gravitationally bound, core. An example of this was seen in the final timestep of run Q (Figure 2.13).

Figure 2.18 depicts the evolution over time of the HCO^{+} integrated intensity maps of VC simulation run K. The top row is the HCO^{+} ($J = 4 \rightarrow 3$) emission, the middle is the HCO^{+} ($J = 3 \rightarrow 2$) emission, and the bottom is the HCO^{+} ($J = 1 \rightarrow 0$) emis-

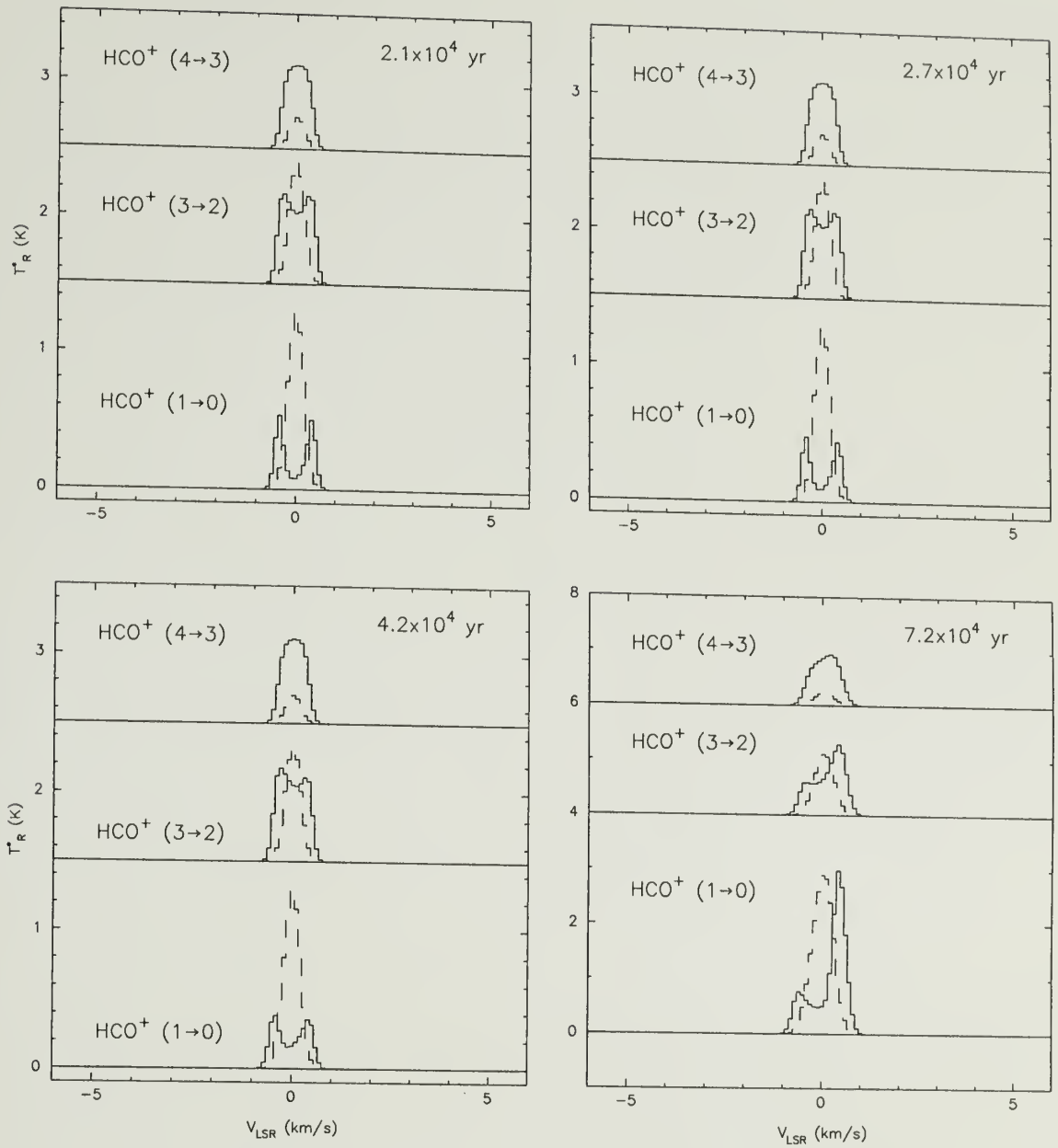

Figure 2.17 HCO^+ and $H^{13}CO^+$ line profiles at various time steps in simulation K. The solid line is the indicated HCO^+ transition, while the dashed line is the corresponding $H^{13}CO^+$ isotopic line. The isotopic line has been magnified relative to the main line by a factor of 5.

sion. Each column represents a different time step, evolving from left to right. The integrated intensity maps at 2.1×10^4 years and 2.7×10^4 years appear the same, with intensity peaking at the core position in all the HCO^+ transitions. The emission appears circularly symmetric around the core position, indicating that the molecular gas in the core is relatively undisturbed by the shock front at these timesteps. At 4.2×10^4 years the HCO^+ ($J = 4 \rightarrow 3$) integrated intensity map still appears undisturbed, but the HCO^+ ($J = 3 \rightarrow 2$) integrated intensity map has developed a slight asymmetry at the 10% of the peak intensity level. The HCO^+ ($J = 1 \rightarrow 0$) emission is profoundly effected by the swept up molecular gas ridge, though it still peaks at the core position. At 7.2×10^4 years the swept up gas is fully interacting with the core, and is forming a type A morphology in the HCO^+ integrated intensity maps. The molecular gas core is still the dominant source of emission in all the HCO^+ transitions. This simulation bucks the trend which we've seen so far in which the HCO^+ ($J = 4 \rightarrow 3$) emission is concentrated in the core at the final timestep only if the core is gravitationally bound. In the case of run O the core was torn apart by the speed of the ionized gas wind, however this case is different in that the wind is moving so slowly it does not induce collapse. In the case of a slowly moving wind the HCO^+ integrated intensity maps may not be a good a discriminating bound from unbound bright-rimmed cloud cores.

Figure 2.19 depicts the centroid velocity maps of the modeled HCO^+ spectral line profiles. As in the case of run Q, the centroid velocity maps do not have much structure over the length of the simulation. In this simulation, as in run Q, the cloud never evolves into a type C morphology. Our simulations indicate that significant centroid velocity structure does not appear until well into the type B morphology. Nevertheless, the HCO^+ ($J = 1 \rightarrow 0$) does show some organized evolution of the centroid velocity map. In the early timesteps (2.1×10^4 to 4.2×10^4 years) the center of the core has a slightly lower velocity centroid than the surrounding gas, but in

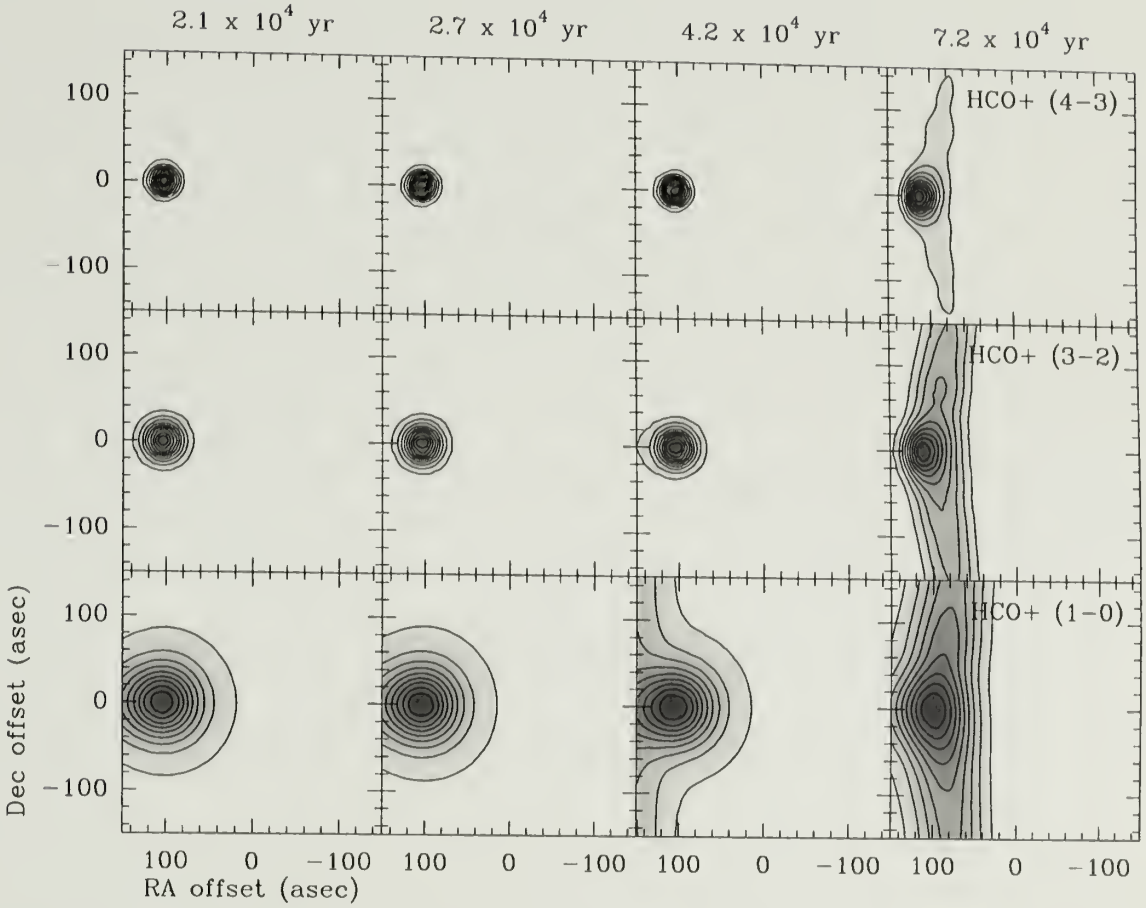

Figure 2.18 Integrated intensity maps of the HCO^+ emission from simulation K. The contours run from 10% to 90% of the peak integrated intensity in increments of 10%.

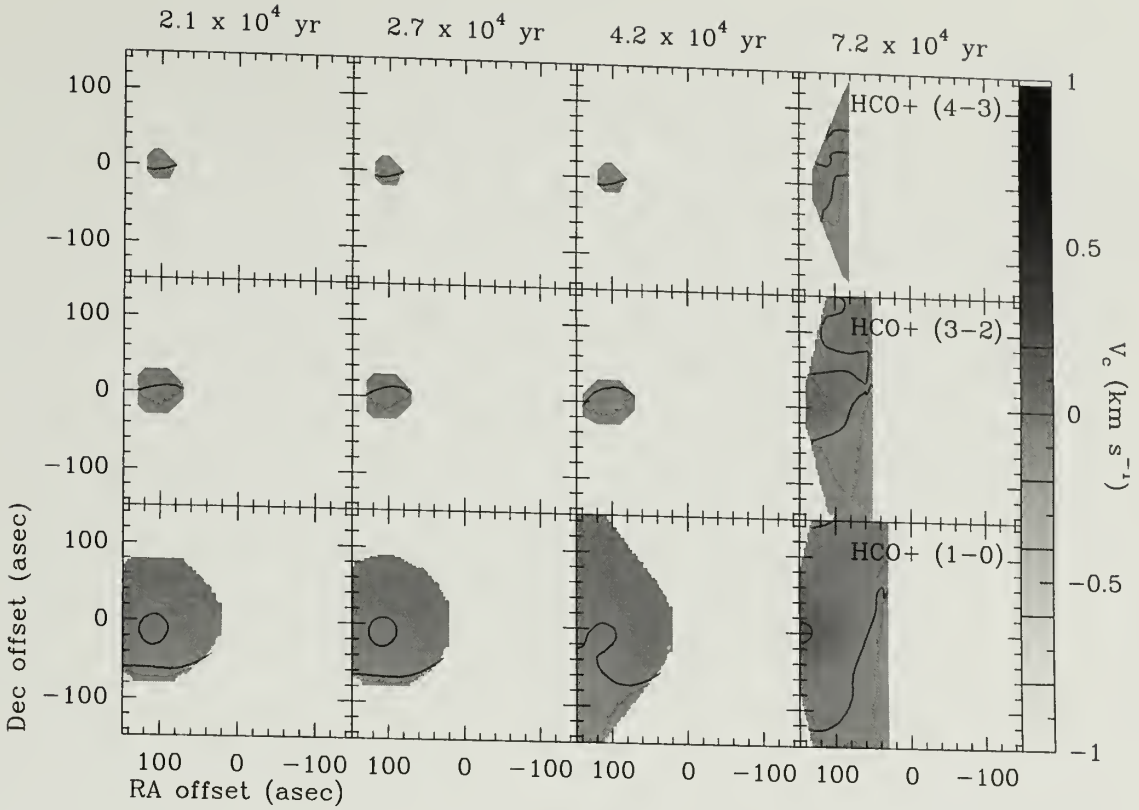

Figure 2.19 Centroid velocity maps of the HCO^+ line emission from simulation K. The wedge to the right of the centroid maps indicates the velocities of the contours. Dashed contours indicate negative velocity centroids and solid contours indicate positive velocity centroids.

the final timestep the core position has a higher centroid velocity than the rest of the cloud. This may be due initially to an blue asymmetric infall signature which is reverse in the final timestep as the gas is heated by the molecular gas ridge causing the core to dissipate.

Figure 2.20 depicts the evolution over time of the CO integrated intensity maps of VC simulation run K. The top row is the CO ($J = 2 \rightarrow 1$) emission, the bottom is the CO ($J = 1 \rightarrow 0$) emission. Each column represents a different time step, evolving from left to right. Although at the earliest timesteps (2.1×10^4 and 2.7×10^4 years) the interaction between the HCO^+ emission showed no sign of the interaction of the molecular gas with the shock front, the CO emission shows a truncation in the direction of the approaching shock front. At 4.2×10^4 years the CO integrated intensity

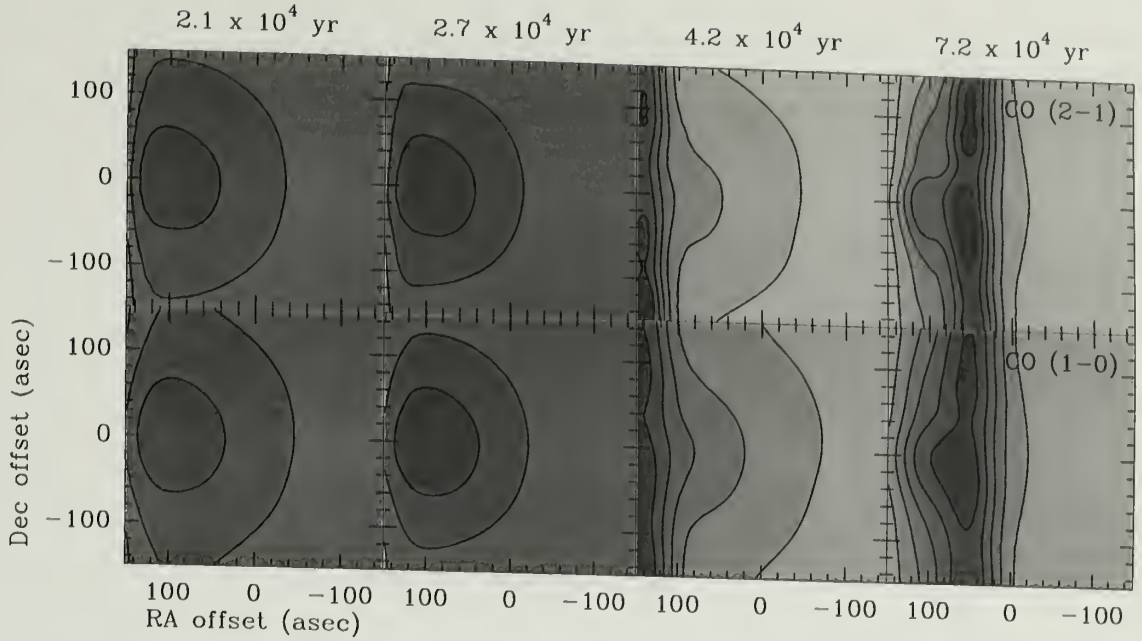

Figure 2.20 Integrated intensity maps of the CO emission from simulation K. The contours run from 10% to 90% of the peak integrated intensity in increments of 10%.

maps are significantly changed by the encroaching ridge of molecular gas swept up by the shock front. This ridge has become the dominant source of CO emission indicating that quite a column of gas is swept up by the slow-moving shock front. At the final timestep (7.2×10^4 years) the thin molecular gas ridge has passed the molecular core position. The CO integrated intensity maps are dominated by the emission from the molecular ridge, though the core results in an easterly extension to the CO ridge.

2.4.5 Run I

Simulation run I (VC) simulates the effect of a 10 km s^{-1} wind on a 20 $M_\odot$ cloud core in a 1 μG effective magnetic field. This core collapses into two gravitationally bound cores, which would eventually form a binary star system (VC). Figure 2.21 shows our modeled spectra for the cloud core position at various timesteps in the hydrodynamic models. Although two cores form, their angular separation is less than our smallest beam width. The line profiles in this simulation are quite complex, which is probably a result of two infall regions which overlap in velocity space. At 2.7×10^4 yr

there is some self absorption in the HCO^+ $(J = 4 \rightarrow 3)$ transition as well as the HCO^+ $(J = 3 \rightarrow 2)$ transition, and there is a red asymmetry. The HCO^+ $(J = 1 \rightarrow 0)$ transition looks like a narrow gaussian with wide wings. At 4.1×10^4 yr there are three peaks in the HCO^+ $(J = 4 \rightarrow 3)$ line, although the $H^{13}CO^+$ $(J = 4 \rightarrow 3)$ line appears to have only one peak and is rather symmetric. The other HCO^+ lines show a red asymmetry. This changes at 7.0×10^4 yr when the asymmetry in the HCO^+ $(J = 4 \rightarrow 3)$ and HCO^+ $(J = 3 \rightarrow 2)$ line is now blue, however the $H^{13}CO^+$ lines show significant structure as well, so we can not say from the molecular line emission alone if the resulting HCO^+ profiles are the result of radiative transfer effects or a superposition of clumps along the line of sight. In the final time step, 7.4×10^4 yr, both the HCO^+ and $H^{13}CO^+$ line profiles are very complex and show multiple peaks and troughs which are a combination of the superposition of the two cores along the line of sight as well as radiative transfer effects.

Figure 2.22 depicts the evolution over time of the HCO^+ integrated intensity maps of VC simulation run I. The top row is the HCO^+ $(J = 4 \rightarrow 3)$ emission, the middle is the HCO^+ $(J = 3 \rightarrow 2)$ emission, and the bottom is the HCO^+ $(J = 1 \rightarrow 0)$ emission. Each column represents a different time step, evolving from left to right. At 2.1×10^4 years the HCO^+ integrated intensity maps show a characteristic type A morphology. Each of the HCO^+ transitions has it's emission peaking at the core position with a relatively narrow ridge of swept up gas forming an emission ridge. The HCO^+ $(J = 1 \rightarrow 0)$ transition has a ridge which widens near the core position. At 2.7×10^4 years the HCO^+ emission in all the tracers continues to peak at the core position. The curvature of the swept up ridge is increasing as the cloud begins to evolve from a type A to a type B morphology. The curvature of the gas ridge continues to increase at 4.1×10^4 years. At this point the HCO^+ integrated intensity maps are in a type B morphology. The HCO^+ $(J = 4 \rightarrow 3)$ and HCO^+ $(J = 3 \rightarrow 2)$ emission is peaked at the core position. The HCO^+ $(J = 1 \rightarrow 0)$ emission peaks to the west

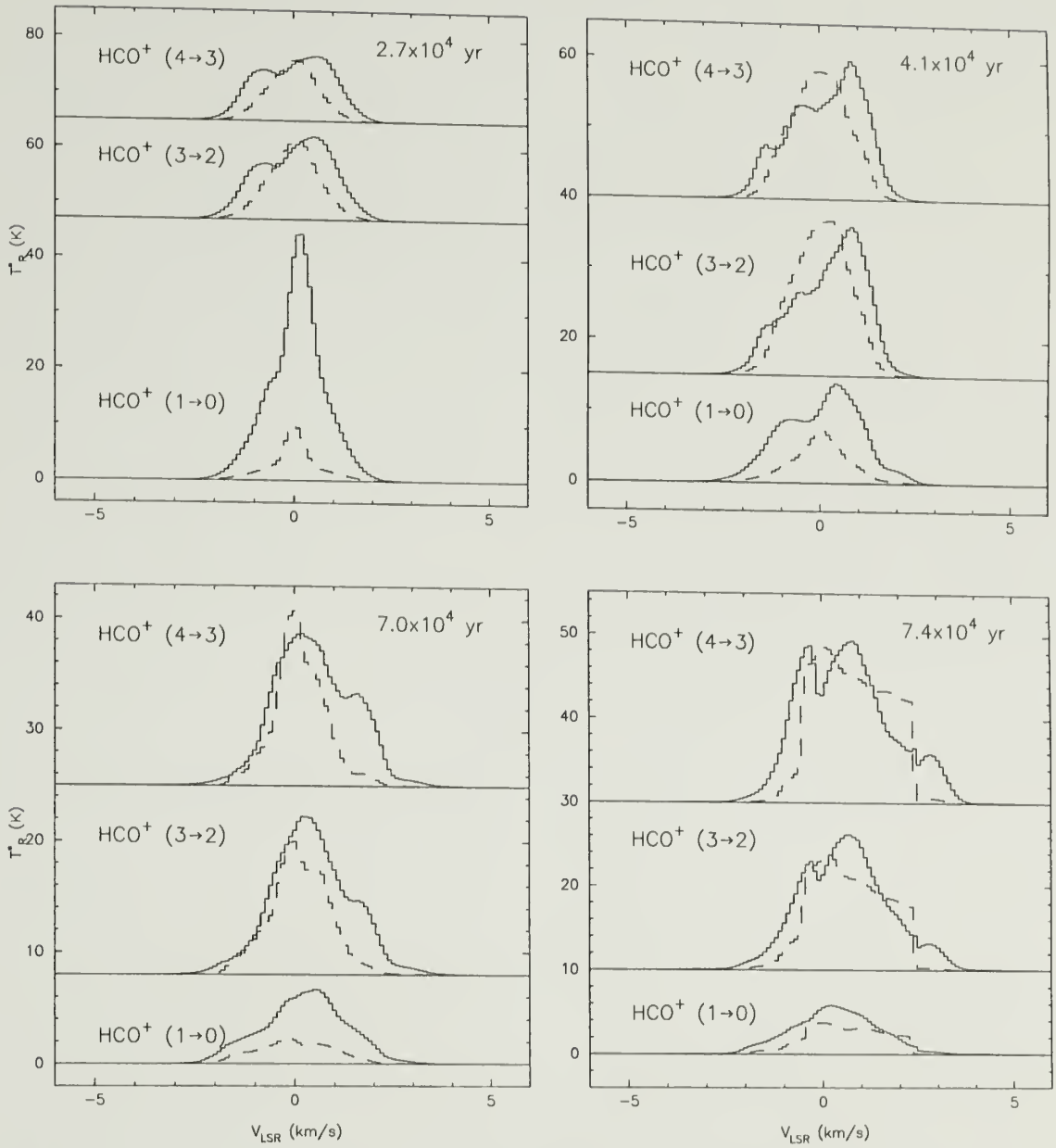

Figure 2.21 HCO^+ and $H^{13}CO^+$ line profiles at various time steps in simulation I. The solid line is the indicated HCO^+ transition, while the dashed line is the corresponding $H^{13}CO^+$ isotopic line. The isotopic line has been magnified relative to the main line by a factor of 10 at 2.7×10^4 yr and 4.1×10^4 yr, and by 5 at 7.0×10^4 yr and 7.4×10^4 yr.

of the core position. This is a result of the fact that more than half the molecular gas originally in the core is swept away by the wind. At 7.0×10^4 years the HCO^+ emission is in a type C morphology. The HCO^+ $(J = 4 \rightarrow 3)$ and HCO^+ $(J = 3 \rightarrow 2)$ emission continues to peak at the core position, although the core is elongated in the east-west direction. This may be due to the fact that dense gas continues to be stripped from the core at this time. There are also knots of emission visible in the tail indicating that the tail is not a smooth structure, but full of overdense ad underdense regions. The HCO^+ $(J = 1 \rightarrow 0)$ emission peaks approximately $100''$ to the west of the core tracing the gas swept from the core. At the final timestep $(7.4 \times 10^4$ years) the morphology in the HCO^+ integrated intensity maps remains a type C morphology. The HCO^+ $(J = 4 \rightarrow 3)$ and HCO^+ $(J = 3 \rightarrow 2)$ peaks remain at the core position, though they are much less elongated than in the previous timestep which may be an indication that the wind can no longer strip the molecular gas from the core. The head/tail emission contrast in the HCO^+ $(J = 4 \rightarrow 3)$ emission is also increasing as it did for the final timesteps of the other simulations of successful collapse. The HCO^+ $(J = 1 \rightarrow 0)$ integrated intensity map appears similar to the previous timestep.

Figure 2.23 depicts the centroid velocity maps of the modeled HCO^+ spectral line profiles. At early times $(2.1 \times 10^4$ and 2.7×10^4 years) there is relatively little variation in the centroid velocity across the cloud, however as the HCO^+ emission forms a type B morphology the variation in the centroid velocity increases. By 7.0×10^4 we see that there are knots within the tail of the cometary clouds with significantly different centroid velocities than that of the core. In the HCO^+ $(J = 1 \rightarrow 0)$ centroid velocity map we see that a velocity gradient is developing across the width of the cometary cloud. This is different than in all previous cases where a velocity gradient developed along the length of the cometary cloud. These trends continue into the next timestep $(7.4 \times 10^4$ years) with one curious note. The HCO^+ $(J = 3 \rightarrow 2)$ and

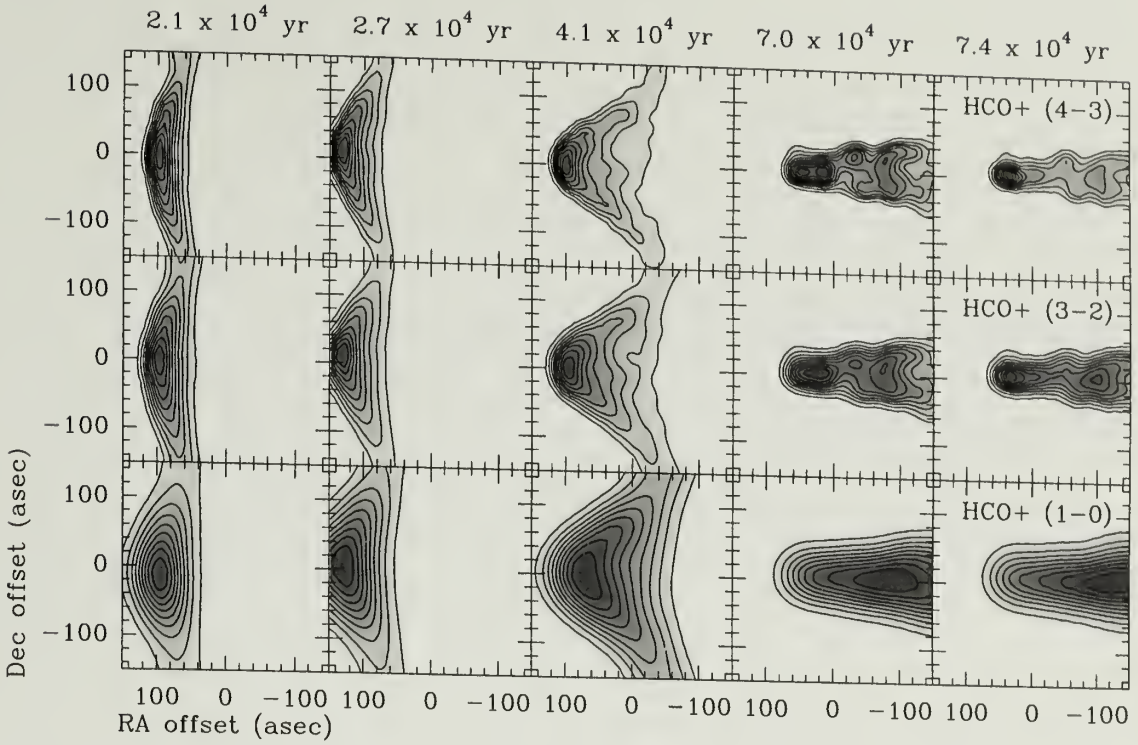

Figure 2.22 Integrated intensity maps of the HCO^+ emission from simulation I. The contours run from 10% to 90% of the peak integrated intensity in increments of 10%.

HCO^+ ($J = 1 \rightarrow 0$) velocity centroids diminish by quite a bit. This may indicate that along the entire length of the cometary cloud an infall signature has developed.

Figure 2.24 depicts the evolution over time of the CO integrated intensity maps of VC simulation run I. The top row is the CO ($J = 2 \rightarrow 1$) emission, the bottom is the CO ($J = 1 \rightarrow 0$) emission. Each column represents a different time step, evolving from left to right. At 2.1×10^4 years and 2.7×10^4 years the CO integrated intensity map is in a type A morphology. The CO ($J = 1 \rightarrow 0$) map appears to peak more sharply at the core position while the CO ($J = 2 \rightarrow 1$) integrated intensity map has a fairly broad peak along the molecular gas ridge. At 4.1×10^4 years the emission peaks of the CO integrated intensity maps have moved west of the core position. There are also now two CO integrated intensity peaks, one to the northwest of the core, the other to the southwest of the core. This can be explained by the fact that we are seeing a ring of dense gas being pushed from east to west by the wind. We

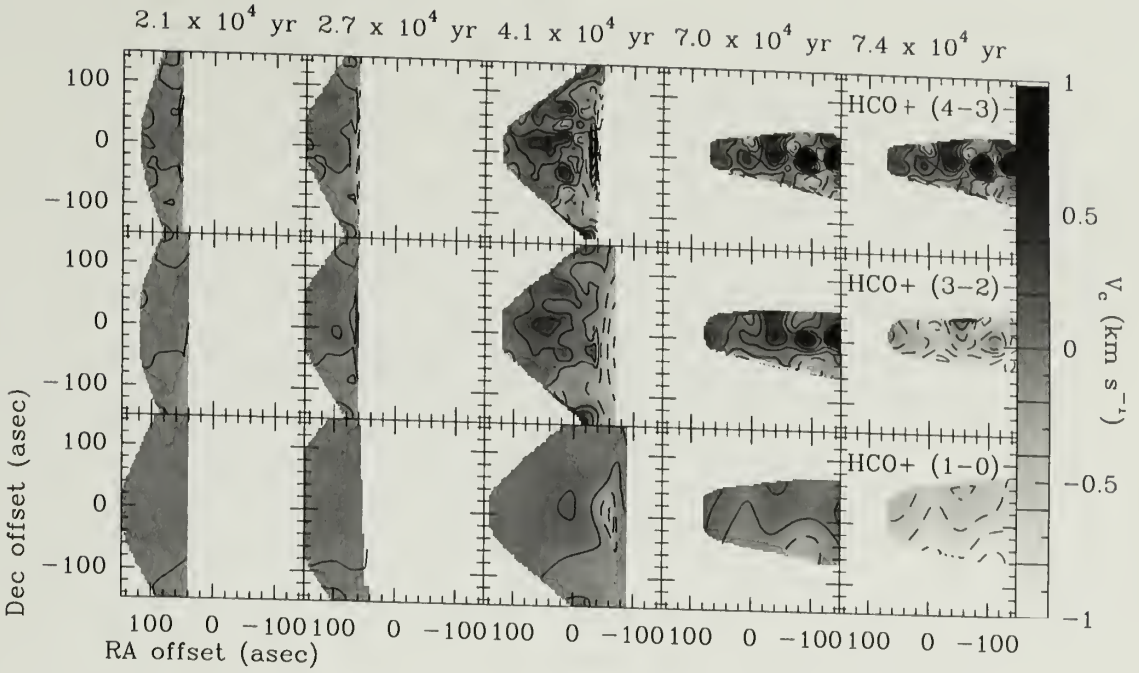

Figure 2.23 Centroid velocity maps of the HCO^+ line emission from simulation I. The wedge to the right of the centroid maps indicates the velocities of the contours. Dashed contours indicate negative velocity centroids and solid contours indicate positive velocity centroids.

see the ring edge on from our vantage point, and the CO, which tends to trace the column density of the gas, produces emission which peaks at the edges of the ring where the column density is the greatest. By 7.0×10^4 years the morphology is less interesting. The CO integrated intensity maps now are in a type C morphology. The dominant emission source is the tail of the cometary cloud, where much of the molecular gas has been swept up by the wind. At the last timestep (7.4×10^4 years) the CO integrated intensity map appears similar to the previous timestep, however a small CO ($J = 2 \rightarrow 1$) peak has developed at the core position.

2.5 The Effect of Observing Angle on Synthetic Observations

All of the proceeding synthetic observations have been projected such that the shock front moves parallel to the plane of the sky. Observed bright-rimmed clouds are probably not aligned exactly in this configuration. In order to study the effect

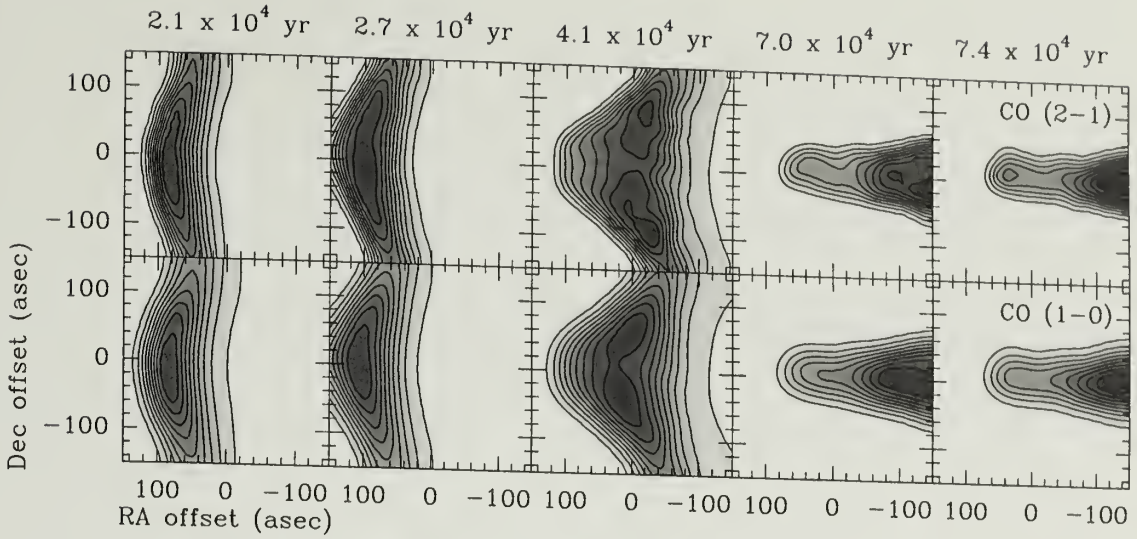

Figure 2.24 Integrated intensity maps of the CO emission from simulation I. The contours run from 10% to 90% of the peak integrated intensity in increments of 10%.

of different geometries we have reprojected VC simulation run F such that the angle between the plane of the sky and the direction of motion of the shock front is 35°. The shock front is approaching from the east and from the direction of the observer. In these cases the velocity imposed by the wind on the core includes a component in the direction of the line of sight. Run F is a simulation in which a 25 km s^{-1} wind causes a 3 $M_\odot$ cloud core to collapse into a self-gravitating object. This model was previously discussed in §2.4.1.

Figure 2.25 depicts the simulated HCO^+ line profiles towards the collapsing core for Run F viewed in this geometry. In the earliest timestep, 2.1×10^4 yr, we do not see blue asymmetry similar to that seem in Figure 2.5, however we do see a redshifted tail, and a second redshifted peak at 7 km s^{-1}. The presence of so much emission at relatively high redshift is due to the acceleration of molecular gas by the wind along the line of sight. The fact that the peak is still very close to 0 km s^{-1} indicates that the wind has not managed to accelerate the cloud core very much at this time. At 2.7×10^4 yr the HCO^+ line profiles have evolved. The overall intensity of the emission is much greater and the line peaks have become further

redshifted. The HCO^+ $(J = 4 \rightarrow 3)$ and HCO^+ $(J = 3 \rightarrow 2)$ line profiles peak at approximately 1.5 km s^{-1}, and although the HCO^+ $(J = 1 \rightarrow 0)$ line is very broad it does have a local maximum at that velocity. This corresponds to the emission from the core, which of course is still well traced by the submillimeter transitions. The remainder of the emission which is at higher velocities is from gas accelerated by the wind, which is also being excited by the interaction with the shock front. At 4.2×10^4 yr the gas surrounding the cloud core is mostly swept from the line if sight towards the cloud core, which results in less emission at high redshifts, though clearly a tail remains in all the HCO^+ emission profiles. The core emission is most prominent in the submillimeter transitions. Finally at 7.0×10^4 yr we see that the redshifted wing has emerged once again. Although initially puzzling, this component of the emission actually arises from fairly dense region of molecular gas which is being stripped from the core at this time. It is visible in the HCO^+ integrated intensity maps presented earlier (Figure 2.6) as the elongation in the westerly direction of the core. The blue side of these emission profiles up to the peak have similar shapes to those seen in Figure 2.5. Even the blue wing seen in the HCO^+ $(J = 1 \rightarrow 0)$ line profile in Figure 2.5 is reproduced in Figure 2.25.

Figure 2.26 depicts the evolution over time of the HCO^+ integrated intensity maps of VC simulation run F as projected in this geometry. One difference which is immediately apparent when comparing these results with those in Figure 2.6 is that the type A morphology for the first two timesteps is only visible in the HCO^+ $(J = 1 \rightarrow 0)$ integrated intensity map. The rotation by 35° of the molecular gas ridge has sufficiently spread the emission of the swept up molecular gas out so much that it is below the 10% level in the HCO^+ $(J = 4 \rightarrow 3)$ and HCO^+ $(J = 3 \rightarrow 2)$ maps. At 4.2×10^4 yr we see the cometary tail start to form, and both the HCO^+ $(J = 3 \rightarrow 2)$ and HCO^+ $(J = 1 \rightarrow 0)$ maps exhibit a type B morphology. In the final timestep, 7.0×10^4 yr, all the maps show a type C, cometary morphology. As in Figure 2.6 the

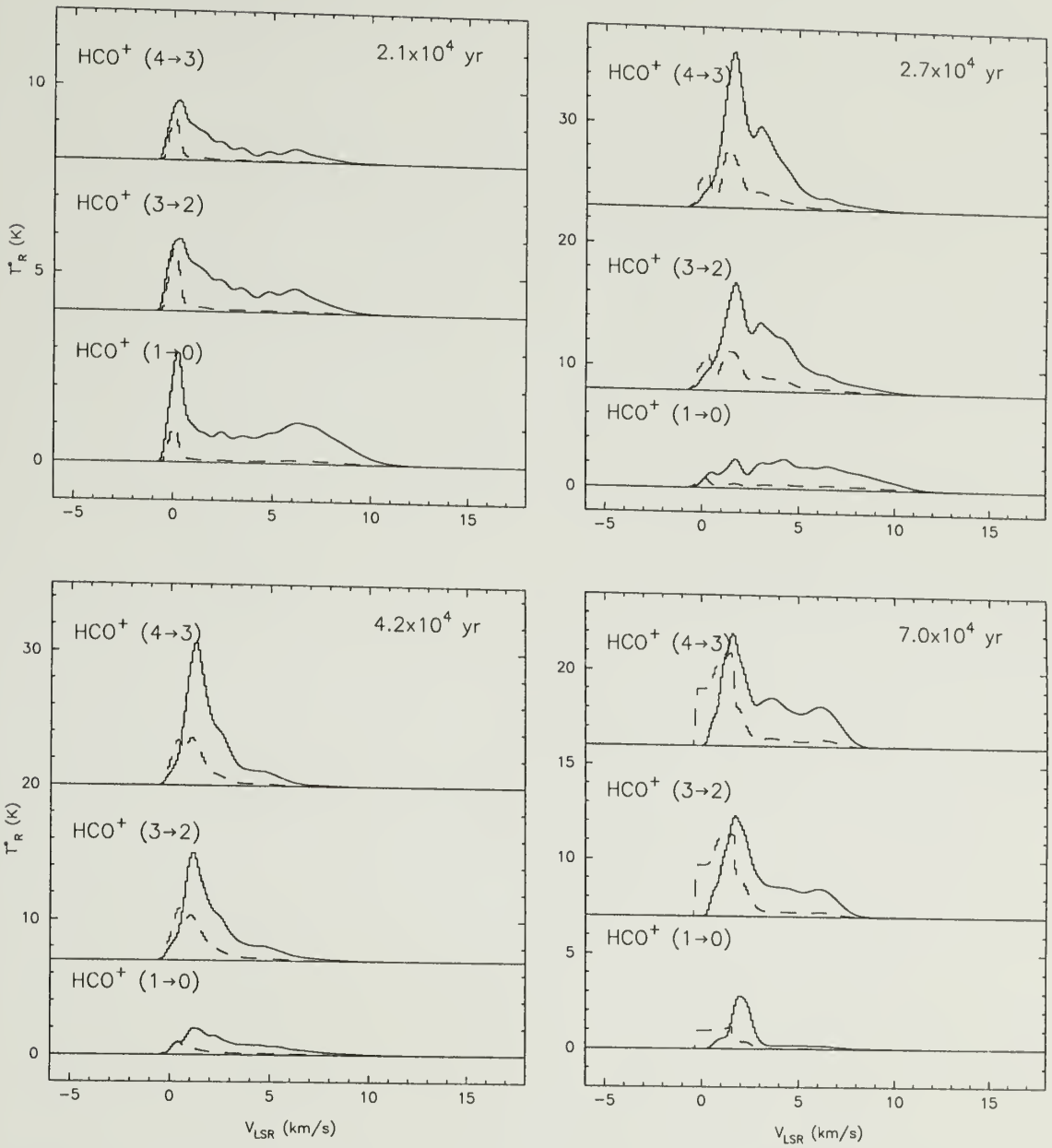

Figure 2.25 HCO^+ and $H^{13}CO^+$ line profiles at various time steps in simulation F observed at an angle of 35° from the plane of the sky. The solid line is the indicated HCO^+ transition, while the dashed line is the corresponding $H^{13}CO^+$ isotopic line. The isotopic line has been magnified relative to the main line by a factor of 5 at 2.1×10^4 yr, and by 10 in all other time steps.

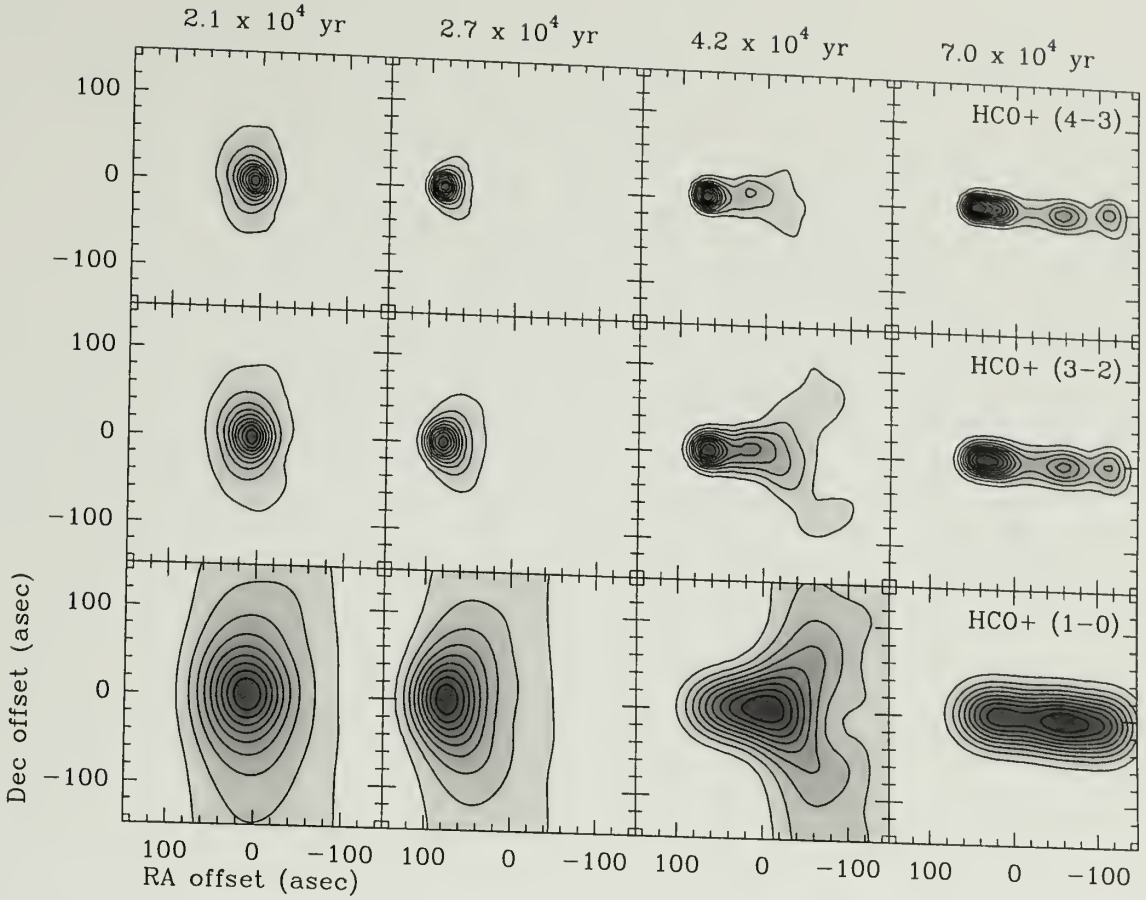

Figure 2.26 Integrated intensity maps of the HCO^+ emission from simulation F observed at an angle of 35° from the plane of the sky. The contours run from 10% to 90% of the peak integrated intensity in increments of 10%.

bulk of the HCO^+ $(J = 4 \rightarrow 3)$ and HCO^+ $(J = 3 \rightarrow 2)$ emission in the integrated intensity maps in the final timestep shown in Figure 2.26 arises from the core position, while the HCO^+ $(J = 1 \rightarrow 0)$ emission is spread more uniformly over the length of the cometary cloud.

Figure 2.27 depicts the evolution over time of the centroid velocity maps of the HCO^+ emission in this simulation. The velocity gradients are much more pronounced in this geometry because the wind is sweeping the molecular gas along the line of sight. The lowest velocities are near the core position for all the time steps. This is because the core slows the advance of the wind and it takes a lot of energy to accelerate the core. As a result all the lower density gas surrounding the core has a higher

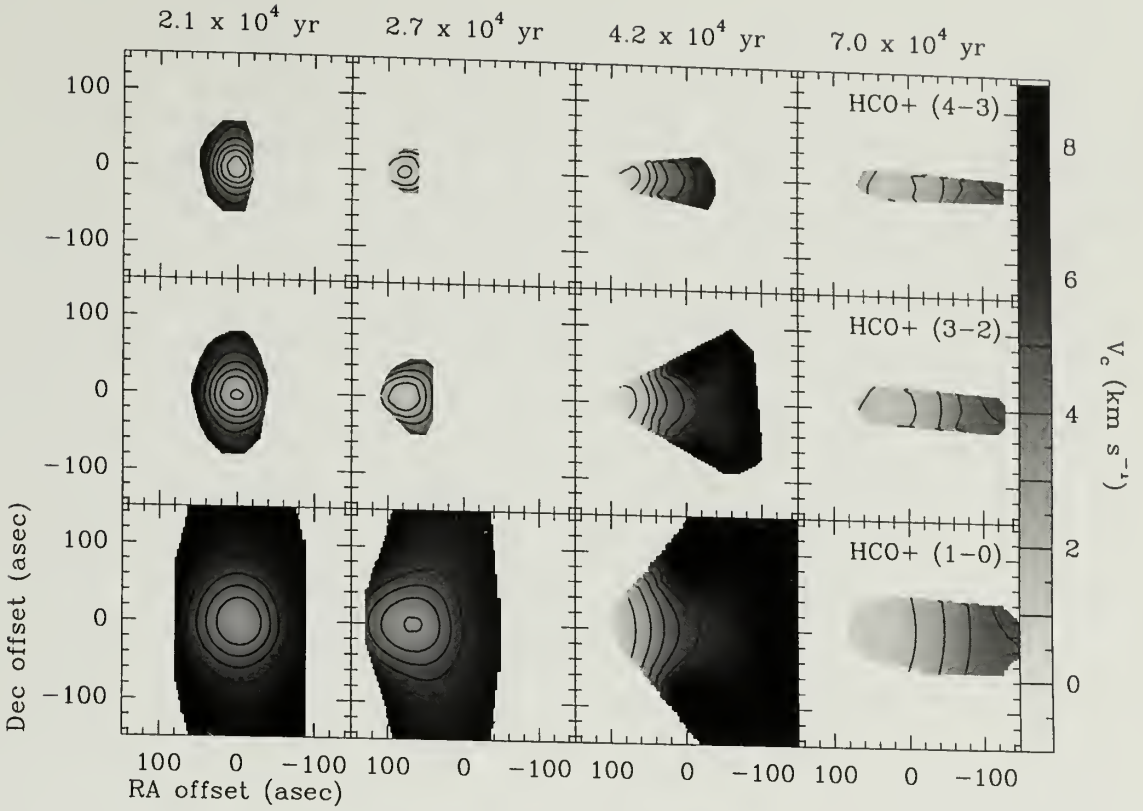

Figure 2.27 Centroid velocity maps of the HCO^+ line emission from simulation F observed at an angle of 35° from the plane of the sky. The wedge to the right of the centroid maps indicates the velocities of the contours. Dashed contours indicate negative velocity centroids and solid contours indicate positive velocity centroids.

velocity than the core. The molecular gas directly behind the core relative to the shock front also is not swept away as it is shielded from the wind by the core. At 2.1×10^4 yr in all the centroid maps we see increasing centroid velocities the further we move from the core position in any direction. The velocity gradient is larger in in the east-west direction than in the north-south direction. As the cloud evolves into a type C cometary cloud at 7.9×10^4 yr the velocity gradient to the west of the core gets smaller. This is because the gas in the tail is the predominant source of emission, and it has not been accelerated by the wind. The velocity gradient seen across the tail is due to other gas along the line of sight which has been accelerated by the wind.

Figure 2.28 depicts the evolution over time of the CO integrated intensity maps in this simulation. The top row is CO ($J = 2 \rightarrow 1$) emission, the bottom is

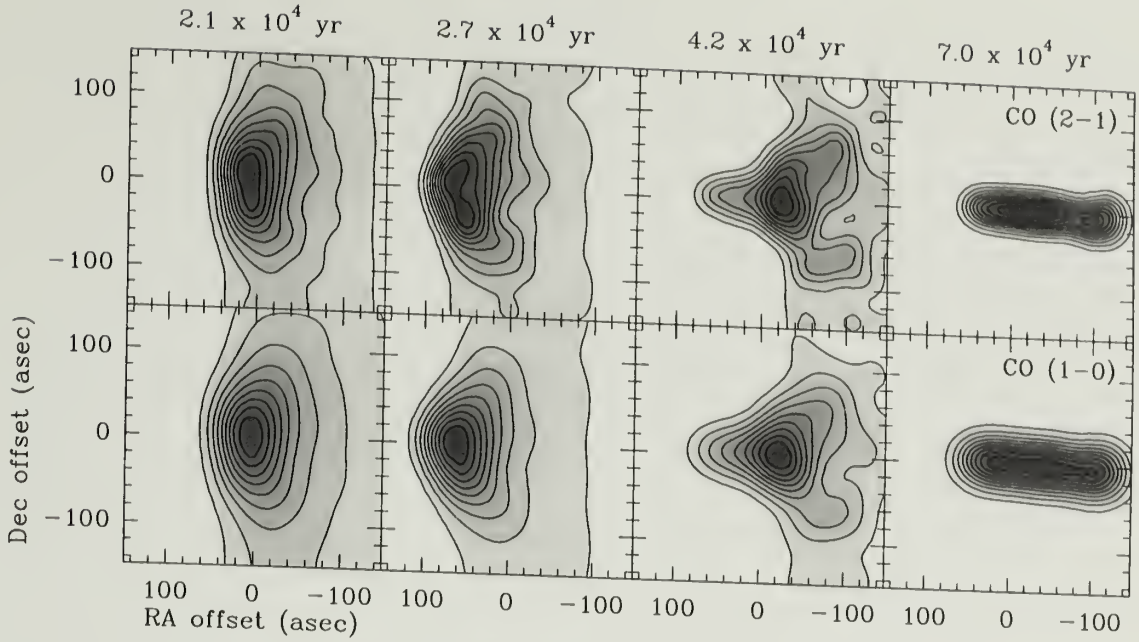

Figure 2.28 Integrated intensity maps of the CO emission from simulation F observed at an angle of 35° from the plane of the sky. The contours run from 10% to 90% of the peak integrated intensity in increments of 10%.

CO ($J = 1 \rightarrow 0$) emission. Each column represents a different time step evolving from left to right. At the earliest timestep (2.1×10^4 yr) the core as well as the ridge of swept up gas is traced by the CO emission. The ridge is not as well defined as in Figure 2.8 because of the viewing angle, though the type A morphology is still clear from these maps. At 2.7×10^4 yr the emission morphology is still type A, and is quite similar to that shown in Figure 2.8 as it is for the rest of the timesteps. At 4.2×10^4 yr the cloud attains a type B morphology as the wind sweeps the ridge of molecular gas past the core position. Finally at 7.0×10^4 yr the cloud is in a type C cometary morphology. Once again we see that the core is not prominent in the CO emission, but that the gas along the cometary cloud, including that stripped from the core, results in CO emission of nearly uniform intensity along the cloud.

2.6 Conclusions

Our investigation of the VC hydrodynamic wind-driven collapse models yields a better understanding of bright-rimmed clouds. We verify that bright-rimmed clouds do evolve over time from type A to type C as was inferred observationally by Ogura & Sugitani (1998). We find that the HCO^+ centroid velocity maps tend to be more ordered in bright-rimmed clouds in which the core becomes gravitationally bound, although we do not see consistent evidence of the spectral signature of infall in the cores of the modeled clouds in either the line profiles or the centroid velocity maps. We find that the line profiles in regions in which binaries are forming are much more complicated that those in which no stars form or in which only a single star is forming. Overall the line profiles in these regions are less self-absorbed and more symmetric than in isolated star forming regions, such as Bok globules. Our modeling suggests that it is easy to detect regions in which there are shock fronts interacting with cores because of this distinctive morphological sequence, but it is difficult to determine if these cores will collapse to form a star or if they are just transient overdense regions which will eventually dissipate under the influence of the shock front.

CHAPTER 3
OBSERVATIONS OF BRIGHT-RIMMED CLOUDS

3.1 Observational Approach

3.1.1 Source Selection

Potential triggered star formation regions have been selected from the catalog of bright-rimmed clouds with associated IRAS point sources by SFO. Each of these sources is associated with an HII region and is suspected to be forming stars via triggering. In all of these sources the geometry of the incoming shock region is obvious, as the shock emanates from the interface of the cloud and HII region. Since there are three different morphologies, or bright-rimmed cloud types, we decided to chose at least two of each type. We also chose nearby sources, both to get the best possible resolution, and because most Bok globules that have been studied have been nearby objects. The bright-rimmed clouds we observed have distances between 190 and 1900 pc, and include two type A bright-rimmed clouds (SFO 16 and SFO 18), three type B bright-rimmed clouds (SFO 4, SFO 13, and SFO 25), and two type C bright-rimmed clouds (SFO 20 and SFO 37). We cannot hope to resolve the cores of the more distant sources with single dish millimeter or submillimeter observations, however we do resolve the structure of the swept up molecular gas cloud surrounding the core, which is greatly affected by the impacting ionization front. The embedded IRAS sources in the selected bright-rimmed clouds have infrared luminosities which range from 5 to 1300 $L_{\odot}$, though all but one of the sources have a luminosity less that 110 $L_{\odot}$. These luminosities tend to be typical of low or intermediate mass star formation. Finally all but one of the bright-rimmed clouds were chosen to have the

IRAS colors of their embedded IRAS point source be consistent with Young Stellar Objects (YSOs) according to the color criteria presented in Beichman (1986). There are two exceptions to this rule. The first, SFO 4, was chosen because it is exceptionally nearby (190 pc). The second, SFO 13, was chosen because it is thought to be a region of cluster formation (Carpenter et al., 2000). Although SFO 4 and SFO 13 do not meet the IRAS color criteria of Beichman (1986) for inclusion in the population of YSOs, they do meet the criteria of Carpenter et al. (2000) for embedded star forming regions. Digitized Sky Survey observations of the bright-rimmed clouds are shown in Figure 3.1. In most of the optical images the bright rim is clearly visible, enclosed within the rim is the molecular cloud. Several of the sources show high extinction on one side of the rim indicating the presence of the molecular cloud. We have drawn in an arrow indicating the direction of propagation of the ionization front from the ionizing source creating the HII region.

In order to compare potential triggered star formation regions with quiescent star formation regions, we also observed Bok globules with embedded IRAS sources in their cores from the Clemens & Barvainis (1988) catalog of small, optically selected molecular clouds. We chose Bok globules with properties that are similar to our bright-rimmed clouds. They lie at distances between 250 and 2500 pc from us. They are believed to contain one star forming core with an embedded IRAS source, and their luminosities between 3 and 930 $L_{\odot}$. Observations of these sources allow for detailed comparisons between the observed properties of triggered and spontaneous star formation regions, and will allow us to isolate those observed properties unique to triggered star formation. The three Bok globules we have observed are B335, CB 3, and CB 224. The source list is summarized in table 3.1.

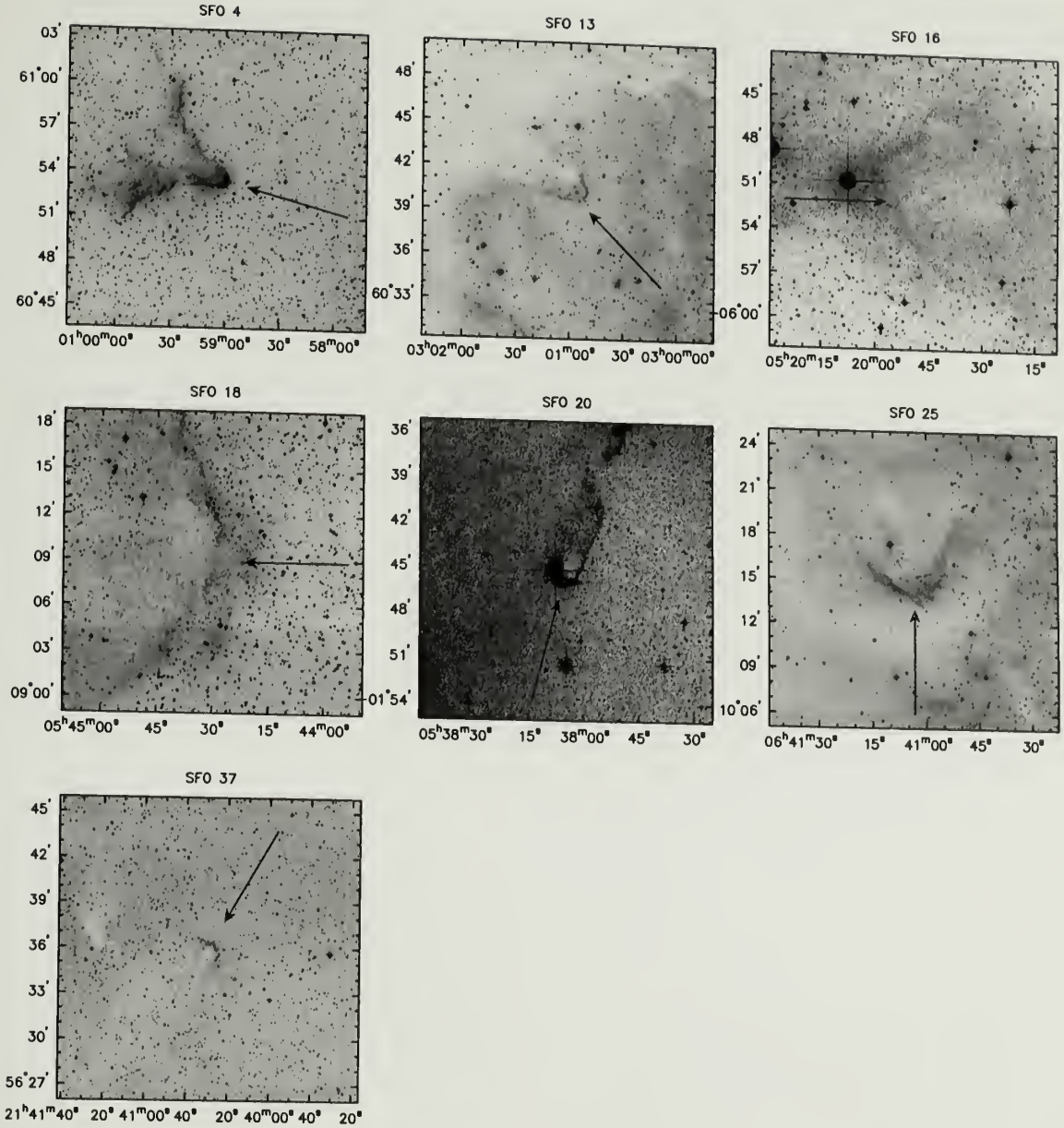

Figure 3.1 Digitized Sky Survey Image of SFO objects. These images show 20′ by 20′ sections of the sky centered on the embedded IRAS object. SFO used these images to classify these objects into their morphological scheme. The arrows indicates the direction of motion of the ionization front.

Table 3.1. Source List

Source	α(2000)	δ(2000)	Distance (pc)	Type	Associated HII Region	IRAS Source	IRAS Luminosity ($L_\odot$)
SFO 4	00h 59m 04.1s	60°53′32″	190[a]	B	S185	00560+6037	5.2
SFO 13	03h 01m 00.7s	60°40′20″	1900[a]	B	IC1848	02570+6028	1300
SFO 16	05h 19m 48.9s	–05°52′05″	400[a]	A	Barnard's Loop	05173–0555	16
SFO 18	05h 44m 29.8s	09°08′54″	400[a]	A	λ Ori	05417+0907	18
SFO 20	05h 38m 04.9s	–01°45′09″	400[a]	C	IC434	05355–0146	9.8
SFO 25	06h 41m 03.3s	10°15′01″	780[a]	B	NGC2264	06382+1017	100
SFO 37	21h 40m 29.0s	56°35′58″	750[a]	C	IC1396	21388+5622	110
B335	19h 37m 01.4s	07°34′02″	250[b]	Bok	none	19345+0727	2.6
CB 3	00h 28m 46.0s	56°42′06″	2500[c]	Bok	none	00259+5625	930
CB 224	20h 36m 17.2s	63°53′15″	450[c]	Bok	none	20355+6343	3.9

[a]Sugitani et al. (1991)

[b]Tomita et al. (1979)

[c]Launhardt & Henning (1997)

Table 3.2. Observed Transitions

Transition	Telescope	Frequency (GHz)	Velocity Res. (km s^{-1})	Beam Size ($''$)
$H^{13}CO^+(J = 1 \rightarrow 0)$	FCRAO	86.754330	0.068	56
$HCO^+(J = 1 \rightarrow 0)$	FCRAO	89.188523	0.066	54
$N_2H^+(J = 1 \rightarrow 0)$	FCRAO	93.173777	0.063	52
CO $(J = 1 \rightarrow 0)$	FCRAO	115.271203	0.203	46
CO $(J = 2 \rightarrow 1)$	HHT	230.538471	0.325	32
$H^{13}CO^+(J = 3 \rightarrow 2)$	HHT	260.557619	0.288	29
$HCO^+(J = 3 \rightarrow 2)$	HHT	267.557625	0.280	28
$H^{13}CO^+(J = 4 \rightarrow 3)$	HHT	346.998531	0.216	22
$HCO^+(J = 4 \rightarrow 3)$	HHT	356.734281	0.210	21
$H^{13}CO^+(J = 4 \rightarrow 3)$	CSO	346.998531	0.042	22
$HCO^+(J = 4 \rightarrow 3)$	CSO	356.734281	0.040	21

3.1.2 Choice of Molecular Transitions

One cannot obtain a complete picture of the physical conditions in a star forming cloud by observing one molecular line. It is only by combining observations of several molecular line transitions, sensitive to various physical conditions, that one can approach an accurate physical representation of the star forming cloud. As a result we chose several molecular transitions, in both the millimeter and submillimeter wave bands, in order to probe the conditions we felt would provide us with a basis for comparing bright-rimmed clouds with Bok globules. The transitions we observed are summarized in table 3.2.

CO has traditionally been the main tracer of molecular clouds. It has a fairly high abundance and a low critical density, making it a very useful tracer of molecular gas. Our observations of CO were driven by the fact that both the CO $(J = 1 \rightarrow 0)$ and the CO $(J = 2 \rightarrow 1)$ emission are good tracers of molecular outflows. $HCO^+$is a good tracer of moderate density ($\geq 10^4$ cm^{-3}). We observe the millimeter HCO^+ $(J = 1 \rightarrow 0)$ line to trace the morphology of the molecular gas swept up by

the ionization front. The submillimeter HCO^+ ($J = 3 \rightarrow 2$) and HCO^+ ($J = 4 \rightarrow 3$) trace the denser clumps within the swept up gas. HCO^+emission in all three tracers tends to be optically thick in the cores, making it a good tracer of infall as discussed in §4.2. N_2H^+ has been shown to be a good tracer of the dense core material as it can only form in well-shielded regions (Turner, 1995). N_2H^+ also remains relatively undepleated in cores (Bergin & Langer, 1997), making it especially useful in probing the densest regions of star forming clouds. The N_2H^+ ($J = 1 \rightarrow 0$) transition has seven well measured hyperfine components resulting from the interaction of the molecular electric field gradient and the electric quadrupole moments of the nitrogen nuclei (Caselli et al., 1995). These components can be used to determine the optical depth of N_2H^+ from which we can derive the column density of N_2H^+. From this measurement we can infer the density of star forming cores.

3.1.3 Presentation of the Data

In §3.3 we will discuss our observations of each source in a systematic way. This section describes the order in which various observations will be described and also points out various features which we look for in these sources. For each source we present figures illustrating the line profiles at the IRAS source position, an integrated intensity map of each tracer which we mapped, a map of the centroid velocity of the HCO^+ ($J = 1 \rightarrow 0$) transition, and a map of the molecular outflow if one is detected. Our rationale for presenting these figures is discussed below.

We begin by presenting the central line profiles of all the observed molecular transitions. These profiles are taken at the position of the IRAS source. There are several features in the line profiles which are of interest to us. The CO lines often have broad low intensity features called wings. These wings, which are especially prominent in the CO ($J = 2 \rightarrow 1$) transition, are usually the result of an outflow from the forming protostellar object. These outflows are often bipolar and are thought

to arise from megnetohydrodynamic winds driven by infall and interaction with the forming star's surrounding disk (see Bachiller (1996) and references therein). The shape of the line profile can also be of interest. The HCO^+ transitions often have profiles which deviate significantly from gaussian shapes at line center. This is due to the high optical depth which results in self-absorption near the line center. Often this results in a profile with two distinct peaks. When this is indeed the result of self-absorption, the lower abundance $H^{13}CO^+$ lines are often still optically thin and tends to show their greatest intensity at a velocity between the twin peaks of their self-absorbed isotopomer HCO^+. The relative size of each peak often indicates the kinematics of the gas within the beam. When the gas is collapsing to a point within the beam, the red-shifted gas is preferentially self-absorbed leaving a more intense blue-shifted peak and an overall blue-asymmetry with respect to the $H^{13}CO^+$ line. The reverse is true for gas expanding from a point within a beam (Snell & Loren, 1977; Zhou, 1992, 1995).

The integrated intensity maps provide a look at the two-dimensional morphology of the molecular cloud and cores as seen by the different tracers we mapped over the region surrounding the IRAS sources. The CO integrated intensity map gives a global look at the molecular gas in the region. One thing to note in the bright-rimmed clouds we observe is that the boundary between the molecular cloud and the ionized gas is very sharp and well traced by the CO. The HCO^+ tends to trace denser regions, but is also excited by shocks. As a result HCO^+ ($J = 1 \rightarrow 0$) tends to trace both the star forming cores as well as the rim of the ionization front. The higher level HCO^+ transitions tend to trace the dense gas. We overlay the N_2H^+ half-power contour on the integrated intensity map of a higher level HCO^+ transition in order to show the correspondence between the dense gas traced by N_2H^+ and that traced by HCO^+. There is often good agreement between the two tracers. Following the integrated intensity maps we present HCO^+ ($J = 1 \rightarrow 0$) centroid velocity maps for most of the

sources. Centroid velocity maps have been shown to be very effective in disentangling the underlying velocity fields in regions of complex kinematics (Narayanan & Walker, 1998). Often there is a velocity gradient which may correspond to rotation of the cloud or be a result of acceleration of the molecular gas due to the rocket effect which arises at the molecular cloud boundary.

The kinematic signature suggested by the HCO^+ is often interesting when compared to the integrated intensity maps of the CO outflows, which we present next for many of the sources we observe. Often the bipolar outflow we detect in CO is perpendicular to the velocity gradient we detect in HCO^+. This is evidence that we may be detecting rotation along the direction predicted in current models of star formation. We do not have the angular resolution, however, to probe this rotation down to the small scales of the star forming core.

3.2 Observations

3.2.1 FCRAO 14m

We performed observations at the Five College Radio Astronomy Observatory[1] (FCRAO) 14 m telescope over the 1999–2000 and 2000–2001 observing seasons using the Second Quabbin Observatory Imaging Array (SEQUOIA) 16-beam array receiver, and the Focal Plane Array Autocorrelation Spectrometers (FAAS) which consists of 16 autocorrelating spectrometers. A summary of the observed molecular line transitions is shown in table 3.2. The $C^{18}O$, HCO^+, $H^{13}CO^+$, and N_2H^+ transitions were observed using the frequency-switched mode, while CO was observed by position switching to a region that was reasonably clear of CO emission, though some CO contamination was found and considered acceptable in the offset positions as long as it was well separated in velocity from the line of interest. The $HCO^+$and $H^{13}CO^+$ were frequency folded

[1]FCRAO is supported in part by the National Science Foundation under grant AST 01-00793.

and 3rd order baselines were removed, while for the N_2H^+ data a 4th order baseline was used. A 2nd order baseline was subtracted from the position-switched CO data. HCO^+ and N_2H^+ were mapped with half-beam spacing, while CO and $H^{13}CO^+$ were mapped with full-beam spacing. The extent of the region mapped varies depending on the spatial extent of the source's emission.

3.2.2 HHT 10m

We also performed submillimeter observations in April and December 2000 and in April 2001 with the 10 m Heinrich Hertz Telescope[2] (HHT). CO $J = 2 \rightarrow 1$, HCO^+, and $H^{13}CO^+ J = 3 \rightarrow 2$ observations were conducted using the facility 230 GHz SIS receiver, while HCO^+ and $H^{13}CO^+$ observations were conducted using the facility dual polarization 345 GHz SIS receiver. Several backends were used simultaneously, including a 1 GHz wide ($\sim$ 1 MHz resolution) acousto-optical spectrometer (AOS), and three filterbanks with 1 MHz, 250 kHz, and 62.5 kHz resolutions. The results presented in this thesis were processed using the 250 kHz filterbank. All observations were position-switched, and second order baselines were removed. $H^{13}CO^+$ observations were made of the star forming core at the IRAS source position, while HCO^+ and CO observations were made using the on-the-fly (OTF) mapping technique. Observations of $120'' \times 60''$ regions in OTF mode were combined into maps of various spatial extents depending on the source.

3.2.3 CSO 10.4m

We observed B335 in May of 1996 at the Caltech Submillimeter Observatory[3] (CSO). HCO^+ ($J = 4 \rightarrow 3$) mapping was performed using the OTF mapping tech-

---

[2]The HHT is operated by the Submillimeter Telescope Observatory (SMTO), and is a joint facility for the University of Arizona's Steward Observatory and the Max-Planck-Institut für Radioastronomie (Bonn).

[3]The CSO is operated by the California Institute of Technology under funding from the National Science Foundation, grant number AST 93-13929.

nique. The OTF data was gridded into 49 positions with a spacing of 10″. $H^{13}CO^+$ ($J = 4 \rightarrow 3$) was observed at the IRAS source position. All observations were carried out with low-noise SIS waveguide receivers and a 1000 channel, 50 MHz wide acousto-optical spectrometer. The main beam efficiency at 345 GHz is ~ 0.65. Calibration of observations was done by the chopper wheel technique.

3.3 Results

3.3.1 Bright-Rimmed Clouds

3.3.1.1 SFO 4

SFO 4 is a bright-rimmed cloud with a type B morphology on the edge of the HII region S185 (γ Cas) (SFO). IRAS source 00560+6037 is embedded within SFO 4. This IRAS source has been classified by SFO as having IRAS colors consistent with hot cirrus sources, and not a forming or newly formed star (SFO). However according to the criteria of Carpenter et al. (2000) SFO 4 fits the IRAS color profile of an embedded star forming region. SFO 4 is nearby (190 pc), and has no known associated outflows or HH objects.

Figure 3.2a shows the spectra of our observations towards the IRAS source in SFO 4. Although $H^{13}CO^+$ ($J = 1 \rightarrow 0$) was not detected, our observations limit the integrated intensity of that transition to less that 0.037 K km s^{-1}. Based on this limit, and the integrated intensity measurement of HCO^+ ($J = 1 \rightarrow 0$), and an assumed $C/^{13}C$ abundance ratio of 64 we derive an upper limit to the column density of HCO^+ to be 2×10^{13} cm^{-2}. The line profiles appear fairly gaussian, in all the observed transitions, with nearly identical centroid velocities. None of the isotopic lines of either CO or HCO^+ were detected.

Figure 3.3 shows the HCO^+ and CO integrated intensity maps. Neither the CO ($J = 1 \rightarrow 0$) map, nor the HCO^+ maps show much structure. In the CO ($J = 1 \rightarrow 0$) map and the HCO^+ ($J = 1 \rightarrow 0$) map the cloud core surrounding the embedded

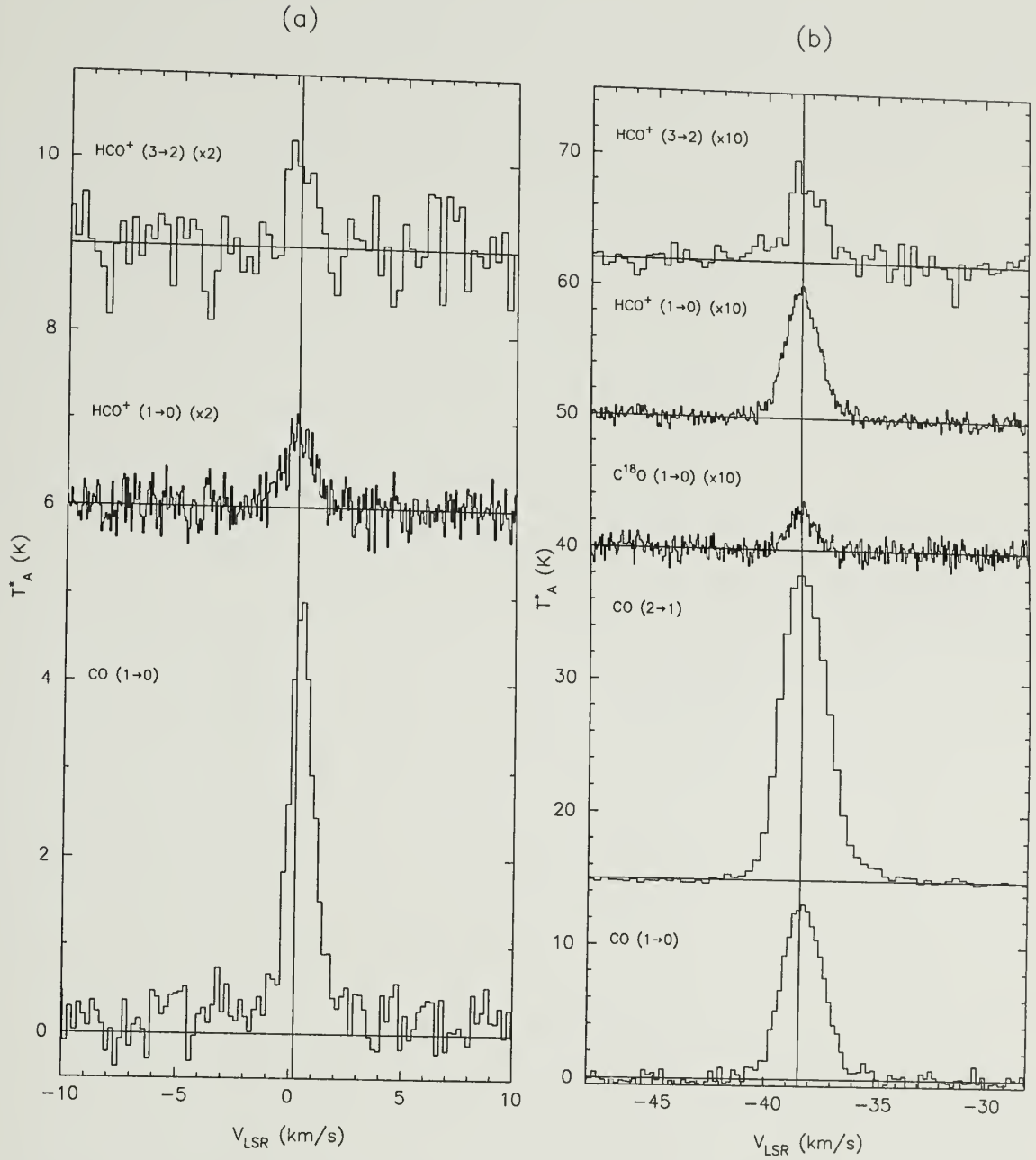

Figure 3.2 Line profiles of molecular transitions in the direction of the central IRAS source of SFO 4 (a) and SFO 13 (b).

IRAS source is visible, but no gas traces the ionization front or the elephant trunk morphology seen in the DSS image in Figure 3.1. The HCO^+ ($J = 3 \rightarrow 2$) map shows only one point whose integrated intensity is above 1.0 K km s^{-1}, the three sigma threshold for the map. This source is unusually weak compared to the other sources in the sample, which is unfortunate as it is also the nearest source in the sample.

3.3.1.2 SFO 13

SFO 13 is classified as a type B bright-rimmed cloud by SFO. Figure 3.1 shows the elephant trunk morphology characteristic of type B clouds. The initially cometary head of the cloud broadens into a wider structure as one follows the cloud away from the ionizing source. SFO 13 borders the HII region IC1848, and lies at a distance of 1.9 kpc from us, making it the most distant SFO source in the sample. A recent near-infrared survey reveals $\sim$ 20 point sources whose spectral energy distributions are consistent with pre-main-sequence stars (Sugitani et al., 1995, 1999). K' band observations by Carpenter et al. (2000) also confirm the presence an embedded stellar cluster in this molecular cloud. These sources are distributed preferentially towards the HII region with respect to the IRAS source, and are probably older than the IRAS source indicating that this cloud may be an example of small scale sequential star formation.

The millimeter and submillimeter line profiles for SFO 13, shown in Figure 3.2b, are all fairly gaussian and also peak at approximately the same velocity. This is not entirely unexpected as the average infall region for individual cores in a star formation region is smaller than the FCRAO beamwidth, which is 0.5 pc at this distance, and the HHT beamwidth, of 0.3 pc, making it difficult to detect infall. The CO ($J = 2 \rightarrow 1$) line strength is almost twice as much as that of CO ($J = 1 \rightarrow 0$). This intensity difference may be due to excitation effects, but may also be the result

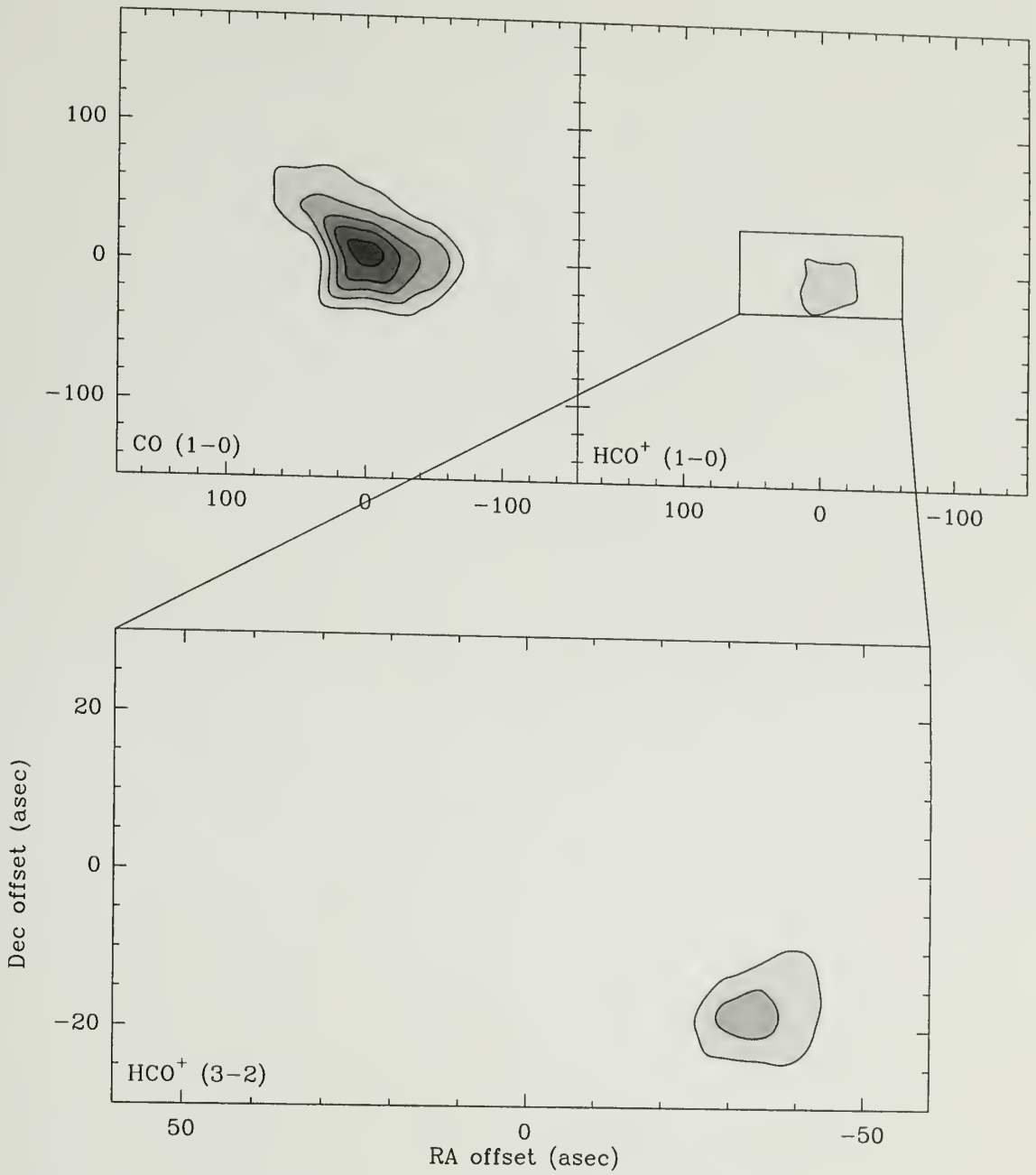

Figure 3.3 Integrated intensity maps of SFO 4. The IRAS source 00560+6037 is located at the center of each map. The CO ($J = 1 \rightarrow 0$) map has a lowest contour of 1.9 K km s^{-1} (3σ) and increments of 1.3 K km s^{-1} (2σ). The HCO$^+$ ($J = 1 \rightarrow 0$) map has a lowest contour of 0.6 K km s^{-1} (3σ) and increments of 0.2 K km s^{-1} (1σ). The HCO$^+$ ($J = 3 \rightarrow 2$) map has a lowest contour of 0.7 K km s^{-1} (2σ) and increments of 0.3 K km s^{-1} (1σ).

of the small angular size of the core. Since the CO ($J = 2 \rightarrow 1$) transition is observed with a much smaller beam than the CO ($J = 1 \rightarrow 0$) transition, the beam dilution is much greater for the lower transition and can have significant effects on the intensities observed with such distant sources. The HCO^+ and $C^{18}O$ line profiles are all fairly gaussian. N_2H^+ ($J = 1 \rightarrow 0$) was not detected in this source, down to an rms level of 0.017 K km s^{-1}.

Although the spatial resolution of our observations are not good enough to trace individual infall regions, the overall gas morphology is resolved by the beam. Figure 3.4 shows integrated intensity maps of various transitions and isotopes of CO and HCO^+. The CO ($J = 1 \rightarrow 0$) shows a distinct head, located at the IRAS source position upon which the map is centered. Lower intensity CO ($J = 1 \rightarrow 0$) emission continues from the core and spreads out to the north-east of the image, similar to the elephant trunk morphology seen in the optical (Figure 3.1). This is also consistent with the fact that the ionizing source is located to the southwest of the core. The region mapped in CO ($J = 2 \rightarrow 1$) shows a similar morphology to the CO ($J = 1 \rightarrow 0$) emission, however the core position is much more intense than the surrounding gas. The $C^{18}O$ ($J = 1 \rightarrow 0$) map shows emission mostly north of the HCO^+ core, with very little north-east extension. This indicates that the large column density molecular gas may not correspond exactly with the star forming core in this source.

The HCO^+ ($J = 1 \rightarrow 0$) integrated intensity map (Figure 3.4) shows a more cometary morphology than the digitized sky survey image in Figure 3.1. The dense gas appears to be preferentially located along a ridge near the southern edge of the cloud. This could be a result of the preexisting density structure of the molecular cloud which was swept up by the ionization front or an effect of the geometry of the expanding HII region. However, these observations can not determine how the gas was swept into that ridge. The HCO^+ ($J = 3 \rightarrow 2$) integrated intensity map only shows significant emission at the position of the star forming core. The HCO^+ ($J = 1 \rightarrow 0$)

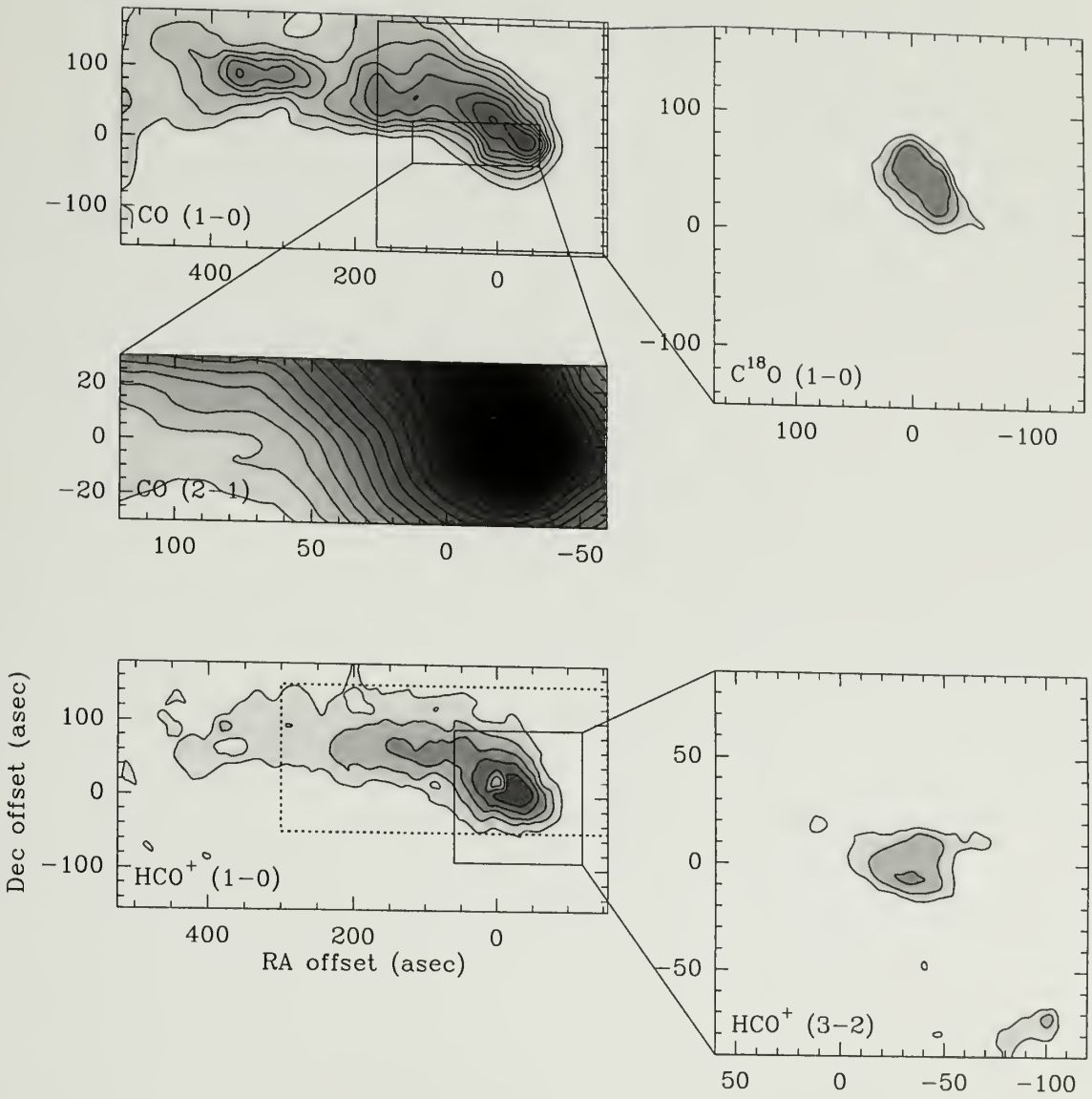

Figure 3.4 Integrated intensity maps of SFO 13. The IRAS source 02570+6028 is located at the center of each map. The CO ($J = 1 \rightarrow 0$) map has a lowest contour of 4.6 K km s^{-1} (3σ) and increments of 4.6 K km s^{-1} (3σ). The CO ($J = 2 \rightarrow 1$) map has a lowest contour of 2.1 K km s^{-1} (3σ) and increments of 5.0 K km s^{-1} (7σ). The $C^{18}O$ ($J = 1 \rightarrow 0$) map has a lowest contour of 0.6 K km s^{-1} (3σ) and increments of 0.2 K km s^{-1} (1σ). The HCO^+ ($J = 1 \rightarrow 0$) map has a lowest contour of 0.4 K km s^{-1} (3σ) and increments of 0.4 K km s^{-1} (3σ). The HCO^+ ($J = 3 \rightarrow 2$) map has a lowest contour of 1.7 K km s^{-1} (3σ) and increments of 0.6 K km s^{-1} (1σ). The dotted rectangle in the HCO^+ ($J = 1 \rightarrow 0$) map indicates the region over which the HCO^+ centroid is shown in Figure 3.5.

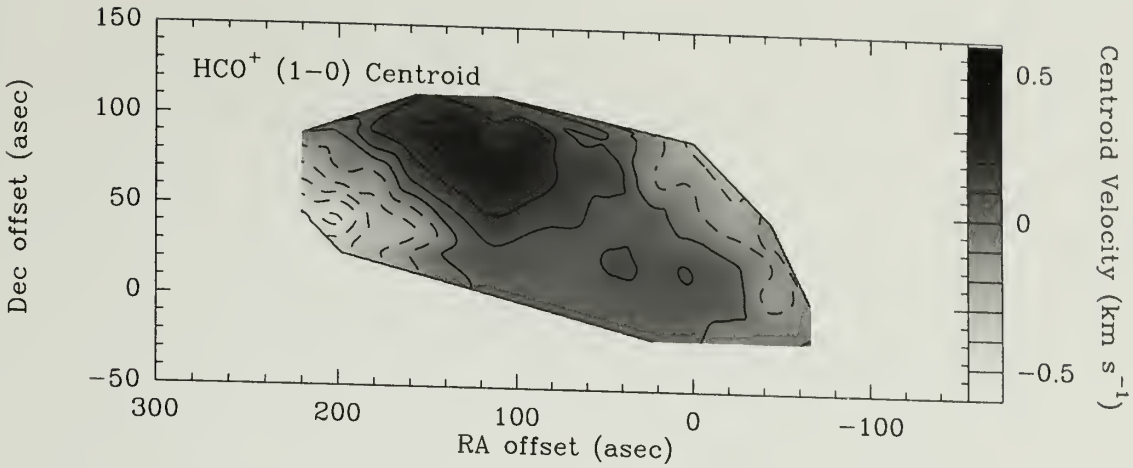

Figure 3.5 The SFO 13 centroid velocity integrated over the line core of HCO^+ ($J = 1 \rightarrow 0$). The line of sight velocity has been subtracted out and the contours and greyscale are indicated on the wedge to the right of the figure.

centroid map (Figure 3.5) does not show a very coherent structure, however there is a significant velocity gradient across the tail in the HCO^+ ($J = 1 \rightarrow 0$) map along the northwest-southeast direction. The CO ($J = 2 \rightarrow 1$) line profiles show distinct wings, which seem to form two lobes of an outflow (Figure 3.6). This outflow has not previously been observed, although SFO found line wings indicative of an outflow in their CO ($J = 2 \rightarrow 1$) observation of this source.

3.3.1.3 SFO 16

SFO 16, also known as L1634 and RNO40, is classified as a type A bright-rimmed cloud by SFO, as it is a broad ionization front, with no tail. SFO 16 borders Barnard's Loop, and is at a distance of 400 pc. The embedded IRAS source 05173–0555 has a spectral energy distribution in the IRAS bands consistent with an embedded YSO (SFO). Cohen (1980) describes this object as a purely nebulous elongated very Red source typical of Herbig-Haro objects. Emission lines which Cohen (1980) detects in this source include Hα, Hβ, Hγ, [NII], [SII], [OI], [NI], [OIII], and HeI.

Figure 3.7a shows the central line profiles towards the IRAS source 05173–0555. The vertical line indicates the best fit velocity of the N_2H^+ ($J = 1 \rightarrow 0$) hyperfine en-

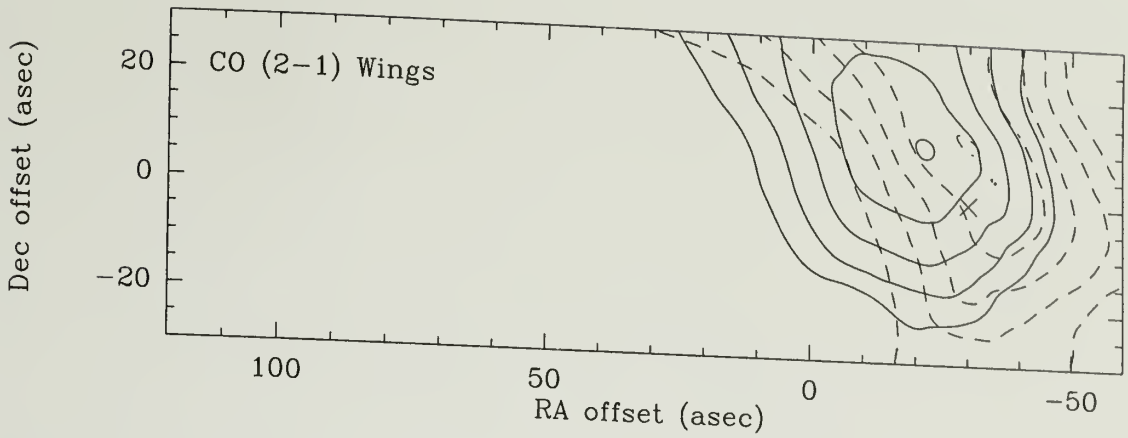

Figure 3.6 The SFO 13 CO ($J = 2 \rightarrow 1$) line wing emission. The blue lobe, indicated by dotted lines, is the integrated intensity in the range of −48 to −39.5 km s^{-1}. The red lobe, indicated by solid lines, is the integrated intensity in the range from −37.5 to −28 km s^{-1}. The lowest contour in each case is the half power contour. The x indicates the HCO^+ ($J = 3 \rightarrow 2$) peak integrated intensity position.

semble. Both the CO ($J = 1 \rightarrow 0$) and the CO ($J = 2 \rightarrow 1$) lines show wings. These wings often indicate the presence of outflows. The $C^{18}O$ ($J = 1 \rightarrow 0$) line, however appears to have a fairly gaussian shape. The HCO^+ line profiles, shown in Figure 3.7a, are a bit more enigmatic. The HCO^+ ($J = 3 \rightarrow 2$) and $H^{13}CO^+$ ($J = 3 \rightarrow 2$) lines seem fairly well centered on the V_{LSR}, but the HCO^+ ($J = 1 \rightarrow 0$) shows a pronounced asymmetry. This asymmetric profile is not shared by the $H^{13}CO^+$ ($J = 1 \rightarrow 0$) line, indicating that the asymmetry observed in the HCO^+ line is probably the result of a radiative transfer effect, and not an effect of the superposition of clouds along the line of sight. Line asymmetries can be produced by infall (Walker et al., 1994), however this produces a line which has greater emission blue-shifted from line center, and our example is red-shifted from line center. It is possible that the HCO^+ ($J = 1 \rightarrow 0$) profile is caused by an outflow. Another possibility is that this red-asymmetric profile is due to infall in a region where the shock heating has inverted the excitation temperature profile of the infalling gas, so that is has a higher excitation temperature far from the core and a lower excitation temperature near the core. This hypothesis will be fully explored in §4.2.

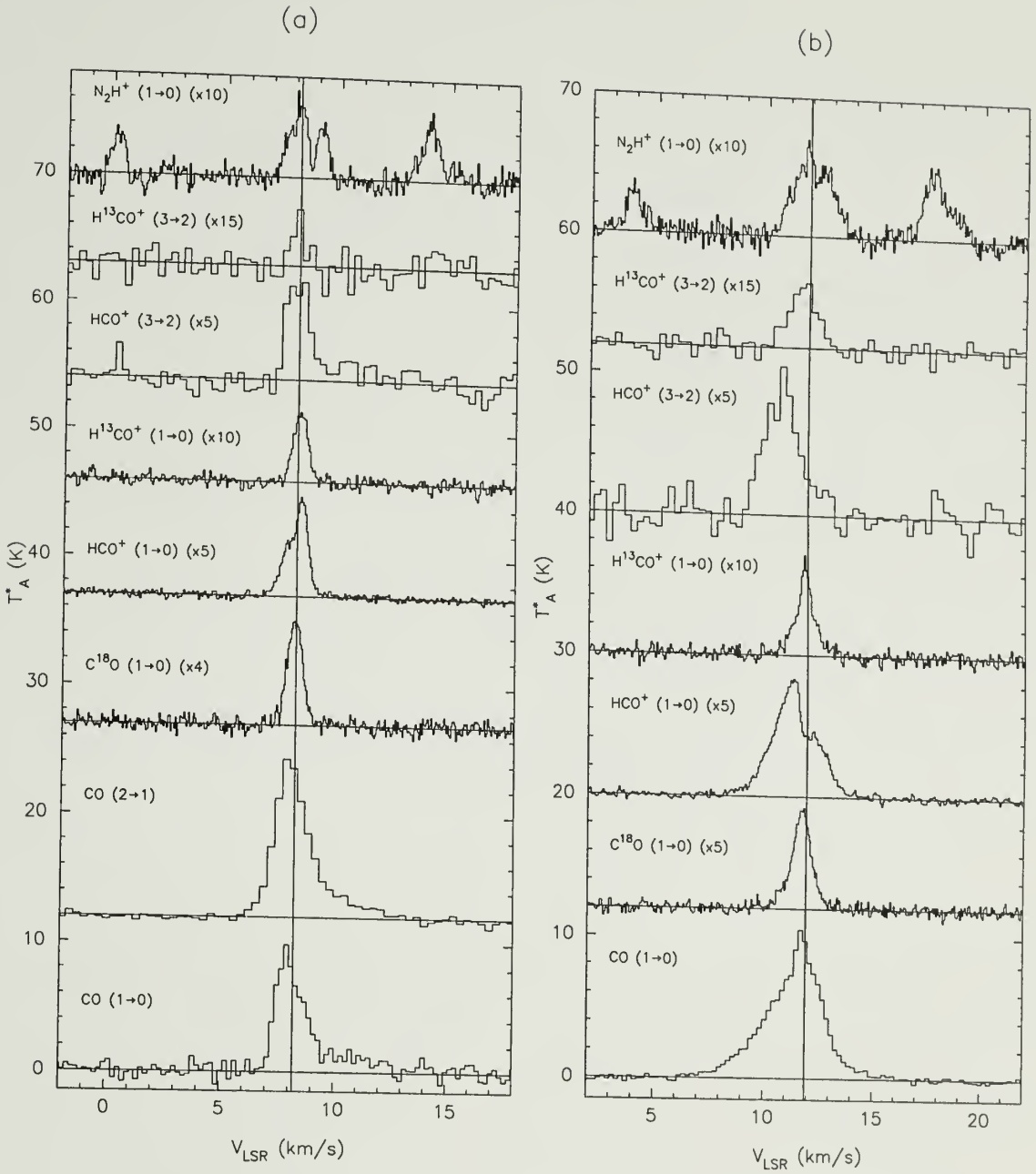

Figure 3.7 Line profiles of molecular transitions in the direction of the central IRAS source of SFO 16 (a) and SFO 18 (b).

The CO and HCO^+ integrated intensity maps are shown in Figure 3.8. Although classified as a type A cloud by SFO, the CO ($J = 1 \rightarrow 0$) seems to show a well defined tail moving off to the south-west, however the ionization source is located directly to the east of the core. The $C^{18}O$ ($J = 1 \rightarrow 0$) integrated intensity map (Figure 3.8) shows the molecular core surrounding the IRAS source, and no evidence of the outflow lobes. It does appear that there is a tail traced by the $C^{18}O$ elongated to the west of the core. The HCO^+ ($J = 1 \rightarrow 0$) integrated intensity image in Figure 3.8 is more indicative of a type A morphology that the CO integrated intensity maps. The majority of the gas traced by the HCO^+ emission is in a fairly broad regions which is densest around the IRAS core, but shows another possible core 300″ north of the IRAS core. The HCO^+ ($J = 3 \rightarrow 2$) integrated intensity map highlights the location of the core. Figure 3.9 shows the centroid velocity of the HCO^+ ($J = 1 \rightarrow 0$) emission in the dense regions of the source. This centroid was calculated over the line core velocities, and do not include contributions from line wings if they are present. On average there appears to be a north-south velocity gradient which could indicate rotation of the cloud.

In both the CO ($J = 1 \rightarrow 0$) and CO ($J = 2 \rightarrow 1$) integrated intensity maps, lobes indicative of a bipolar outflow are evident. Figure 3.10 shows an integrated intensity map of the CO ($J = 2 \rightarrow 1$) line wings. This figure shows that there is an outflow, with the blue shifted lobe on the west side of the core and the red shifted lobe to the east of the core. Previous studies by Hodapp & Ladd (1995) and Fukui (1989) indicate the presence of this outflow and a second outflow, which we do not detect, aligned in the northwest-southeast direction. The axis of rotation, derived from the HCO^+ centroid map, is aligned east-west, matching the alignment of outflow we detect. This alignment is predicted by current star formation theories that posit that outflows are located along the polar direction of a rotating protostar, in order to shed some angular momentum before material can fall into the protostar.

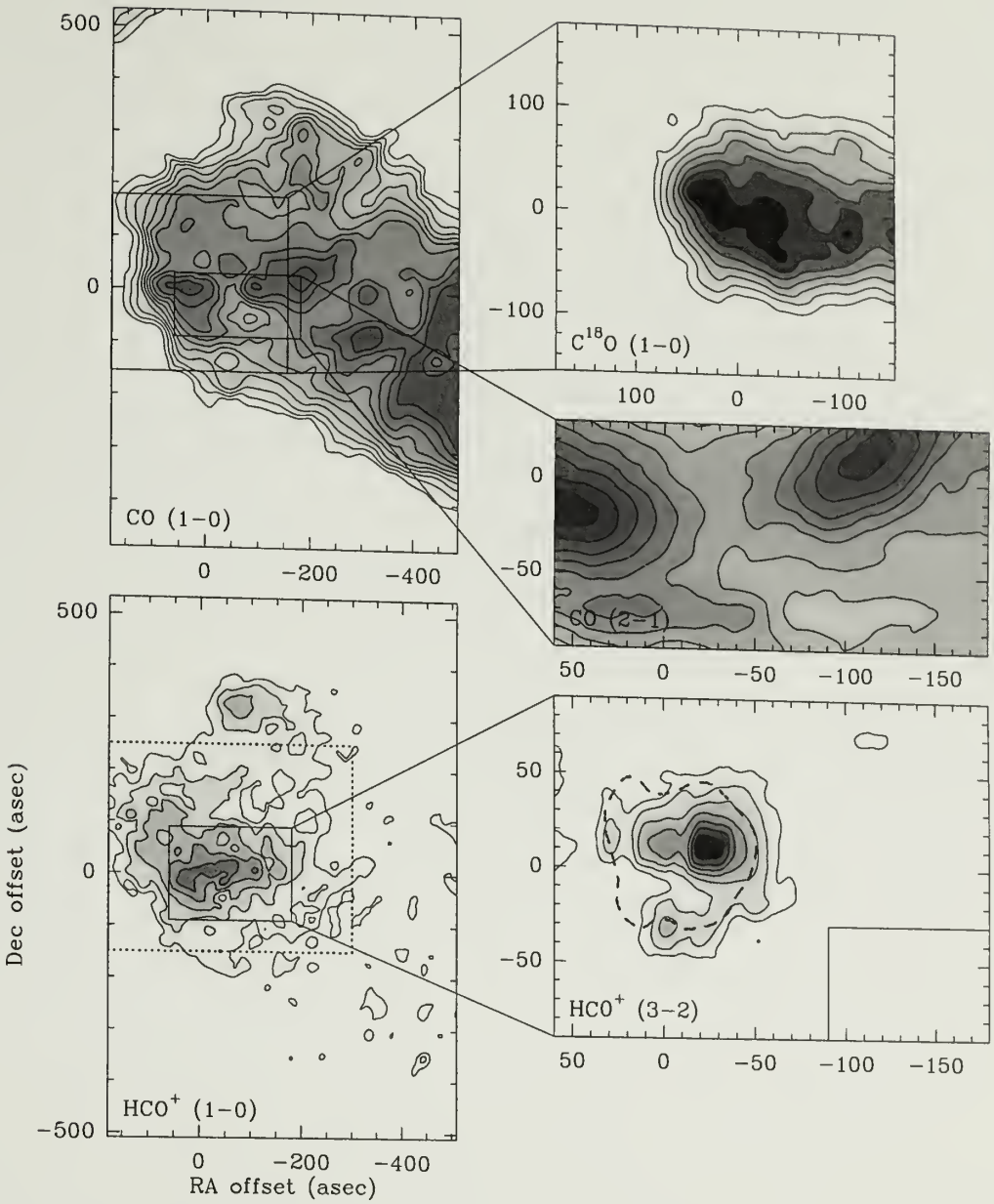

Figure 3.8 Integrated intensity maps of SFO 16. The IRAS source 05173–0555 is located at the center of each map. The CO ($J = 1 \rightarrow 0$) map has a lowest contour of 4.3 K km s^{-1} (3σ) and increments of 1.4 K km s^{-1} (1σ). The CO ($J = 2 \rightarrow 1$) map has a lowest contour of 6.0 K km s^{-1} (12σ) and increments of 2.5 K km s^{-1} (5σ). The $C^{18}O$ ($J = 1 \rightarrow 0$) map has a lowest contour of 0.6 K km s^{-1} (3σ) and increments of 0.2 K km s^{-1} (1σ). The HCO^+ ($J = 1 \rightarrow 0$) map has a lowest contour of 0.4 K km s^{-1} (3σ) and increments of 0.3 K km s^{-1} (2σ). The HCO^+ ($J = 3 \rightarrow 2$) map has a lowest contour of 0.9 K km s^{-1} (3σ) and increments of 0.3 K km s^{-1} (1σ). The dotted rectangle in the HCO^+ ($J = 1 \rightarrow 0$) map indicates the region over which the HCO^+ centroid is shown in figure 3.9. The dashed contour in the HCO^+ ($J = 3 \rightarrow 2$) indicates the half power contour of the N_2H^+ ($J = 1 \rightarrow 0$) emission.

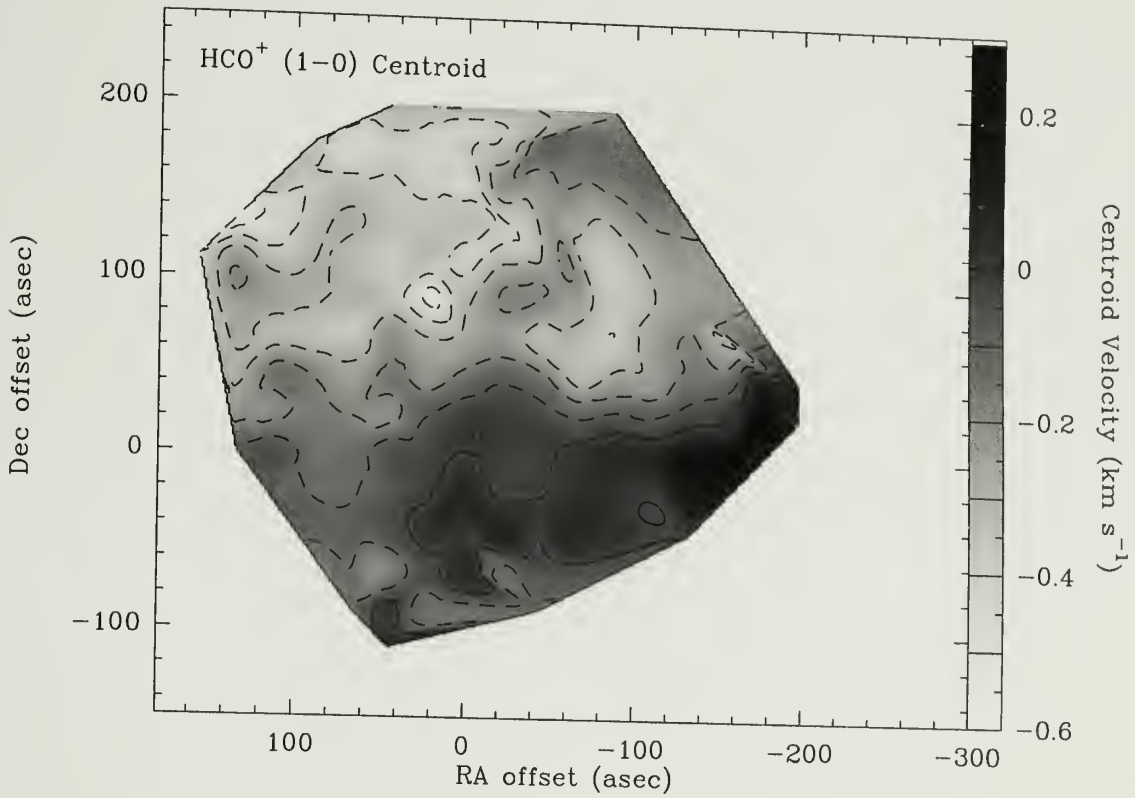

Figure 3.9 The SFO 16 centroid velocity integrated over the line core of HCO^+ ($J = 1 \rightarrow 0$). The line of sight velocity has been subtracted out and the contours and greyscale are indicated on the wedge to the right of the figure.

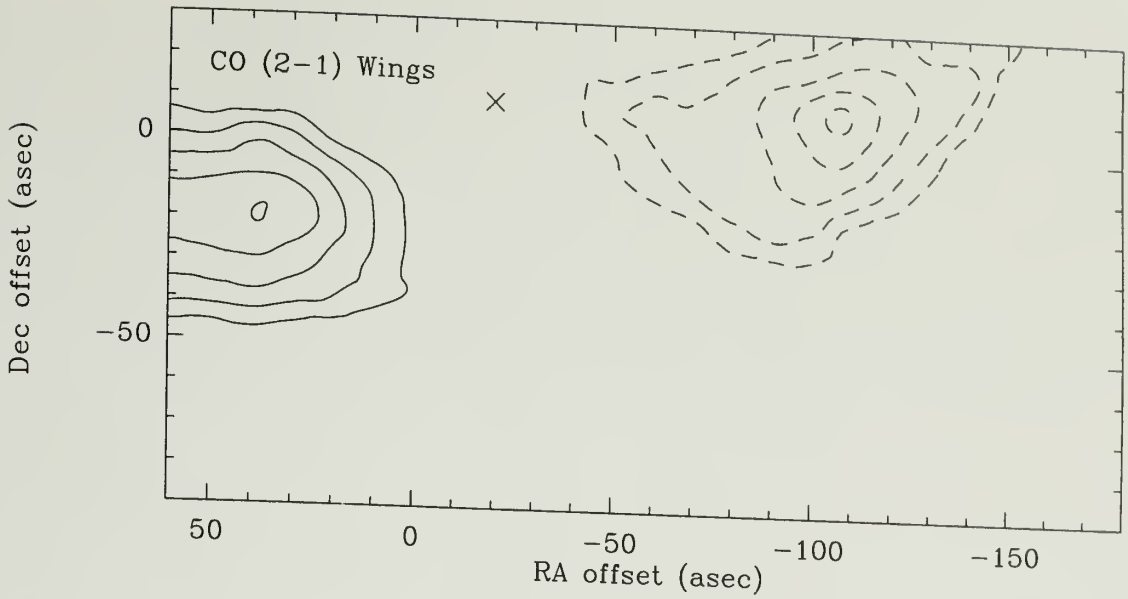

Figure 3.10 The SFO 16 CO ($J = 2 \rightarrow 1$) line wing emission. The blue lobe, indicated by dotted lines, is the integrated intensity in the range of –2 to 7.2 km s^{-1}. The red lobe, indicated by solid lines, is the integrated intensity in the range from 9 to 18 km s^{-1}. The lowest contour in each case is the half power contour. The x indicates the HCO^+ ($J = 3 \rightarrow 2$) peak integrated intensity position.

3.3.1.4 SFO 18

SFO 18, also known as B35A, is also a type A bright-rimmed cloud (SFO). It borders the HII region λ Ori at a distance of about 400 pc. The embedded IRAS source 05417+0907 has a spectral energy distribution consistent with an embedded YSO (SFO). Myers et al. (1988) have detected an outflow in CO ($J = 1 \rightarrow 0$) which extends in the northwest-southeast direction around the embedded IRAS source.

Our line profiles shown in Figure 3.7b show bright, extensive wings on the CO ($J = 1 \rightarrow 0$) line, when compared to its $C^{18}O$ counterpart. The HCO^+ ($J = 1 \rightarrow 0$) and HCO^+ ($J = 3 \rightarrow 2$) line profiles both show a significant blue asymmetry when compared to their $H^{13}CO^+$ isotopic counterparts. This may indicate that the gas is infalling around the core or cores (Walker et al., 1994).

The CO $J = 1 \rightarrow 0$ integrated intensity map (Figure 3.11) shows the broad ionization front with a core at its apex, typical of type A sources. The CO emission cuts off fairly abruptly on the western edge of the cloud, where the ionization front is located.

The ionizing source is located directly to the west of the core. Besides the increased emission at the core, one can see a general increase in CO ($J = 1 \rightarrow 0$) emission adjacent to the ionization front which is probably due to an increase in column density as gas gets swept up by the ionization front, a factor which ultimately enhances the density and leads to self-gravitating clumps (Elmegreen, 1992). The $C^{18}O$ ($J = 1 \rightarrow 0$) better traces the high column density gas around the core and shows what may be another core to the northeast of the first. The HCO^+ ($J = 1 \rightarrow 0$) emission better traces the dense ridge, as seen in the integrated intensity map in Figure 3.11, and the core in which the IRAS source is embedded. This ridge of dense gas is consistent with the type A morphological classification by SFO. Higher resolution HCO^+ ($J = 3 \rightarrow 2$) observations of the core show several emission peaks, indicating that there may be several low mass stars forming simultaneously in that region. This is consistent with models of shock driven collapse (Vanhala & Cameron, 1998) in which multiple stars can be formed.

Further evidence supporting a region of infall is seen in Figure 3.12 where we see that the entire core region has blue shifted HCO^+ ($J = 1 \rightarrow 0$) centroid velocities relative to the rest of the cloud where emission is strong enough to accurately measure a centroid. This match between the core emission and the region of possible infall is further evidence of a collapsing, star forming, core (Narayanan et al., 2002). Figure 3.13 shows the integrated intensity map of the CO ($J = 1 \rightarrow 0$) line wings, and we see the outflow in the same direction as detected by Myers et al. (1988).

3.3.1.5 SFO 20

SFO 20 is a type C bright-rimmed cloud. The long tail is visible in the optical image (Figure 3.1) pointing northwards, away from the HII region IC434, which is approximately 400 parsecs from us (SFO). The infrared spectral energy distribution of this source is consistent with an embedded YSO (SFO). Sugitani et al. (1989)

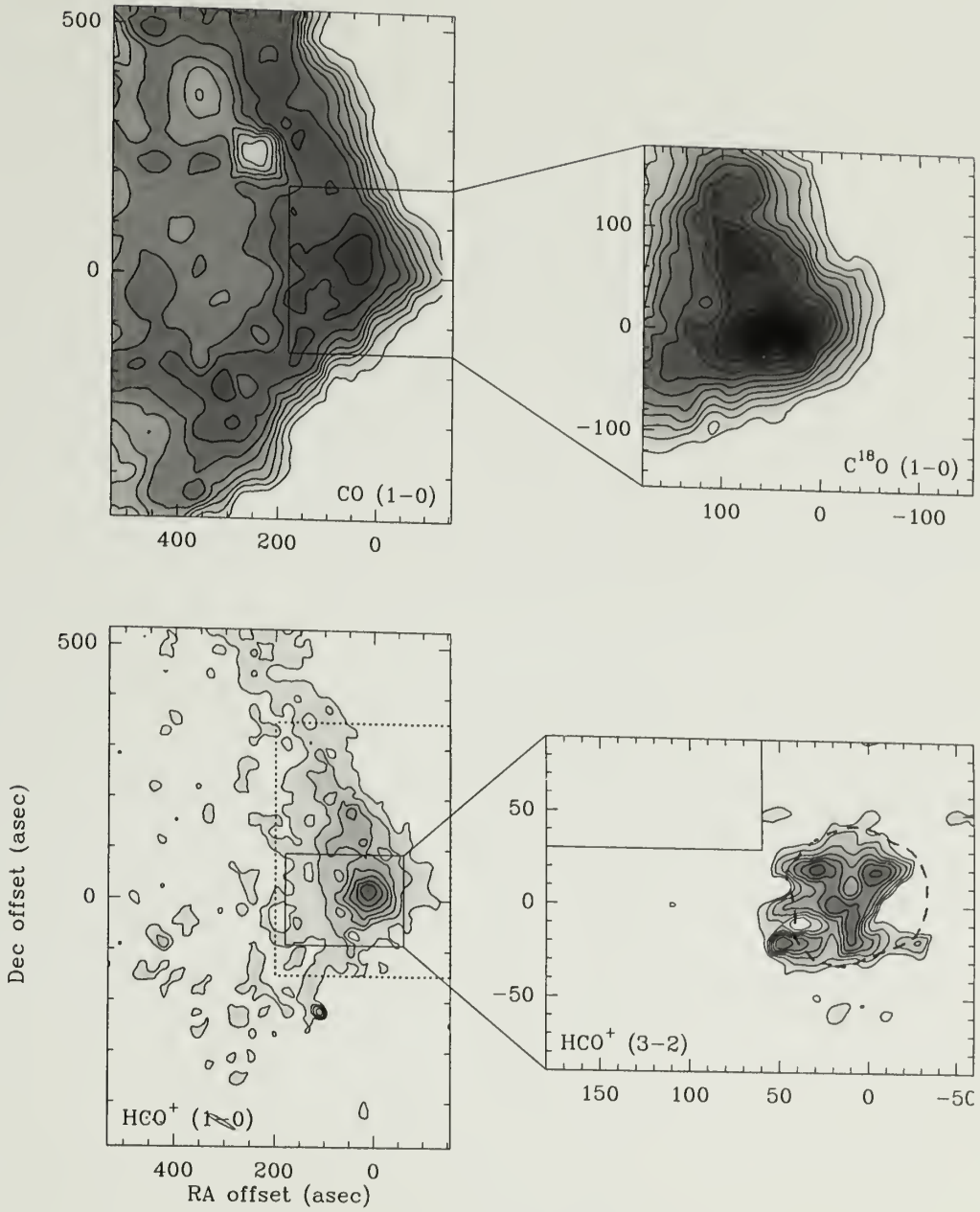

Figure 3.11 Integrated intensity maps of SFO 18. The IRAS source 05417+0907 is located at the center of each map. The CO ($J = 1 \rightarrow 0$) map has a lowest contour of 1.8 K km s^{-1} (3σ) and increments of 1.8 K km s^{-1} (3σ). The $C^{18}O$ ($J = 1 \rightarrow 0$) map has a lowest contour of 0.4 K km s^{-1} (3σ) and increments of 0.1 K km s^{-1} (1σ). The HCO^+ ($J = 1 \rightarrow 0$) map has a lowest contour of 0.7 K km s^{-1} (3σ) and increments of 0.5 K km s^{-1} (2σ). The HCO^+ ($J = 3 \rightarrow 2$) map has a lowest contour of 1.6 K km s^{-1} (3σ) and increments of 0.5 K km s^{-1} (1σ). The dotted rectangle in the HCO^+ ($J = 1 \rightarrow 0$) map indicates the region over which the HCO^+ centroid is shown in figure 3.12. The dashed contour in the HCO^+ ($J = 3 \rightarrow 2$) indicates the half power contour of the N_2H^+ ($J = 1 \rightarrow 0$) emission.

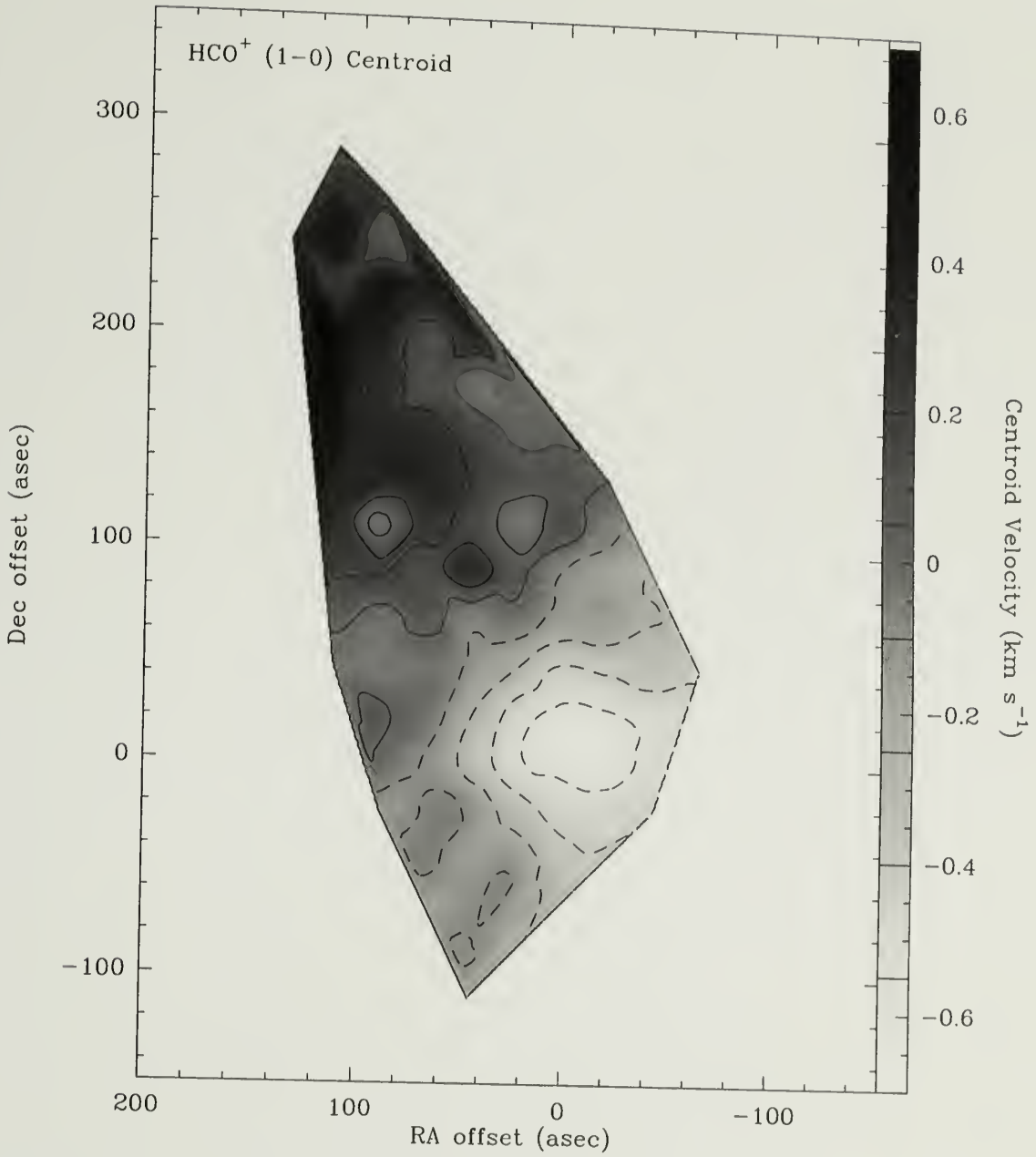

Figure 3.12 The SFO 18 centroid velocity integrated over the line core of HCO^+ ($J = 1 \rightarrow 0$). The line of sight velocity has been subtracted out and the contours and greyscale are indicated on the wedge to the right of the figure.

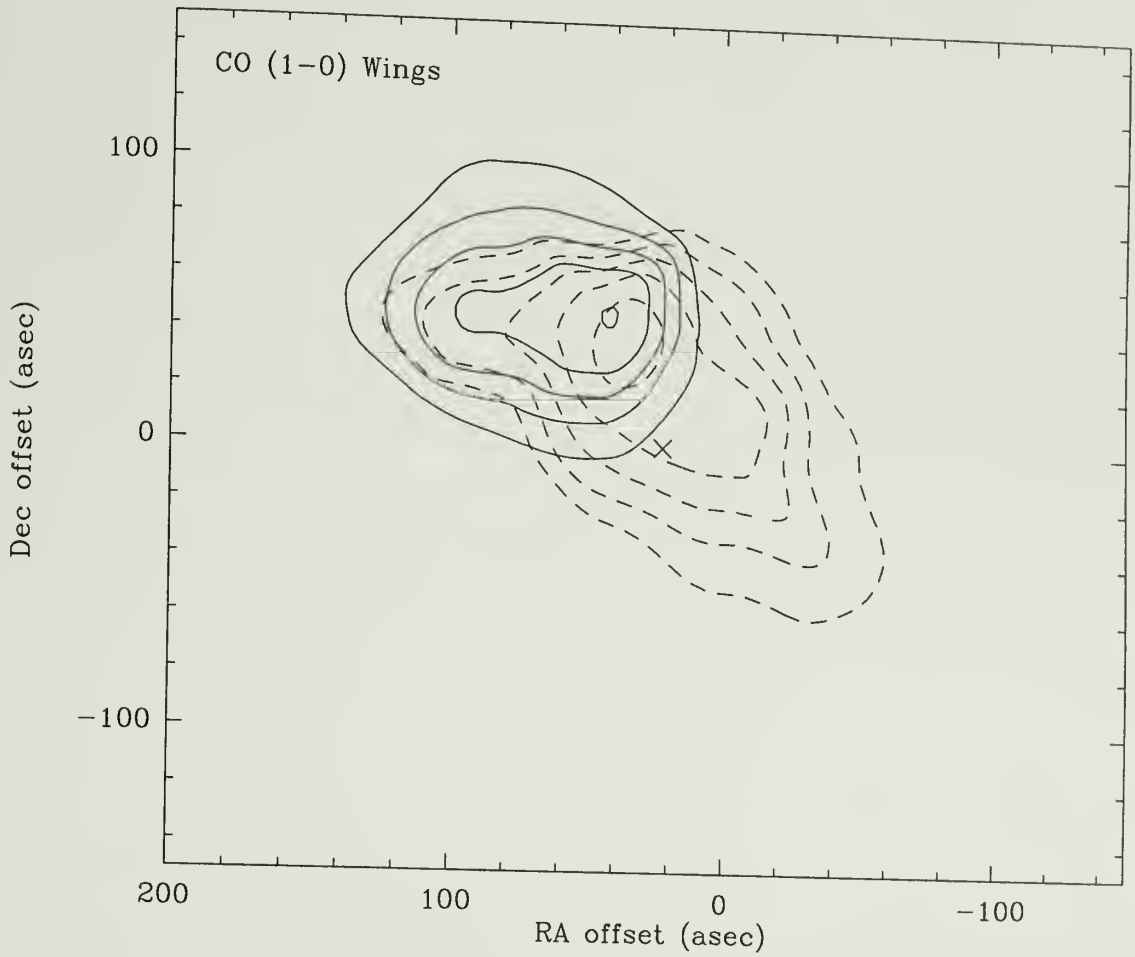

Figure 3.13 The SFO 18 CO ($J = 1 \rightarrow 0$) line wing emission. The blue lobe, indicated by dotted lines, is the integrated intensity in the range of 2 to 11 km s^{-1}. The red lobe, indicated by solid lines, is the integrated intensity in the range from 13 to 22 km s^{-1}. The lowest contour in each case is the half power contour. The x indicates the $C^{18}O$ ($J = 1 \rightarrow 0$) peak integrated intensity position.

discovered and mapped an outflow around the embedded IRAS source in SFO 20 using the NRO 45m telescope in the CO ($J = 1 \rightarrow 0$) transition.

The CO ($J = 1 \rightarrow 0$) and CO ($J = 2 \rightarrow 1$) line profiles shown in Figure 3.14a show a blue asymmetry and wings on the $J = 2 \rightarrow 1$ transition. The HCO^+ line profiles are all fairly gaussian, and fairly well centered on the N_2H^+ ($J = 1 \rightarrow 0$) V_{LSR}. There is no clear evidence of infall from the HCO^+ transitions.

The CO ($J = 1 \rightarrow 0$) integrated intensity map (Figure 3.15) shows the type C morphology, with a strong core and evidence of a tail trailing off to the north. The CO ($J = 2 \rightarrow 1$) emission also traces the core, though the emission peak does not match the HCO^+ ($J = 3 \rightarrow 2$) core position exactly. The $C^{18}O$ ($J = 1 \rightarrow 0$) emission is also peaked on the core and relatively absent in the tail. The HCO^+ ($J = 1 \rightarrow 0$) emission is mainly centered on the core with some emission tracing the tail. While many of the previous sources had substantial emission outside of the core region, this one does not. Under the assumption that the type C morphology is the most temporally evolved morphology, the ionization front may have long since passed this region and it is surrounded by ionized gas. As the core gas collapses the tail can be eaten away as it becomes less and less shielded. The HCO^+ ($J = 3 \rightarrow 2$) traces only the core material.

Analysis of the HCO^+ ($J = 1 \rightarrow 0$) centroid velocity, shown in Figure 3.16 indicates a small, but statistically significant gradient across the core. This gradient may indicate the cloud's rotation. As an outflow has already been detected in this source by Sugitani et al. (1989) we chose to look at the CO ($J = 2 \rightarrow 1$) wing integrated intensity in order to try to verify the existing observation. Figure 3.17 shows that the line wings do show two lobes of emission, with the red lobe being predominantly northeast of the core and the blue lobe predominantly southwest of the core, similar to previous results. The cloud rotation shown in Figure 3.16 is perpendicular to the outflow, which is a prediction of current theories of star formation.

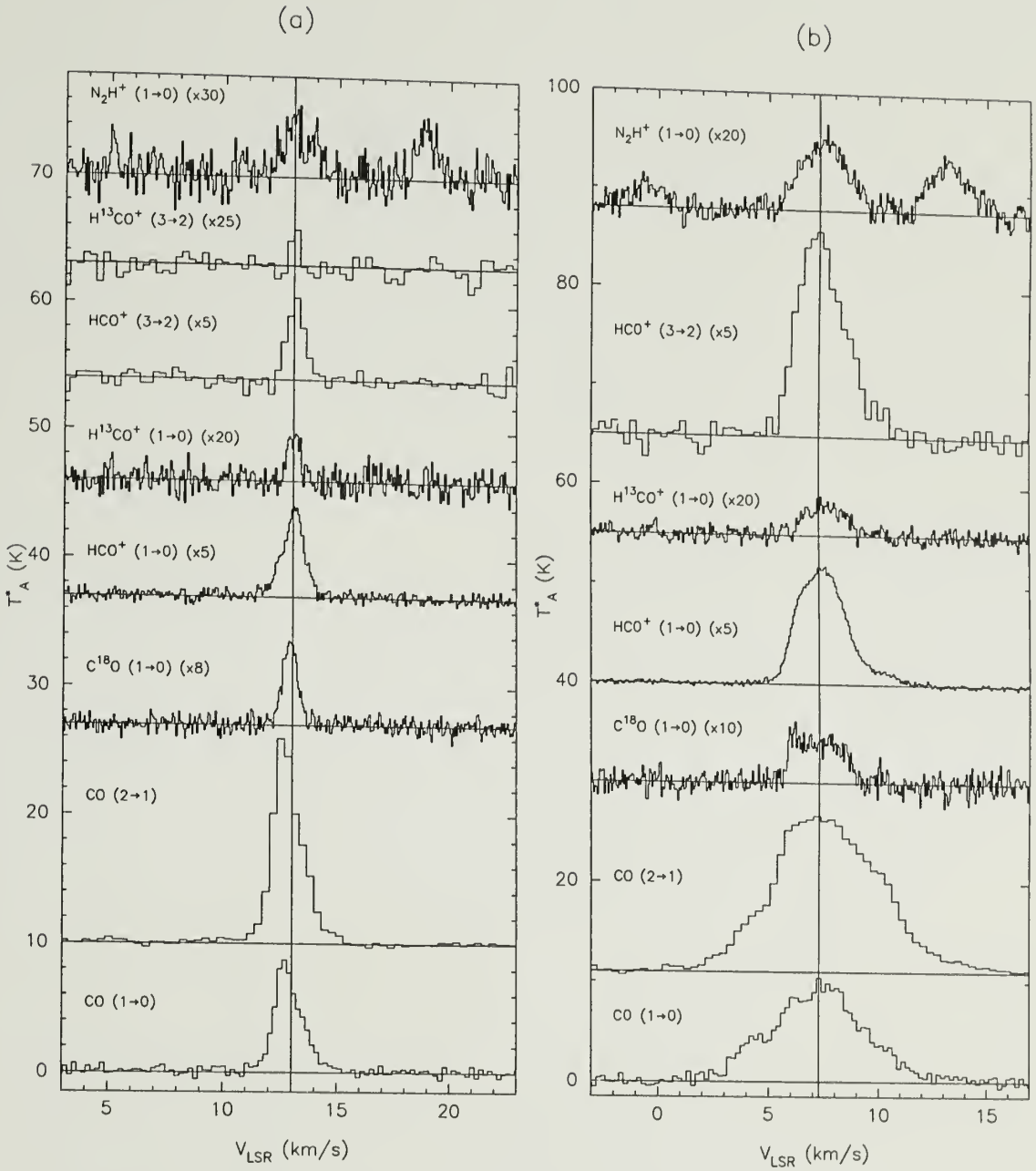

Figure 3.14 Line profiles of molecular transitions in the direction of the central IRAS source of SFO 20 (a) and SFO 25 (b).

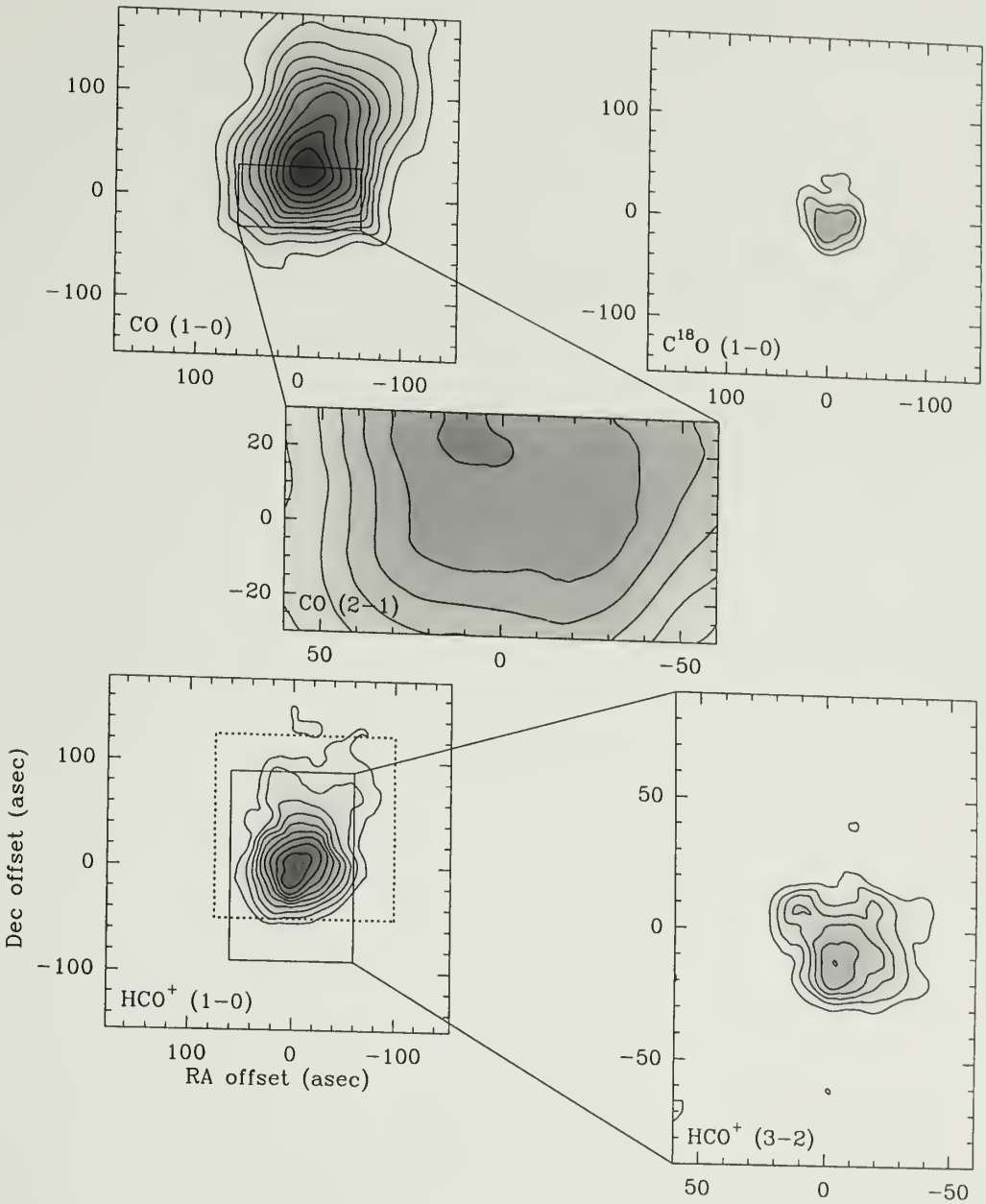

Figure 3.15 Integrated intensity maps of SFO 20. The IRAS source 05173-0555 is located at the center of each map. The CO ($J = 1 \rightarrow 0$) map has a lowest contour of 1.1 K km s^{-1} (3σ) and increments of 1.1 K km s^{-1} (3σ). The CO ($J = 2 \rightarrow 1$) map has a lowest contour of 1.0 K km s^{-1} (3σ) and increments of 3.4 K km s^{-1} (10σ). The C^{18}O ($J = 1 \rightarrow 0$) map has a lowest contour of 0.4 K km s^{-1} (3σ) and increments of 0.1 K km s^{-1} (1σ). The HCO$^+$ ($J = 1 \rightarrow 0$) map has a lowest contour of 0.4 K km s^{-1} (3σ) and increments of 0.1 K km s^{-1} (1σ). The HCO$^+$ ($J = 3 \rightarrow 2$) map has a lowest contour of 0.6 K km s^{-1} (3σ) and increments of 0.2 K km s^{-1} (1σ). The dotted rectangle in the HCO$^+$ ($J = 1 \rightarrow 0$) map indicates the region over which the HCO$^+$ centroid is shown in figure 3.16.

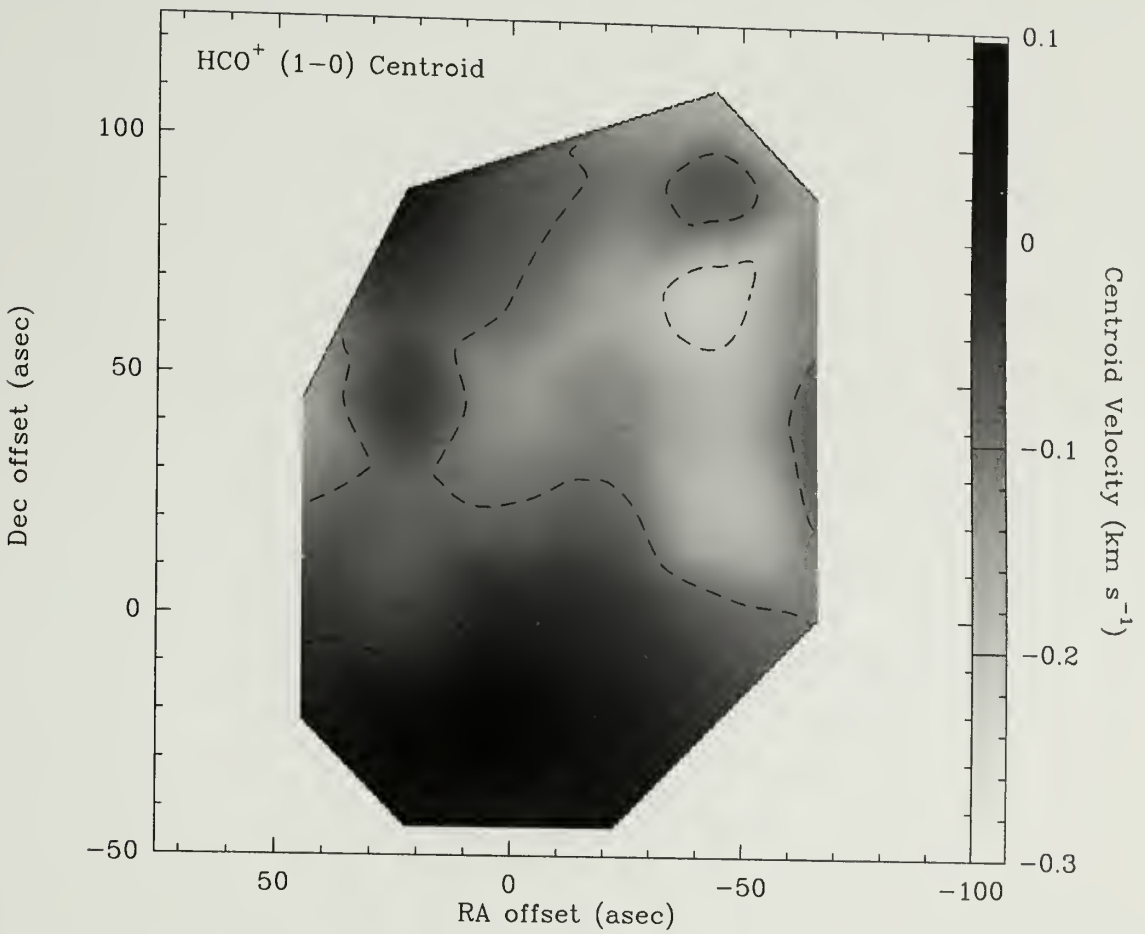

Figure 3.16 The SFO 20 centroid velocity integrated over the line core of HCO^+ ($J = 1 \rightarrow 0$). The line of sight velocity has been subtracted out and the contours and greyscale are indicated on the wedge to the right of the figure.

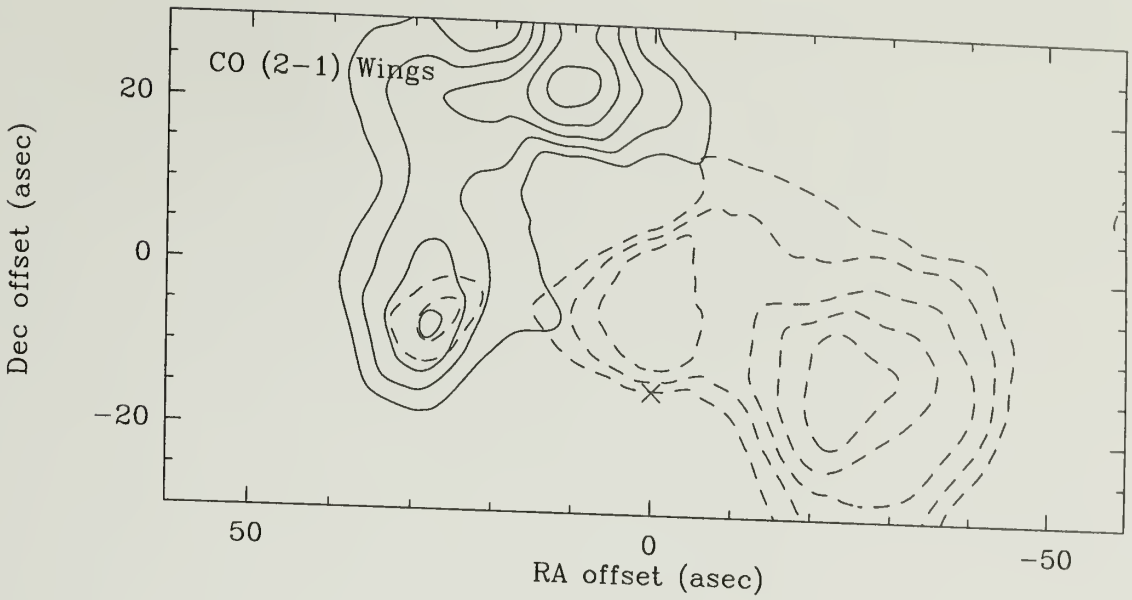

Figure 3.17 The SFO 20 CO ($J = 2 \rightarrow 1$) line wing emission. The blue lobe, indicated by dotted lines, is the integrated intensity in the range of 3 to 12 km s^{-1}. The red lobe, indicated by solid lines, is the integrated intensity in the range from 14 to 23 km s^{-1}. The lowest contour in each case is the half power contour. The x indicates the HCO^+ ($J = 3 \rightarrow 2$) peak integrated intensity position.

3.3.1.6 SFO 25

SFO 25, also known as HH124 (Walsh et al., 1992), is a type B cloud located at a distance of 780 pc. Embedded within is the IRAS source 06382+1017, whose spectral energy distribution is consistent with an embedded YSO (SFO). SFO 25 is associated with the HII region NGC 2264. Figure 3.1 shows a moderately curved rim arching northwards away from the ionizing source. However, although there is no tail visible in the optical, there is also no point at which the structure begins to broaden away from the ionizing source as there is for the other type B sources, SFO 4 and SFO 13. As we shall see below, this source bears many similarities with type C cometary clouds as well.

The CO ($J = 1 \rightarrow 0$) and CO ($J = 2 \rightarrow 1$) profiles show a wide (5 km s^{-1}), slightly asymmetric line (Figure 3.14b). The CO ($J = 2 \rightarrow 1$) profile shows line wings, which may indicate the presence of an outflow. The HCO^+ line profiles show some asymmetry as well, mostly in the form of a redshifted tail.

The CO ($J = 1 \rightarrow 0$) integrated intensity map (Figure 3.18) shows a low level of CO emission throughout the region, which may be the result of contamination from nearby diffuse clouds which lie at nearly the same velocity of SFO 25. The $C^{18}O$ ($J = 1 \rightarrow 0$) traces the higher column density gas which forms the SFO 25 core and shows a molecular gas tail to the north. This morphology is more typical of a type C cometary cloud than a type B source. The CO ($J = 2 \rightarrow 1$) emission peaks strongly at the IRAS source position. The HCO^+ ($J = 1 \rightarrow 0$) integrated intensity map (Figure 3.18) shows strongly peaked emission around the core with much weaker emission along the tail to the north of the source, which looks more typical of a type C source than a type B source. The HCO^+ ($J = 3 \rightarrow 2$) emission is also strongly peaked at the IRAS source position.

We detected no coherent velocity structure in the HCO^+ ($J = 1 \rightarrow 0$) velocity centroid observations. However the CO ($J = 2 \rightarrow 1$) line wings show evidence of an outflow oriented in the north-south direction (Figure 3.19), though unrelated emission near the same velocity makes it hard to separate the outflow emission from emission due to other sources.

3.3.1.7 SFO 37

SFO 37, also known as GN 21.38.9, is a type C cloud (SFO). It's cometary structure is quite striking in the optical (Figure 3.1). SFO 37 is associated with the HII region IC1396 located at a distance of 750 pc. Embedded within is the IRAS source 21388+5622 whose spectral energy distribution is consistent with an embedded YSO. An investigation of this region by Duvert et al. (1990) revealed Hα and [SII] emission on the northeast side of the molecular emission core. This emission is consistent with an ionization front driven by the strong UV field of a neighboring O6 star.

The CO ($J = 1 \rightarrow 0$) and CO ($J = 2 \rightarrow 1$) line profiles (Figure 3.20a) shows a fairly gaussian shape centered at a line of sight velocity of approximately 1 km s^{-1}.

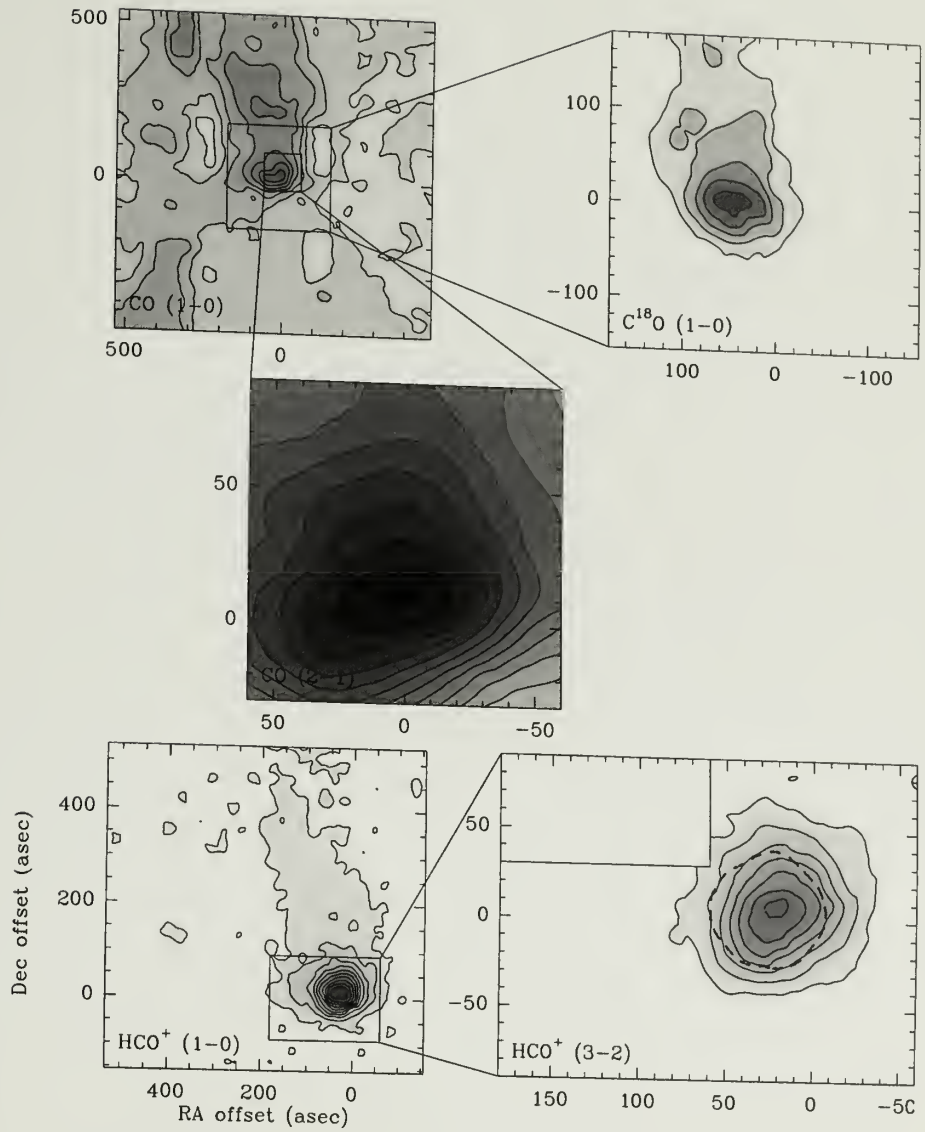

Figure 3.18 Integrated intensity maps of SFO 25. The IRAS source 06382+1017 is located at the center of each map. The CO ($J = 1 \rightarrow 0$) map has a lowest contour of 3.6 K km s^{-1} (3σ) and increments of 6.1 K km s^{-1} (5σ). The CO ($J = 2 \rightarrow 1$) map has a lowest contour of 1.7 K km s^{-1} (3σ) and increments of 5.6 K km s^{-1} (10σ). The C^{18}O ($J = 1 \rightarrow 0$) map has a lowest contour of 0.5 K km s^{-1} (3σ) and increments of 0.4 K km s^{-1} (2σ). The HCO$^+$ ($J = 1 \rightarrow 0$) map has a lowest contour of 0.5 K km s^{-1} (3σ) and increments of 0.8 K km s^{-1} (5σ). The HCO$^+$ ($J = 3 \rightarrow 2$) map has a lowest contour of 1.2 K km s^{-1} (3σ) and increments of 2.0 K km s^{-1} (5σ). The dashed contour in the HCO$^+$ ($J = 3 \rightarrow 2$) indicates the half power contour of the N_2H^+ ($J = 1 \rightarrow 0$) emission.

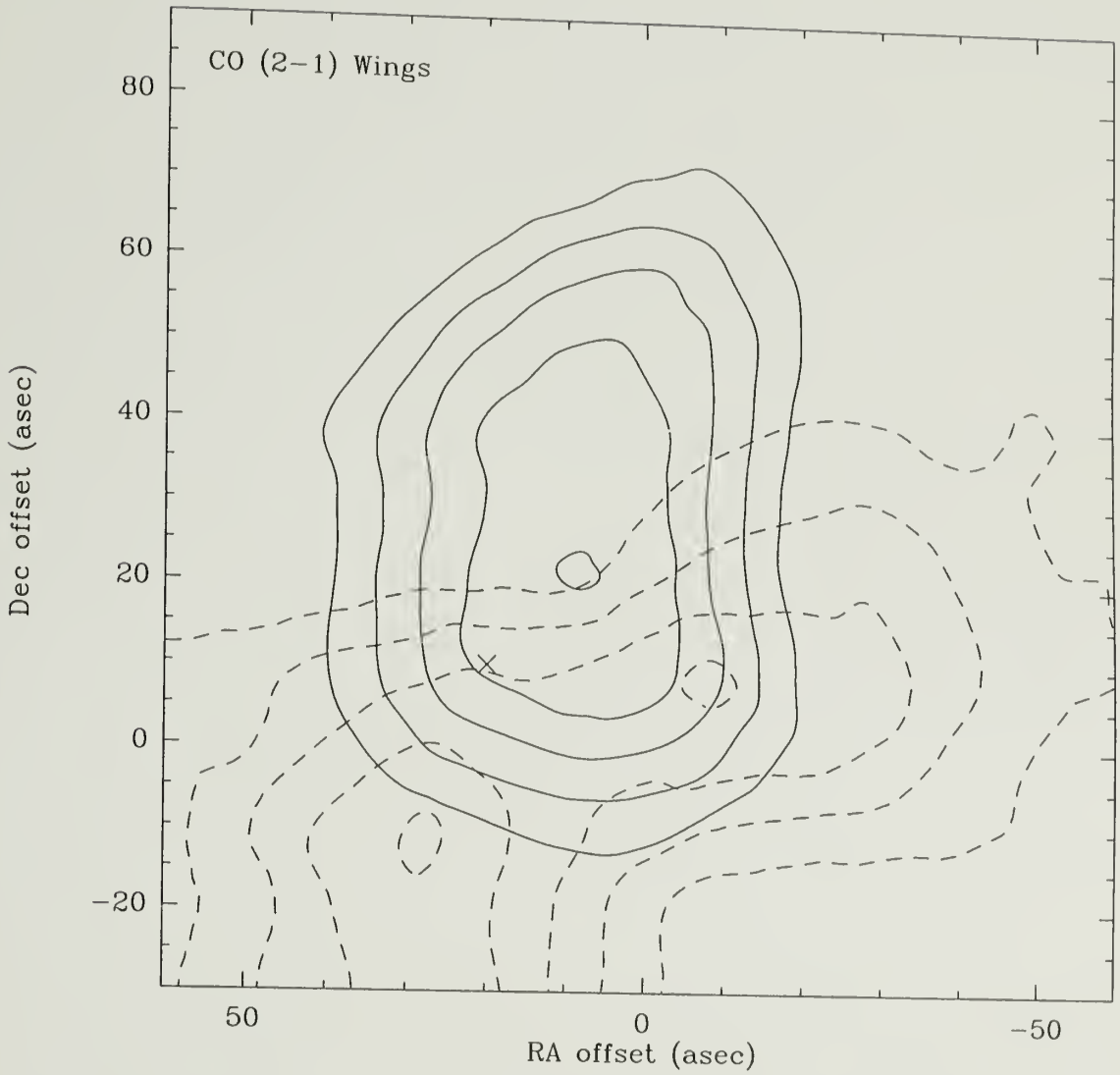

Figure 3.19 The SFO 25 CO ($J = 2 \rightarrow 1$) line wing emission. The blue lobe, indicated by dotted lines, is the integrated intensity in the range of −2 to −5.5 km s^{-1}. The red lobe, indicated by solid lines, is the integrated intensity in the range from 9 to 18 km s^{-1}. The lowest contour in each case is the half power contour. The x indicates the HCO^+ ($J = 3 \rightarrow 2$) peak integrated intensity position.

A second component is visible at a line of sight velocity of approximately 7 km s^{-1}. Duvert et al. (1990) speculate that this second component may be a remnant of the low density gas shell in which the core formed, however we find this to be unlikely; the second component's spatial distribution appears unrelated to that of the main component, and the low density gas surrounding the SFO 37 core has most likely been ionized. Both the HCO^+ and $H^{13}CO^+$ profiles in Figure 3.20a appear fairly gaussian and share approximately the same centroid velocity. As is the case for many of these bright-rimmed clouds, there is little or no indication of infall, despite the presence of a previously detected outflow (Duvert et al., 1990).

The integrated intensity map of the CO ($J = 1 \rightarrow 0$) emission shows the cometary cloud structure stretching from the center of the plot down to the southwest. There also appears to be a spur of gas 120″ south of the core extending west out of the tail of the cometary cloud (Figure 3.21). The CO ($J = 2 \rightarrow 1$) integrated intensity map also shows a cometary structure running northwest-southeast. Although we detected no outflow, the higher resolution survey of Duvert et al. (1990) detected a bipolar outflow with a 20″ separation between the red and blue lobes and a north-south orientation.

The HCO^+ ($J = 1 \rightarrow 0$) integrated intensity map (Figure 3.21) shows emission from the IRAS core, as well as an extension to the southeast. There is a centroid velocity gradient of the HCO^+ ($J = 1 \rightarrow 0$) emission along the length of the cometary cloud (Figure 3.22). This velocity gradient may be due to the interaction of the ionization front and the cometary cloud. Recent near-infrared observations of this source have also shown several point sources which may be pre-main-sequence stars which lie on a line extending from the embedded IRAS source in the opposite direction as the tail (Sugitani et al., 1995, 1999). These young stars, and their extremely regular arrangement along the line which bisects the ionization front, which would be the line along which the dense core would travel in a radiation driven cometary globule (Lefloch & Lazareff, 1994), make this source an excellent candidate for small scale sequential

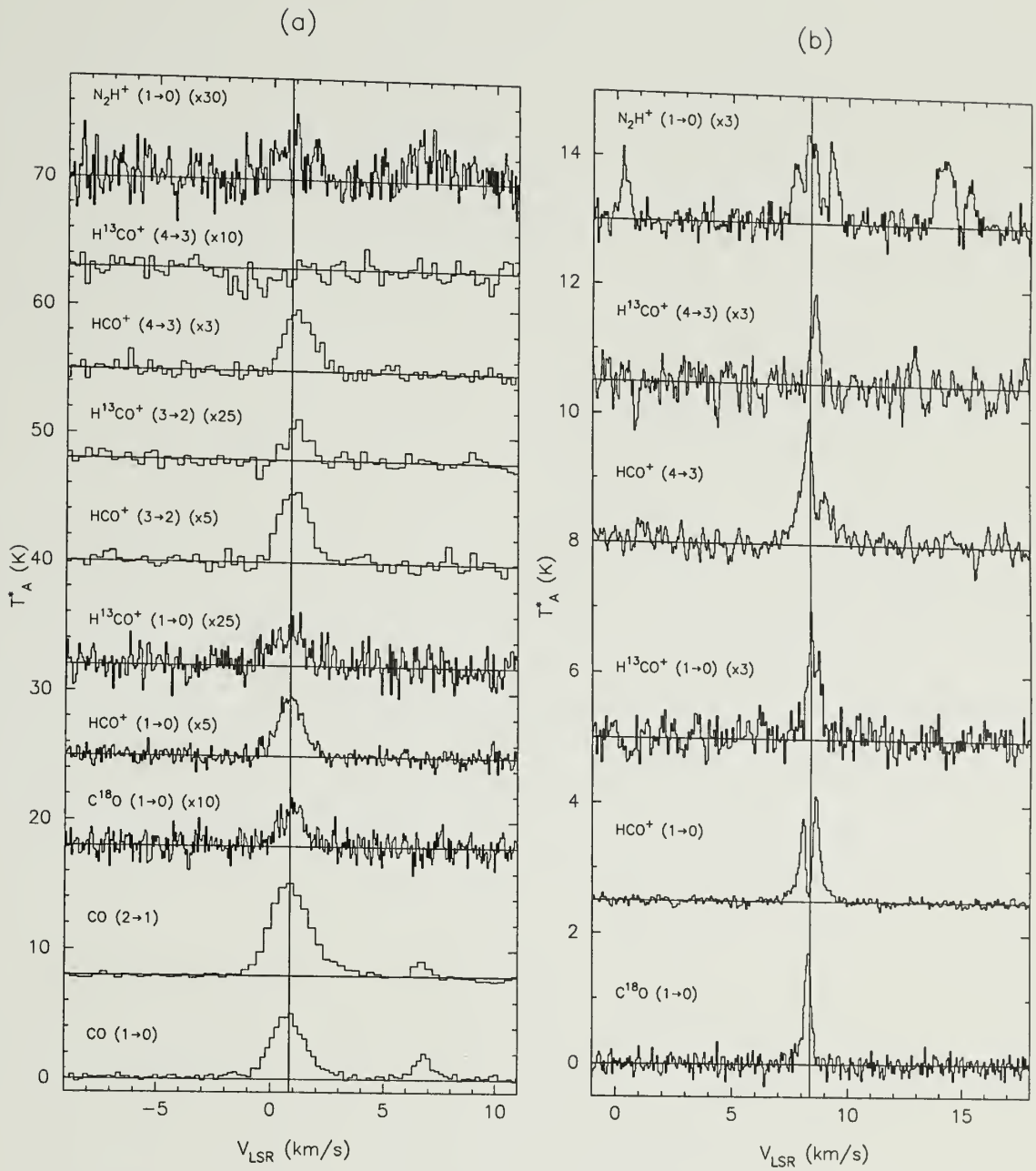

Figure 3.20 Line profiles of molecular transitions in the direction of the central IRAS source of SFO 37 (a) and B 335 (b).

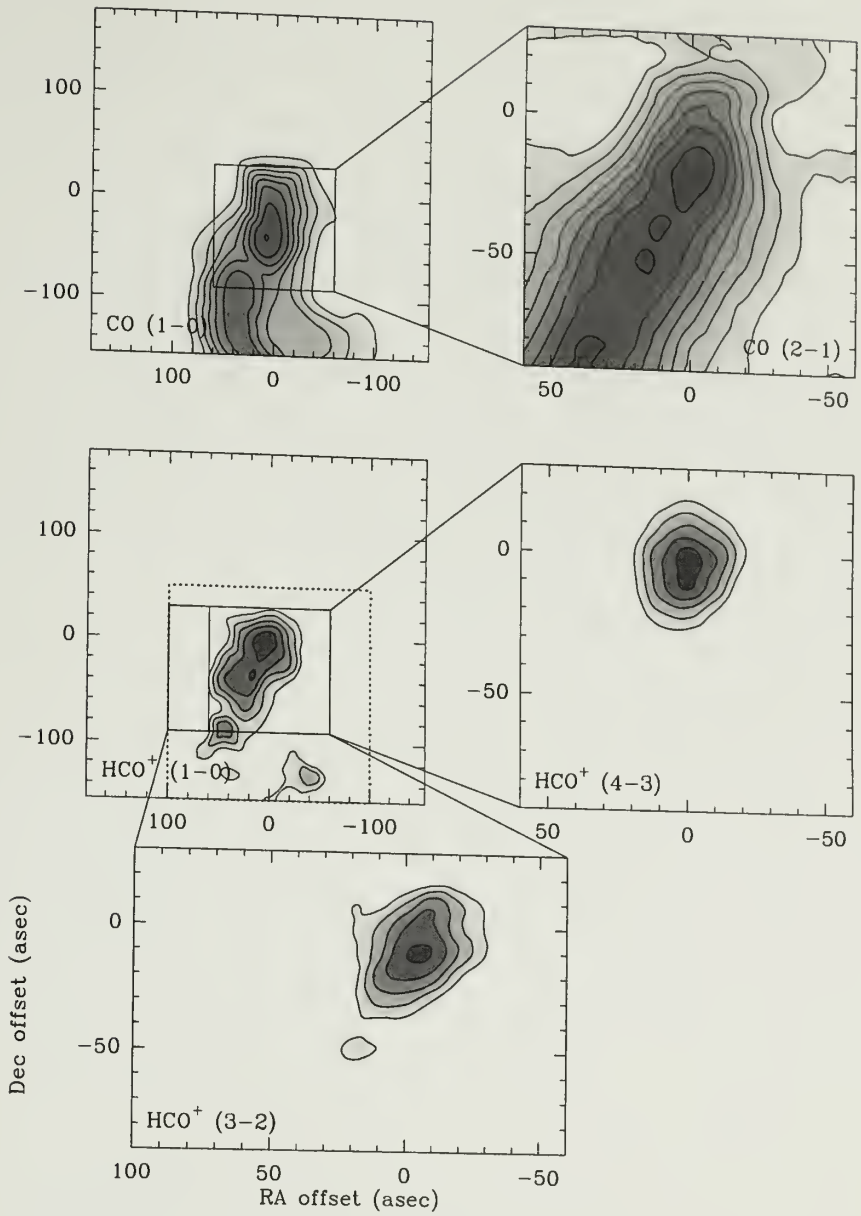

Figure 3.21 Integrated intensity maps of SFO 37. The IRAS source 21388+5622 is located at the center of each map. The CO ($J = 1 \rightarrow 0$) map has a lowest contour of 1.4 K km s^{-1} (3σ) and increments of 1.4 K km s^{-1} (3σ). The CO ($J = 2 \rightarrow 1$) map has a lowest contour of 1.6 K km s^{-1} (3σ) and increments of 2.6 K km s^{-1} (5σ). The HCO$^+$ ($J = 1 \rightarrow 0$) map has a lowest contour of 0.4 K km s^{-1} (3σ) and increments of 0.2 K km s^{-1} (1σ). The HCO$^+$ ($J = 3 \rightarrow 2$) map has a lowest contour of 0.8 K km s^{-1} (3σ) and increments of 0.3 K km s^{-1} (1σ). The HCO$^+$ ($J = 4 \rightarrow 3$) map has a lowest contour of 0.9 K km s^{-1} (3σ) and increments of 0.3 K km s^{-1} (1σ). The dotted rectangle in the HCO$^+$ ($J = 1 \rightarrow 0$) map indicates the region over which the HCO$^+$ centroid is shown in figure 3.22.

star formation (Sugitani et al., 1999). The HCO^+ ($J = 1 \rightarrow 0$) map shows evidence of some fragmentation of the tail of the cometary cloud into what could potentially seed the cores of new sequentially driven star formation. The HCO^+ ($J = 3 \rightarrow 2$) and HCO^+ ($J = 4 \rightarrow 3$) integrated intensity maps pick up the dense gas surrounding the central IRAS source. The second core, located approximately 100″ behind the IRAS source, has a lower excitation temperature than the core surrounding the IRAS source, which may indicate that it is much less dense. Once the ionization front moves past the IRAS source, it could continue on to this second core, inducing star formation once again. The IRAS source would become another young star in the line of young stars which originated in this sequential star forming region.

3.3.2 Bok Globules

3.3.2.1 B335

The dark cloud B335 has been well studied. The embedded IRAS source 19345+0727 appears to be a protostellar core which is the source of a bipolar outflow which is oriented in the east-west direction on the plane of the sky. The central source shows an elongation in the far-infrared and submillimeter continuum in the north-south direction, orthogonal to the outflow (Chandler et al., 1990). The high visual extinction and lack of near-infrared emission (Chandler & Sargent, 1993; Anglada et al., 1992) indicates that it may be a class 0 source. Zhou et al. (1993) provide evidence for protostellar collapse in B335 using H_2CO and CS observations. Subsequently, Zhou (1995) improved upon the infall models for B335 by including rotation and confirmed the earlier suggestion of infall. B335 is one of the best studied infall candidates, which is why we chose to observe it and compare it with the bright-rimmed clouds.

The B335 line profiles (Figure 3.20b) are very narrow compared to the other sources we've observed. The optically thin lines show a velocity width of only about

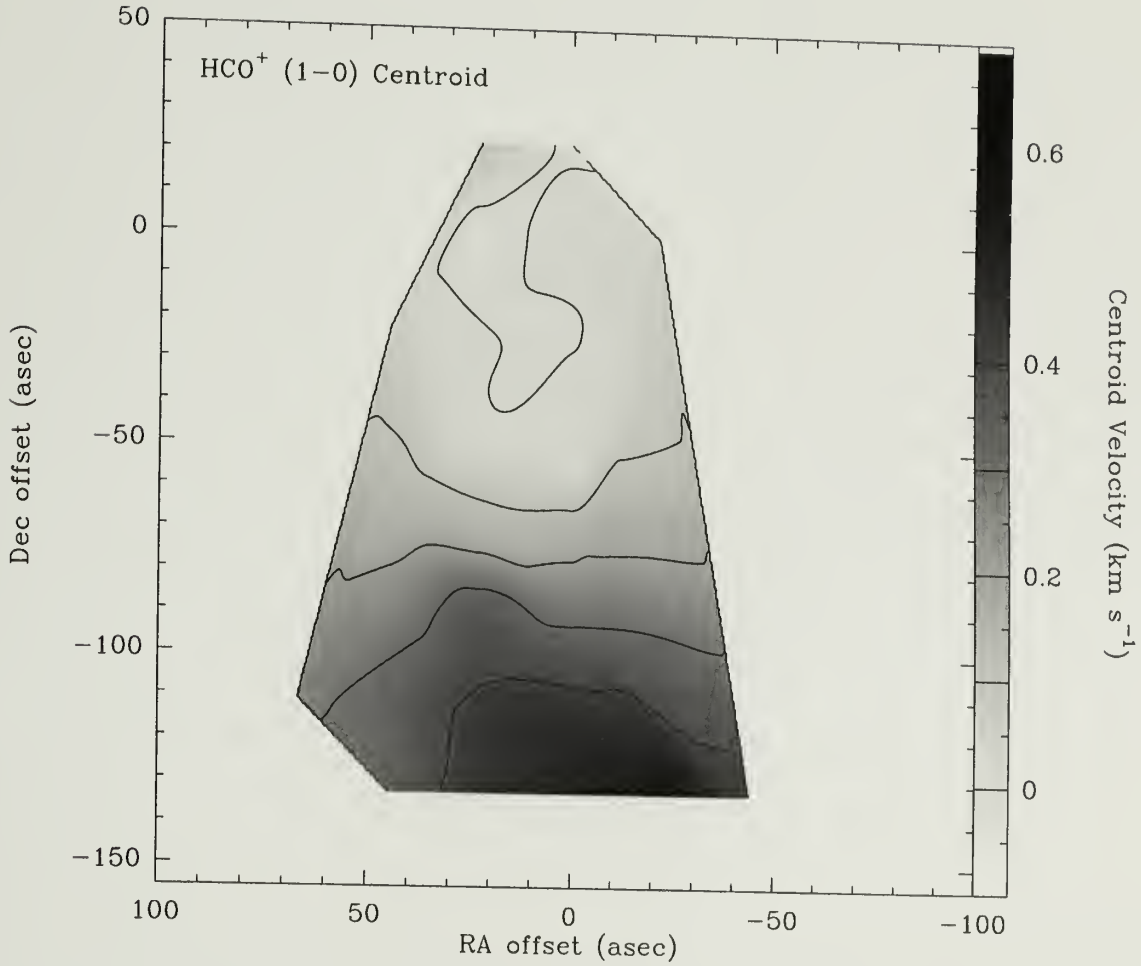

Figure 3.22 The SFO 37 centroid velocity integrated over the line core of HCO^+ ($J = 1 \rightarrow 0$). The line of sight velocity has been subtracted out and the contours and greyscale are indicated on the wedge to the right of the figure.

1 km s^{-1}. The HCO^+ $(J = 1 \rightarrow 0)$ profile shows a large self-absorption trough, however the centroid is not blue shifted, as one would expect for infall, but red-shifted. This is a result of the core rotation (Zhou, 1995) and the large beam of FCRAO. The HCO^+ $(J = 4 \rightarrow 3)$ line profile also shows self absorption, which results in a double-peaked spectrum. This spectrum, however, shows a considerable blue-shifted centroid relative to its isotopic counterpart. The $H^{13}CO^+$ $(J = 1 \rightarrow 0)$ and $H^{13}CO^+$ $(J = 4 \rightarrow 3)$ show single peaks right at the point where the HCO^+ lines are most self-absorbed, indicating that there is a high optical depth of HCO^+ at those velocities, and not that there are two different molecular cloud structures with slightly differing velocities in that direction.

The $C^{18}O$ $(J = 1 \rightarrow 0)$ and N_2H^+ $(J = 1 \rightarrow 0)$ emission is confined to the core, which does not seem to be resolved by our beam (Figure 3.23). The HCO^+ $(J = 1 \rightarrow 0)$ emission is resolved by the FCRAO beam, and seems to peak at the position of the IRAS core. The HCO^+ $(J = 1 \rightarrow 0)$ centroid map (Figure 3.24) does not indicate any coherent structure across the cloud. The HCO^+ $(J = 4 \rightarrow 3)$ emission is elongated in the east-west direction, along the outflow (Figure 3.23). The centroid velocity of HCO^+ $(J = 4 \rightarrow 3)$ has a coherent gradient running north-south indicating that B335 may be rotating around the axis defined by its outflow (Narayanan, 1997).

3.3.2.2 CB 3

CB 3 (Clemens & Barvainis, 1988), also known as L 594 (Lynds, 1965), is a Bok globule located approximately 2500 pc from us (Launhardt & Henning, 1997). Embedded within it is the IRAS source 00259+5625, which has an extremely high luminosity (930 $L_\odot$) and appears to be a source of isolated intermediate- or high- mass star formation, not typically associated with Bok globules (see Codella & Bachiller (1999) and references therein). Because this source is so distant and has such a

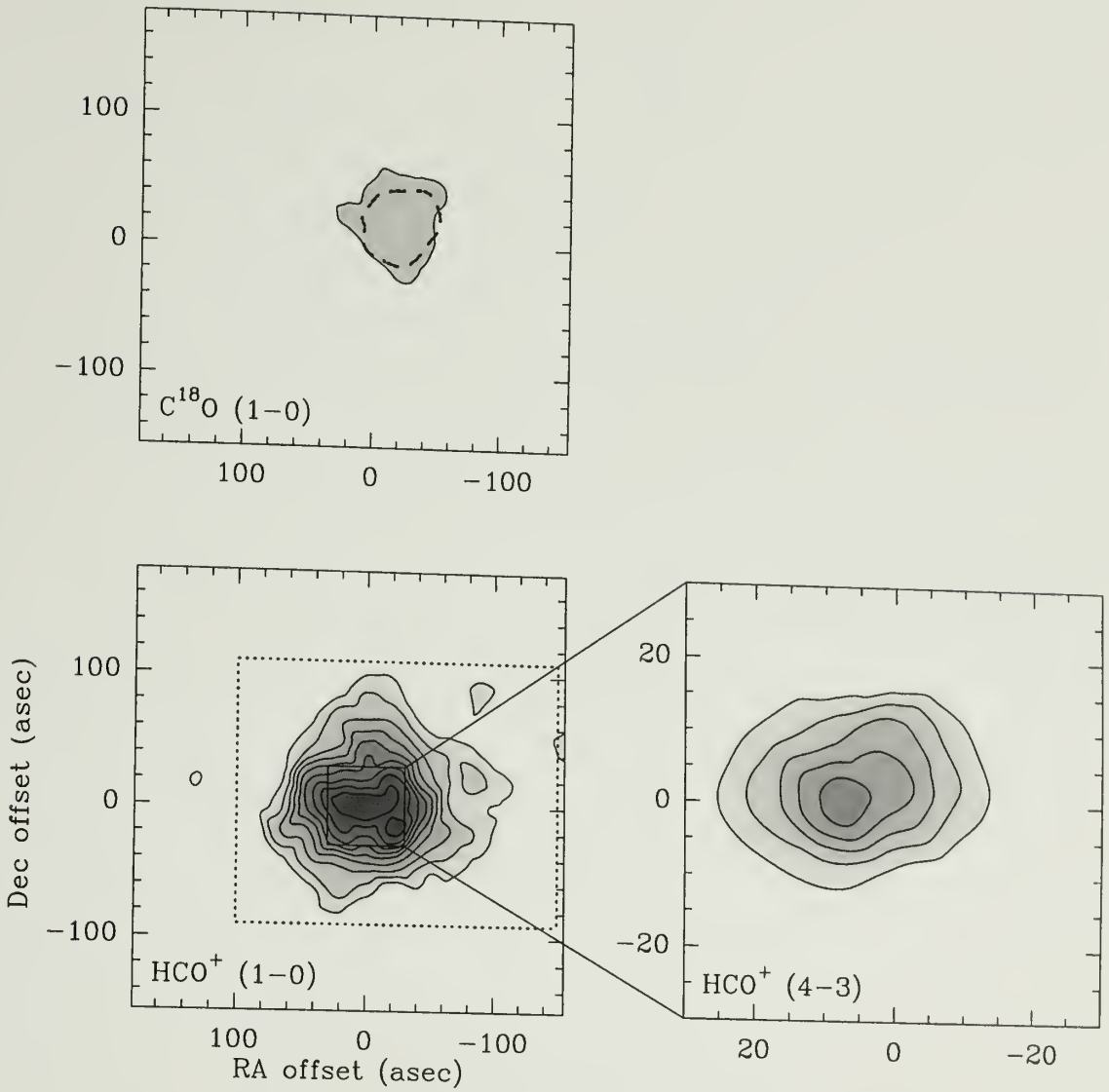

Figure 3.23 Integrated intensity maps of B335. The IRAS source 19345+0727 is located at the center of each map. The $C^{18}O$ ($J = 1 \rightarrow 0$) map has a lowest contour of 0.6 K km s^{-1} (3σ) and increments of 0.2 K km s^{-1} (1σ). The HCO^+ ($J = 1 \rightarrow 0$) map has a lowest contour of 0.3 K km s^{-1} (3σ) and increments of 0.1 K km s^{-1} (1σ). The HCO^+ ($J = 4 \rightarrow 3$) map has a lowest contour of 0.8 K km s^{-1} (3σ) and increments of 0.3 K km s^{-1} (1σ). The dotted rectangle in the HCO^+ ($J = 1 \rightarrow 0$) map indicates the region over which the HCO^+ centroid is shown in figure 3.24. The dashed contour in the $C^{18}O$ ($J = 1 \rightarrow 0$) indicates the half power contour of the N_2H^+ ($J = 1 \rightarrow 0$) emission.

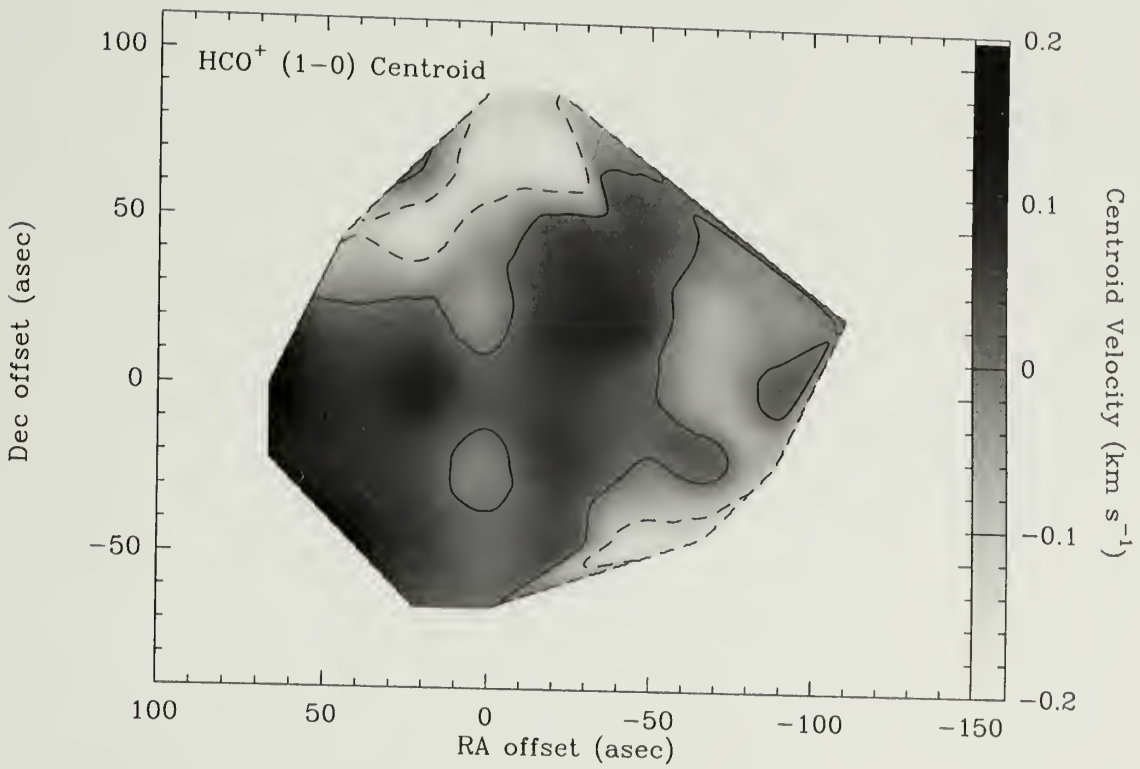

Figure 3.24 The B335 centroid velocity integrated over the line core of HCO^+ ($J = 1 \rightarrow 0$). The line of sight velocity has been subtracted out and the contours and greyscale are indicated on the wedge to the right of the figure.

high luminosity IRAS source it is not typically studied as a source of low-mass star formation, but it may be a good counterpart for the more distant bright-rimmed clouds, such as SFO 13, SFO 25, or SFO 37.

The CB 3 CO central line profiles (Figure 3.25a) are more complex than many of the bright-rimmed cloud's line profiles. Both the CO ($J = 1 \rightarrow 0$) and CO ($J = 2 \rightarrow 1$) profiles show a component near the N_2H^+ line center velocity, and a second component red shifted by a couple of km s^{-1} from the first. The $C^{18}O$ ($J = 1 \rightarrow 0$) line does not show two components, but does have a significant red shifted tail. The HCO^+ ($J = 1 \rightarrow 0$) central line profile is blue-shifted relative to both the N_2H^+ ($J = 1 \rightarrow 0$) line as well as the $H^{13}CO^+$ ($J = 1 \rightarrow 0$) line, which could indicate infall in the core. The HCO^+ ($J = 3 \rightarrow 2$) line shows less self-absorption on the red-shifted side of the line, but still has a centroid velocity which is slightly blue relative to the N_2H^+ profile.

The CO ($J = 1 \rightarrow 0$) integrated intensity map (Figure 3.26) shows a ridge of gas running northeast–southwest, but no peak at the core, however the CO ($J = 2 \rightarrow 1$) map clearly shows the core, which is displaced from the (0,0) position, but remains consistent with the error position of the IRAS source. The $C^{18}O$ ($J = 1 \rightarrow 0$) also highlights the position of the dense core along the low-density molecular gas ridge. The HCO^+ ($J = 1 \rightarrow 0$) integrated intensity map shows the gas core, with some extension along the ridge, however the HCO^+ ($J = 3 \rightarrow 2$) emission is centered only on the core position.

The HCO^+ ($J = 1 \rightarrow 0$) emission does not show a linear velocity gradient, but does have some structure (Figure 3.27). The CO ($J = 2 \rightarrow 1$) line wing map (Figure 3.28) shows a bipolar structure with the blue-shifted line wing to the south of the core and the red-shifted wing to the north. This indicates the probable presence of a bipolar outflow in this core. Our detection of this outflow is consistent with the outflow detected by Codella & Bachiller (1999).

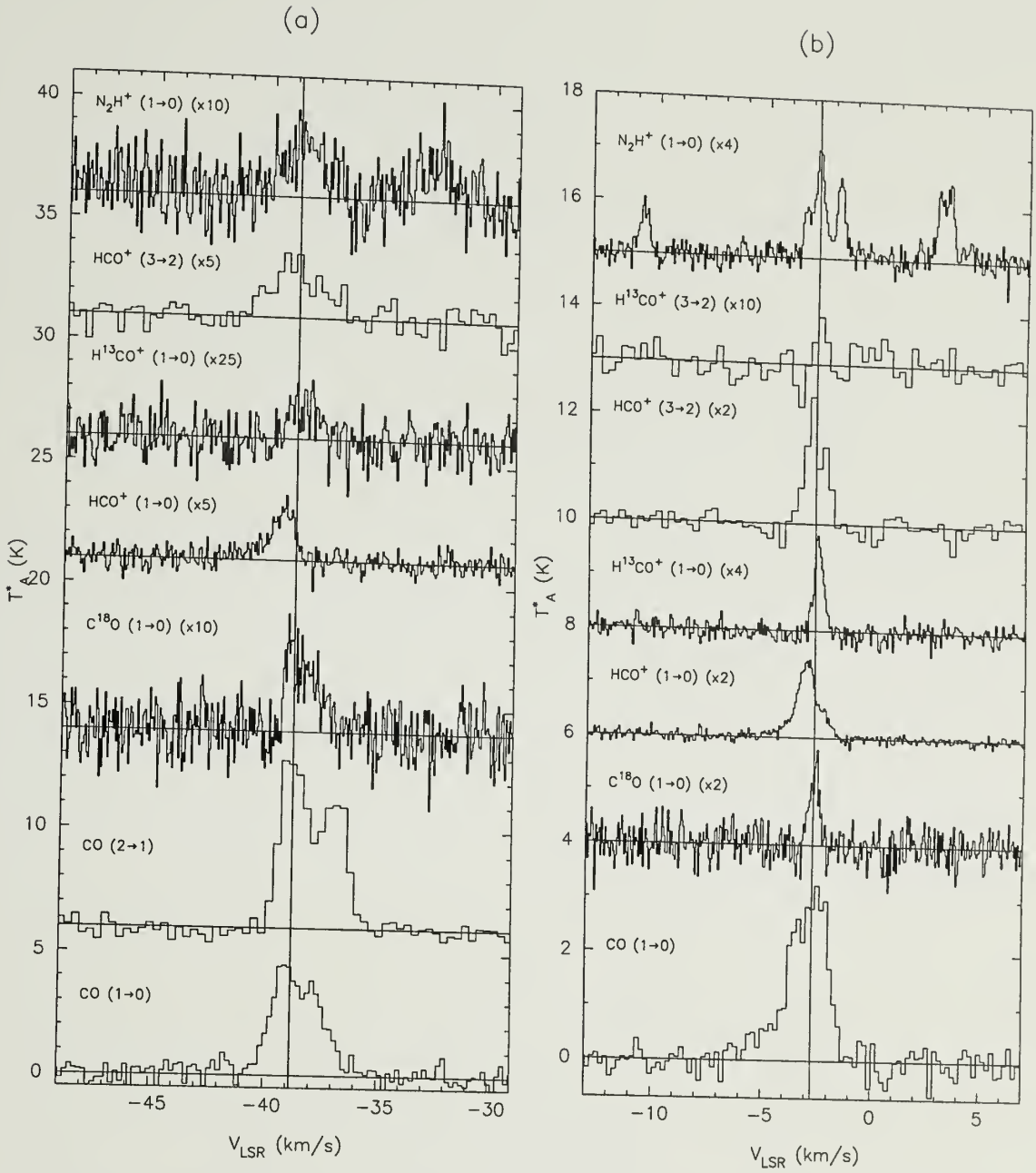

Figure 3.25 Line profiles of molecular transitions in the direction of the central IRAS source of CB 3 (a) and CB 224 (b).

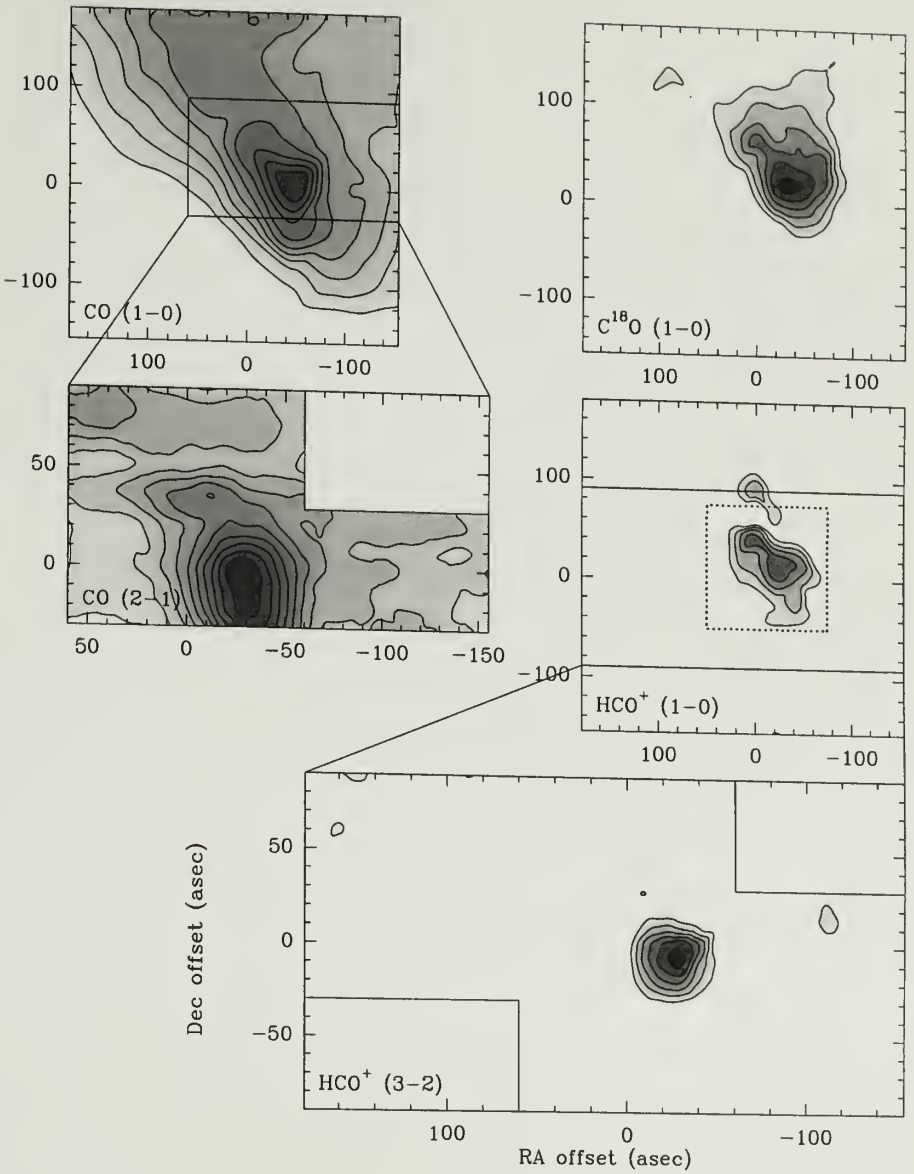

Figure 3.26 Integrated intensity maps of CB 3. The IRAS source 00259+5625 is located at the center of each map. The CO ($J = 1 \rightarrow 0$) map has a lowest contour of 2.2 K km s^{-1} (3σ) and increments of 2.2 K km s^{-1} (3σ). The CO ($J = 2 \rightarrow 1$) map has a lowest contour of 3.1 K km s^{-1} (3σ) and increments of 5.1 K km s^{-1} (5σ). The $C^{18}O$ ($J = 1 \rightarrow 0$) map has a lowest contour of 0.5 K km s^{-1} (3σ) and increments of 0.2 K km s^{-1} (1σ). The HCO^+ ($J = 1 \rightarrow 0$) map has a lowest contour of 0.5 K km s^{-1} (3σ) and increments of 0.2 K km s^{-1} (1σ). The HCO^+ ($J = 3 \rightarrow 2$) map has a lowest contour of 1.5 K km s^{-1} (3σ) and increments of 0.5 K km s^{-1} (3σ). The dotted rectangle in the HCO^+ ($J = 1 \rightarrow 0$) map indicates the region over which the HCO^+ centroid is shown in figure 3.27.

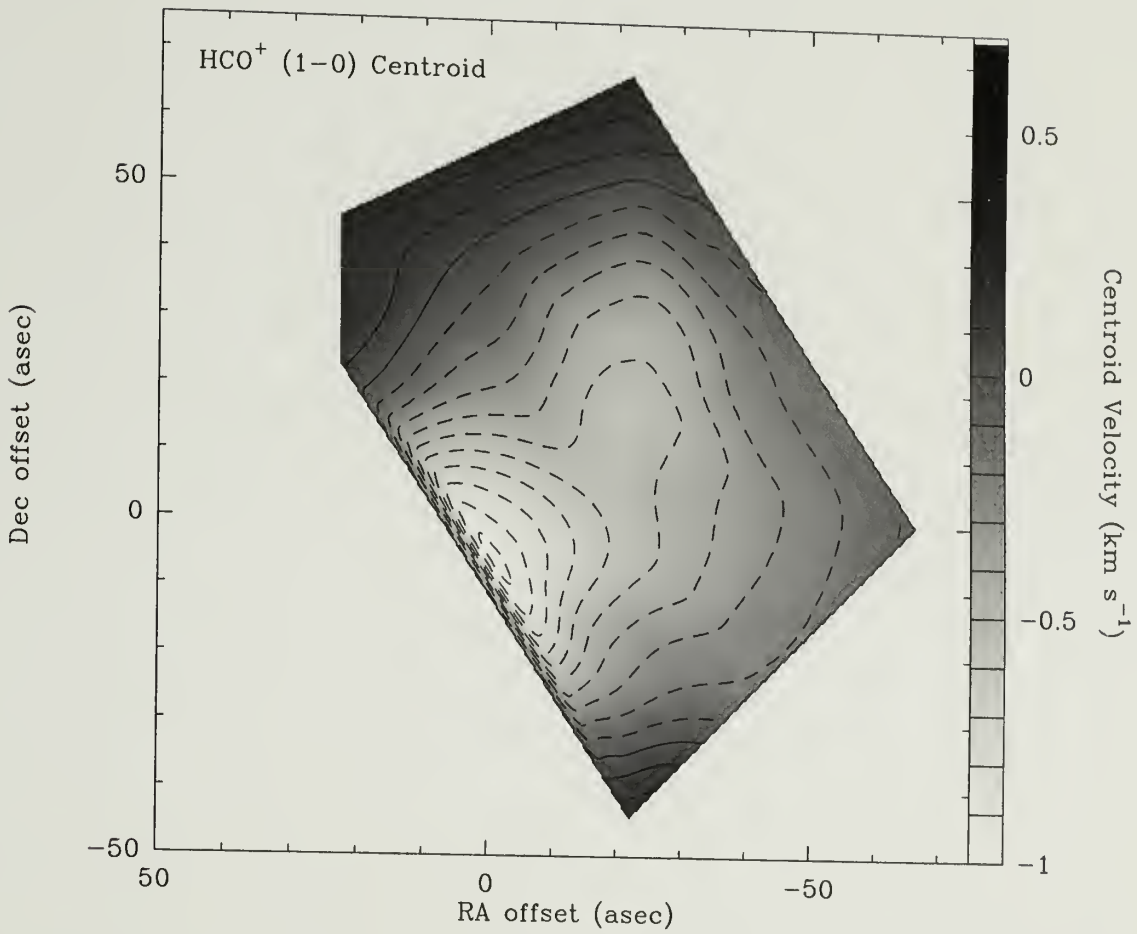

Figure 3.27 The CB 3 centroid velocity integrated over the line core of HCO^+ $(J = 1 \rightarrow 0)$. The line of sight velocity has been subtracted out and the contours and greyscale are indicated on the wedge to the right of the figure.

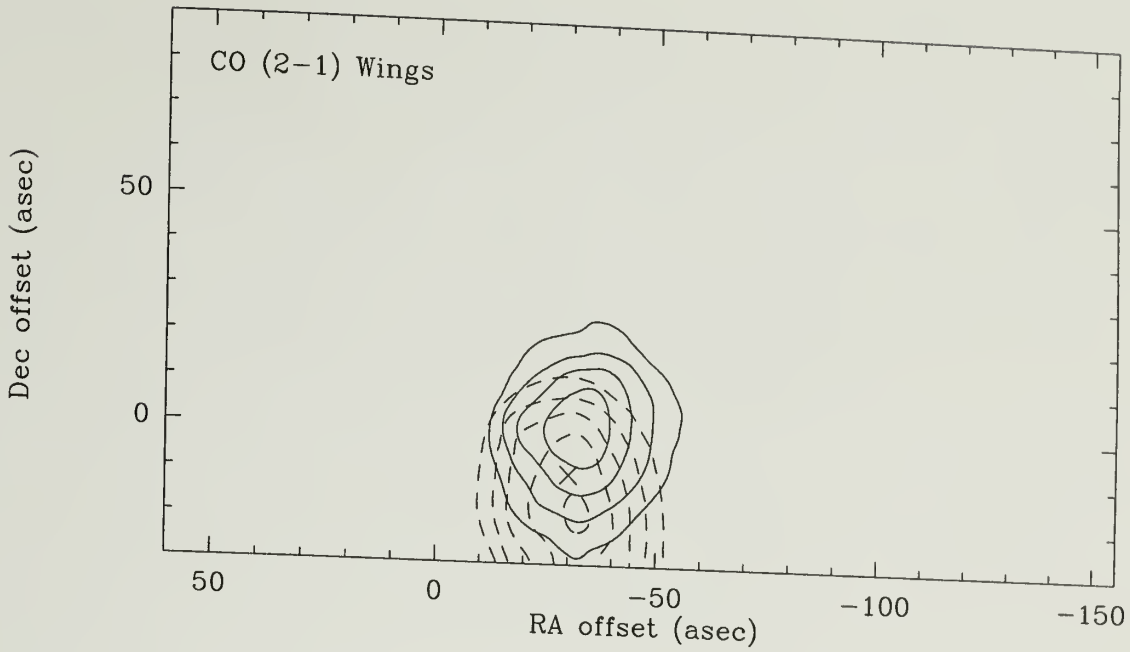

Figure 3.28 The CB 3 CO ($J = 2 \rightarrow 1$) line wing emission. The blue lobe, indicated by dotted lines, is the integrated intensity in the range of -49 to -39.5 km s^{-1}. The red lobe, indicated by solid lines, is the integrated intensity in the range from -37 to -29 km s^{-1}. The lowest contour in each case is the half power contour. The x indicates the HCO^+ ($J = 3 \rightarrow 2$) peak integrated intensity position.

3.3.2.3 CB 224

CB 224 (Clemens & Barvainis, 1988) is a Bok globule located at a distance of approximately 450 pc, and it's embedded IRAS source, 20355+6343, has a luminosity of 3.9 $L_\odot$ (Launhardt & Henning, 1997). This is very comparable to many of the SFO sources discussed above, making CB 224 a good isolated source to compare with the potentially triggered SFO sources. CB 224, however, has very weak molecular emission lines.

The CO ($J = 1 \rightarrow 0$) central line profile shows evidence of a blue-shifted wing, which is not present in the $C^{18}O$ ($J = 1 \rightarrow 0$) profile. This may indicate the presence of an outflow (Figure 3.25b). The HCO^+ ($J = 1 \rightarrow 0$) line profile is blue-shifted relative to both the N_2H^+ emission, and the $H^{13}CO^+$ ($J = 1 \rightarrow 0$) emission profile. The HCO^+ ($J = 1 \rightarrow 0$) profile shows a knee right where the $H^{13}CO^+$ emission peaks indicating a fairly classical self-absorption profile typical of infall regions. The

HCO^+ ($J = 3 \rightarrow 2$) profile shows some evidence of a slight centroid blue-shift relative to the $H^{13}CO^+$ ($J = 3 \rightarrow 2$) line and the N_2H^+ ($J = 1 \rightarrow 0$) line, but it is not as convincing an infall signature as the lower energy transition.

The CO ($J = 1 \rightarrow 0$) integrated intensity map shows molecular emission is fairly ubiquitous around this source (Figure 3.29), however there are two CO peaks, one north and one south of the IRAS core. The HCO^+ ($J = 1 \rightarrow 0$) integrated intensity map clearly highlights the core gas surrounding the IRAS source at the center of the map. There is a gradient running northeast–southwest in the HCO^+ ($J = 1 \rightarrow 0$) centroid velocity which could indicate rotation in the core (Figure 3.30).

3.4 Core Masses

Of the seven bright-rimmed clouds observed and the three Bok globules, all the sources show evidence of a very dense core with the exception of SFO 4, which is unusual in that it appears to be a fairly diffuse cloud. Turner (1995) has shown that the N_2H^+ ($J = 1 \rightarrow 0$) transition can be a good probe of the properties of star forming cores. While CO, HCO^+, and other molecules have a tendency to freeze on to grains in the low temperature, high density environment of cores, N_2H^+ remains relatively undepleted (Bergin & Langer, 1997) in dark cloud cores, making it a good probe of the density profile. N_2H^+ ($J = 1 \rightarrow 0$) also has several fine structure lines (Caselli et al., 1995) which can be used to derive the excitation temperature of the N_2H^+ ($J = 1 \rightarrow 0$) line. We use the "hyperfine structure (hfs) method" in CLASS (Forveille et al., 1989) to derive these properties from the N_2H^+ emission, using the component separations observed by Caselli et al. (1995). The excitation temperature and the optical depth derived from the hyperfine line ratios can be used to derive the column density of gas within the telescope beam, which can be related to the gas mass in the beam, assuming a relative abundance ratio between N_2H^+ and molecular hydrogen (Benson et al., 1998). We have performed this analysis for the objects

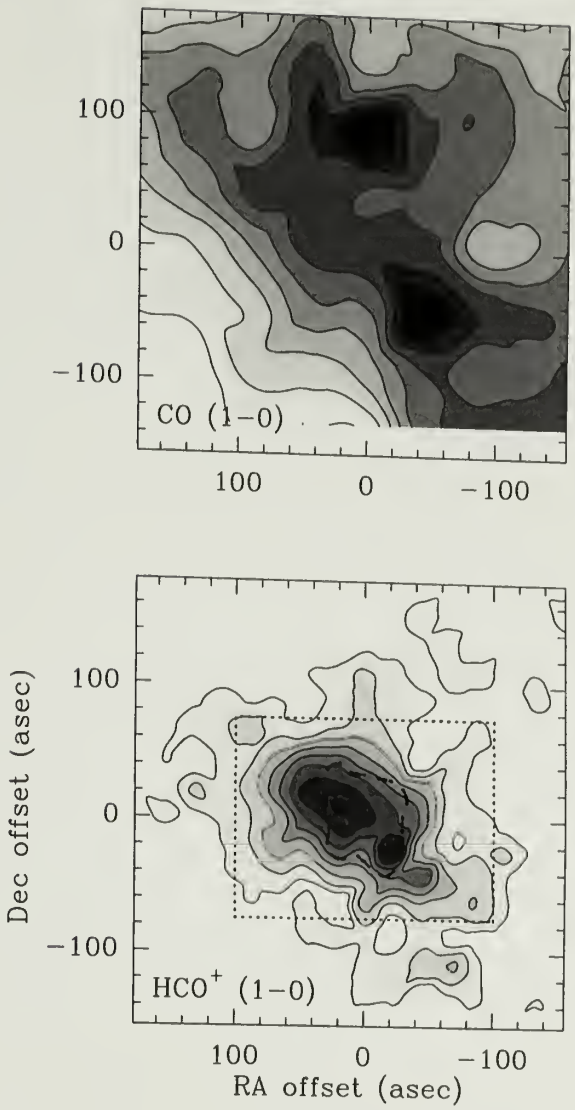

Figure 3.29 Integrated intensity maps of CB 224. The IRAS source 20355+6343 is located at the center of each map. The CO ($J = 1 \rightarrow 0$) map has a lowest contour of 2.4 K km s^{-1} (3σ) and increments of 0.8 K km s^{-1} (1σ). The HCO^+ ($J = 1 \rightarrow 0$) map has a lowest contour of 0.3 K km s^{-1} (3σ) and increments of 0.1 K km s^{-1} (1σ). The dotted rectangle in the HCO^+ ($J = 1 \rightarrow 0$) map indicates the region over which the HCO^+ centroid is shown in figure 3.30. The dashed contour in the HCO^+ ($J = 1 \rightarrow 0$) indicates the half power contour of the N_2H^+ ($J = 1 \rightarrow 0$) emission.

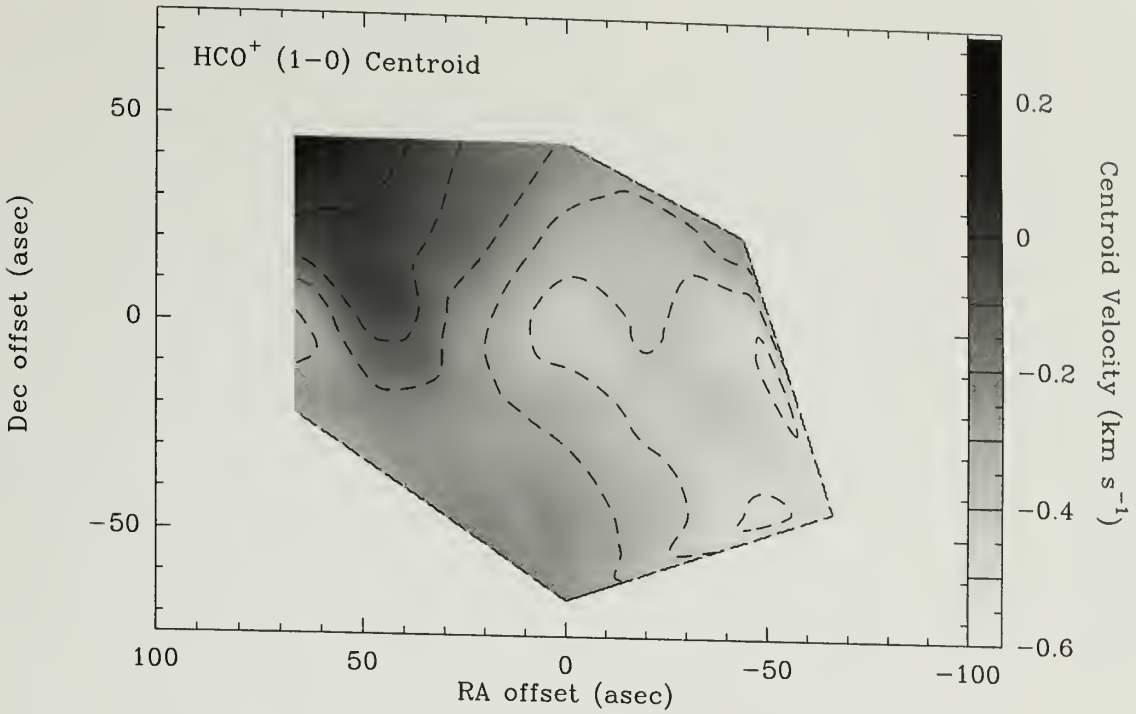

Figure 3.30 The CB 224 centroid velocity integrated over the line core of HCO^+ ($J = 1 \rightarrow 0$). The line of sight velocity has been subtracted out and the contours and greyscale are indicated on the wedge to the right of the figure.

in our sample, and the results are shown in Table 3.3, where T_{ex} is the excitation temperature, V_{LSR} is the line of sight velocity, ΔV is the line width, τ is the optical depth, N is the column density of N_2H^+, and M_{H_2} is the molecular mass of the core. The column densities of N_2H^+ fall within the same range of column densities observed in the cores of dark clouds (Benson et al., 1998).

The mass of the core can also be derived by comparing the emission of HCO^+ ($J = 1 \rightarrow 0$) to $H^{13}CO^+$ ($J = 1 \rightarrow 0$), under the assumption that the $H^{13}CO^+$ emission is optically thin. The optical depth can be derived from assuming an abundance ratio between the C and ^{13}C isotopes, and comparing the ratio of $H^{13}CO^+$ emission to HCO^+ emission. Then the excitation temperature is derived by assuming a filling factor of unity, and the excitation temperature and optical depth are used to derive the column density of gas. The results of this analysis are presented in table 3.4. It is encouraging to see that even though N_2H^+ and HCO^+ do not trace

Table 3.3. Observations of N_2H^+

Source	T_{ex} (K)	V_{LSR} (km s^{-1})	ΔV (km s^{-1})	τ	N (cm^{-2})	M_{H_2} ($M_\odot$)
SFO 13[a]	...	...	...	...	...	...
SFO 16	5.4 (1.0)	8.190 (0.002)	0.589 (0.017)	2.3 (0.9)	5×10^{12}	12
SFO 18	4.2 (0.2)	11.912 (0.015)	0.964 (0.038)	4.1 (0.6)	10×10^{12}	25
SFO 20[b]	...	13.007 (0.036)	0.589 (0.093)	0.6 (0.2)	1×10^{12}	3
SFO 25	5.0 (1.3)	7.287 (0.025)	1.832 (0.082)	0.8 (0.5)	5×10^{12}	50
SFO 37[b]	...	0.829 (0.103)	1.499 (0.503)	0.3 (0.2)	1×10^{12}	13
B335	3.6 (0.2)	8.362 (0.005)	0.376 (0.017)	11 (2)	8×10^{12}	8
CB 3	5.2 (8.6)	-38.843 (0.104)	1.789 (0.367)	0.459 (1.603)	3×10^{12}	270
CB 224	8.0 (6.4)	-2.729 (0.007)	0.450 (0.020)	0.785 (0.946)	2×10^{12}	8

[a]N_2H^+ ($J = 1 \rightarrow 0$) was not detected in this source down to an RMS of 0.067 K.

[b]The excitation temperature and optical depth were not well constrained due to the noise in this observation, however their combination was, so assuming an excitation temperature of 5 K yields the above mass estimates

Note. — These are the star formation core properties. η_{MB} is 0.5, $X(N_2H^+)$ is 7×10^{-10}, beamwidth is 52 arc seconds.

Table 3.4. Observations of HCO^+

Source	T_{main} (K)	T_{iso} (K)	ΔV (km s^{-1})	T_{ex} (K)	N_{main} (cm^{-2})	M_{H_2} ($M_\odot$)
SFO 4	0.221 (0.023)	< 0.037	3.0	...	$< 2 \times 10^{13}$	< 2
SFO 13	0.464 (0.020)	0.012 (0.014)	4.0	4.2	1×10^{13}	54
SFO 16	0.717 (0.007)	0.234 (0.007)	2.0	4.3	1×10^{14}	28
SFO 18	0.980 (0.007)	0.272 (0.006)	2.0	4.9	1×10^{14}	27
SFO 20	0.841 (0.013)	0.082 (0.008)	1.5	4.6	3×10^{13}	6
SFO 25	1.241 (0.015)	0.071 (0.012)	5.0	5.5	7×10^{13}	55
SFO 37	0.436 (0.014)	0.047 (0.006)	3.0	3.7	5×10^{13}	34
B335	0.786 (0.012)	0.280 (0.017)	1.0	4.4	8×10^{13}	6
CB 3	0.222 (0.043)	0.017 (0.019)	2.5	3.2	2×10^{13}	185
CB 224	0.664 (0.018)	0.302 (0.011)	0.8	4.2	8×10^{13}	21

Note. — These are the star forming core properties. η_{MB} is 0.46, $X(HCO^+)$ is 1×10^{-8}, beamwidth is 54.0 arc seconds, $C/^{13}C$ ratio is 64.0 (Pratap et al., 1997).

exactly the same gas they produce fairly comparable results for the overall core mass. These clouds tend to have cores with masses on the order of tens of solar masses.

3.5 Outflows

Outflows appear to be fairly ubiquitous in our sample. We detected outflows in nearly all the sources we surveyed. This is to be expected, since a star is forming and the cloud must dissipate its angular momentum in order to collapse. However, in the case of shock triggered regions, the ionization front does dissipate some of the angular momentum of the collapsing cloud (Elmegreen, 1992), though the ionization front would probably not have a noticeable effect on the scale of the accretion disk.

We have analyzed the energy in the detected outflows and present the results in table 3.5. We derived the mass of the lobes by averaging the integrated intensity of the line-wing emission over the spatial extend of the lobe. We then derived a column

density from this integrated intensity assuming that the emission is optically thin and an excitation temperature of 30K. The momentum (P) and kinetic energy (KE) of an outflow can be derived by computing

$$P = \sum_{\rm ch} m_{\rm ch} v_{\rm ch}, \text{ and KE} = \frac{1}{2} \sum_{\rm ch} m_{\rm ch} v_{\rm ch}^2$$

along the spatially averaged spectrum of the outflow lobe. Unless the outflow is along the line of sight, this method underestimates these quantities by a factor of $\sin(i)$ where i is the inclination of the outflow relative to the plane of the sky. As this method tends to underestimate the momentum and kinetic energy of the outflow, and since these estimates have fairly large uncertainties we chose not to integrate over the averaged spectrum, but instead to calculate the momentum to be $M_{\rm total} V_{\rm max}$ and kinetic energy to be $\frac{1}{2} M_{\rm total} V_{\rm max}^2$ where $M_{\rm total}$ is the total mass of the outflow lobe, and $V_{\rm max}$ is the maximum measured velocity of the outflow lobe relative to the line center. This assumes that all the material in the flow is moving at the maximum observed velocity, and that the lower velocities are the result of projection effects. This technique results in upper limit estimates of the flow's momentum and energy (Walker et al., 1988). The dynamical age (τ_d) of the flow is found by calculating the distance from the core to the edge of the outflow lobe and dividing by $V_{\rm max}$, while the kinetic luminosity (L) is derived by dividing the kinetic energy of the lobe by the dynamical age of the flow.

The dynamical ages and kinetic luminosities of these outflows tend to agree with those of previously observed outflow sources (Saraceno et al., 1996). The outflow ages all tend to be greater than 10^4 years, which may indicate that the embedded objects are class I sources rather than class 0 sources, which typically have outflow ages less than 10^4 years (Saraceno et al., 1996).

We compare the mechanical luminosity and force needed to accelerate the outflow to the luminosity and radiant pressure of the IRAS source driving the outflow in

Table 3.5. Outflow Characteristics

Source	$M_{\rm tot}$ ($M_\odot$)	P ($M_\odot$ km s^{-1})	KE ($M_\odot$ km^2 s^{-2})	$V_{\rm max}$ (km s^{-1})	τ_d (yr)	$\dot{M}$ ($M_\odot$ yr^{-1})	$\dot{P}$ ($M_\odot$ yr^{-1} km s^{-1})	L ($L_\odot$)
SFO 13 RL	8.9	75	310	8.4	80000	1.1×10^{-4}	9.3×10^{-4}	0.6
SFO 16 BL	0.3	2.4	10	8.2	35000	8.6×10^{-6}	7.1×10^{-5}	4.7×10^{-2}
SFO 16 RL	0.4	2.3	6.7	5.8	49000	8.1×10^{-6}	4.7×10^{-5}	2.2×10^{-2}
SFO 18 BL[a]	0.5	2.4	6.0	4.9	39000	1.3×10^{-5}	6.3×10^{-5}	2.5×10^{-2}
SFO 18 RL[a]	0.4	2.4	7.4	6.1	37000	1.1×10^{-5}	6.5×10^{-5}	3.3×10^{-2}
SFO 20 BL	0.01	0.03	0.04	3.0	25000	4.0×10^{-7}	1.2×10^{-6}	2.9×10^{-4}
SFO 20 RL	0.01	0.02	0.02	2.0	38000	2.6×10^{-7}	5.3×10^{-7}	8.6×10^{-5}
SFO 25 RL	2.3	24	130	10.7	24000	9.4×10^{-5}	1.0×10^{-3}	0.88
CB 3 BL	7.0	22	36	3.2	130000	5.4×10^{-5}	1.7×10^{-4}	4.5×10^{-2}
CB 3 RL	3.2	9.0	13	2.8	150000	2.2×10^{-5}	6.1×10^{-5}	1.4×10^{-2}

[a]SFO 18 values are based on CO ($J = 1 \rightarrow 0$) observations, $\eta_{\rm MB}$ is 0.45 in this case.

Note. — Assumes $\eta_{\rm MB}$ is 0.8, X(CO) is 1×10^{-4}, $T_{\rm ex}$ is 30 K.

Figure 3.31. We find that the bright-rimmed clouds occupy similar regions in the two plots indicating that they are probably driven by similar processes as the other outflows around forming stars that have been observed to date. We find that the embedded IRAS source has sufficient energy to drive the outflows we observe, but that the radiant pressure of the IRAS source is not sufficient to accelerate the outflows to the velocities we observe. This confirms similar observations of Lada (1985). The mechanism which accelerates these outflows is not a single scattering of photons from the IRAS source, but entrenchment in a bipolar flow thought to be driven by the interaction of an accretion disk and the stellar object's magnetic field.

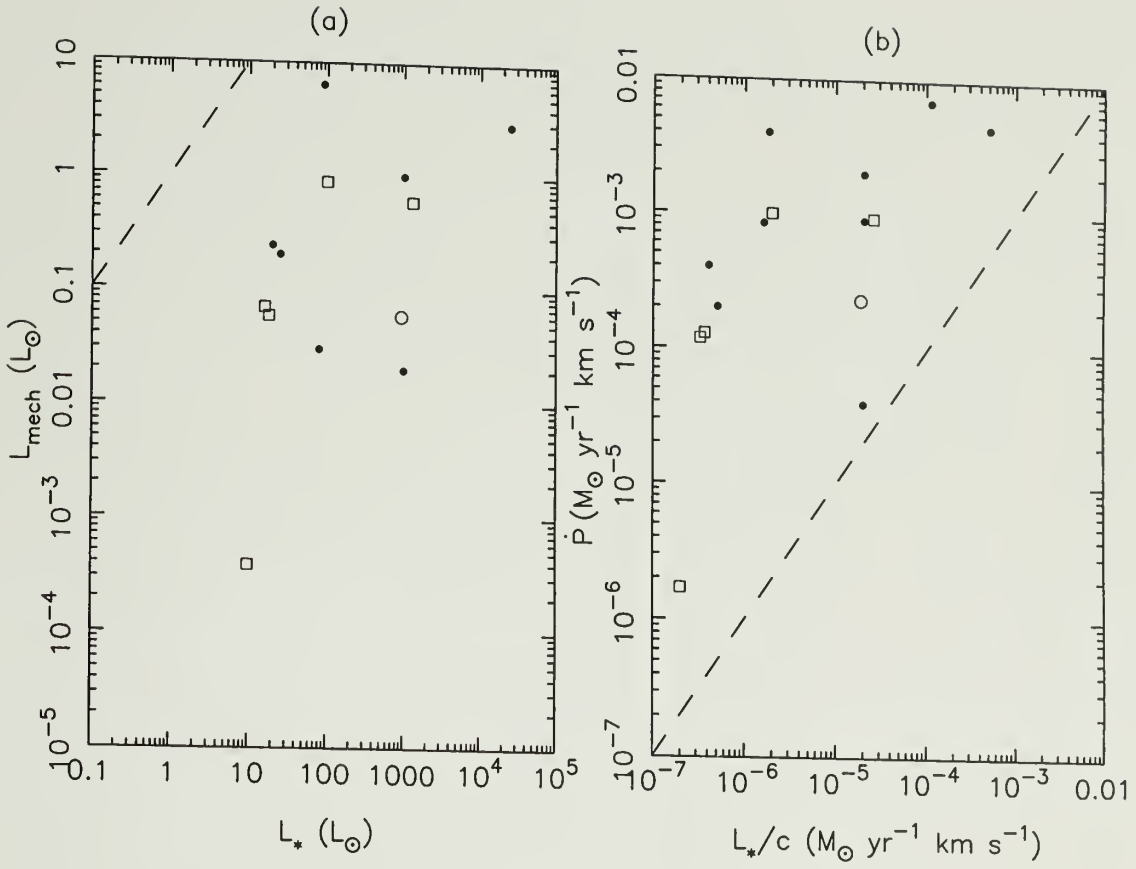

Figure 3.31 The energetics of the outflow are compared with those of the photons arising from the embedded IRAS sources we observed. The open squares represent the bright-rimmed clouds we observed, the open circle is CB 3 and the closed circles are data from Lada (1985). Figure (a) shows the outflow mechanical luminosity compared to the luminosity of the IRAS source. Figure (b) compares the force needed to accelerate the molecular outflows to the total radiant pressure of the central object. The dashed lines indicate where forces or luminosities are equal. The bright-rimmed clouds share similar properties with previously observed outflows, namely that although there exists enough energy in the central source to drive the outflows, radiative scattering is not the source of the outflow's acceleration.

CHAPTER 4
DISCUSSION OF MODELS AND OBSERVATIONS

4.1 Introduction

Comparing models and spectral line observations of star forming regions is complicated. The most complicating factor is that we are trying to reconstruct the three dimensional dynamic behavior of a gas cloud under the influence of gravity, magnetic fields, and it's own internal pressure from two spatial dimensions and one spectral dimension of data at one point in the cloud's evolution. Under such conditions it is generally impossible to construct a unique model which describes the physical state of the cloud (Stenholm & Pudritz, 1993). In the regions we have observed, there are a number of factors which help mitigate these effects. We have chosen regions which appear to have a fairly simple geometry, the bright-rimmed clouds are molecular clouds with ionization fronts from nearby HII regions sweeping up the molecular gas into a fairly well defined ridge. In other regions of cluster formation, multiple winds and shock fronts would confuse our analysis greatly. Even though we have chosen relatively simple regions to study, finding signatures of triggered star formation within bright-rimmed clouds remains difficult. We are unable to determine if there were preexisting self-gravitating cores within these clouds, or if the cores were induced to collapse as a result of the imposed shock front because we have no way of observing the evolution of each source. Nevertheless we do observe trends in our observations and in our models which are useful in uncovering the physical processes in these regions.

4.2 Infall Motion

4.2.1 Quantifying Blue Asymmetry in Line Profiles

Although several outflows were detected, and the presence of outflows implies infalling gas, there were few line asymmetries indicative of infall in the bright-rimmed clouds. Mardones et al. (1997) have defined a parameter to quantify the line asymmetry in terms of the line center velocity of an optically thick line, the line center velocity of an optically thin line, and the width of the optically thin line. The asymmetry (δV) is then defined as

$$\delta V = (V_{\rm thick} - V_{\rm thin}) / \Delta V_{\rm thin}.$$

Mardones et al. (1997) find the line center velocities of both the thick and thin lines by fitting a gaussian to the lines. However using gaussian fits does not yield a very robust estimator of the asymmetry. As the optical depth increases, the thick line does immediately separate into two distinguishable components. At moderate optical depths a knee forms in the line profile as the peak becomes blue-shifted. A gaussian fit to this type of profile is very inaccurate. The centroid velocity of a line is a better determined quantity. Therefore we use the centroid velocity of the thick line when calculating the line asymmetry. The thin line is usually very close to a gaussian, so we use a gaussian fit to determine the velocity of the thin line.

We tabulate our line asymmetry values in table 4.1. The millimeter asymmetry is derived from observations of the HCO^+ ($J = 1 \rightarrow 0$) optically thick line and the $H^{13}CO^+$ ($J = 1 \rightarrow 0$) optically thin line. The submillimeter asymmetry value is derived from the observations of the HCO^+ ($J = 3 \rightarrow 2$) optically thick line and the $H^{13}CO^+$ ($J = 3 \rightarrow 2$) optically thin line. Mardones et al. (1997) suggest that a δV between –0.25 and 0.25 be considered symmetric. All the bright-rimmed clouds, with the exception of SFO 18, show no significant asymmetry in their central line profiles according to this criterion.

Table 4.1. Line Asymmetries

Source	Millimeter Asymmetry	Submillimeter Asymmetry
SFO 13	-0.11 ± 0.10	-0.32 ± 0.19
SFO 16	-0.14 ± 0.01	0.20 ± 0.13
SFO 18	-0.48 ± 0.02	-0.59 ± 0.06
SFO 20	-0.01 ± 0.05	0.38 ± 1.34
SFO 25	-0.01 ± 0.02	0.03 ± 0.12
SFO 37	0.08 ± 0.05	-0.15 ± 0.06
B 335	-0.09 ± 0.03	-0.13 ± 0.04
CB 3	-0.84 ± 0.14	-3.79 ± 11.83
CB 224	-1.20 ± 0.06	-0.27 ± 0.16

Previous studies of class 0 and class I sources performed using the millimeter CS ($J = 2 \rightarrow 1$) transition (Mardones et al., 1997) and the submillimeter HCO^+ ($J = 3 \rightarrow 2$) transition (Gregersen et al., 2000) show preferentially blue asymmetric line profiles, thought to be the result of infall in these star forming cores. Mardones et al. (1997) quantify the overall predilection of the observed sources to have blue asymmetric line profiles in terms of a parameter they call the "blue excess" which is defines as

$$\text{blue excess} = \frac{N_{\text{blue}} - N_{\text{red}}}{N_{\text{total}}}, \tag{4.1}$$

where N_{blue} is the number of sources with $\delta V < -0.25$, N_{red} is the number of sources with $\delta V > 0.25$, and N_{total} is the total number of sources. Gregersen et al. (2000) find a blue excess of 0.28 for the class 0 and class I sources they observe, and an overall blue excess of 0.31 for all the sources in the literature. The bright-rimmed clouds have a blue excess of 0.2 measured in both the millimeter and submillimeter transitions, however that is measured with a sample of only 6 sources. A scatter plot, comparing the asymmetry of the bright-rimmed clouds and Bok globules we observed with those observed by Mardones et al. (1997) and Gregersen et al. (2000) is shown in Figure 4.1. In the same figure, we also indicate the modeled line asymmetries for two of the VC

hydrodynamic models which collapsed to form a single gravitationally bound core. We see that the bright-rimmed clouds show asymmetry values comparable to those of other star forming regions. The bright-rimmed clouds, however, do not show as wide a deviation of asymmetry values, and tend to have δVs which are closer to 0 than typical star formation regions, whose δVs tend to be negative. Even the modeled clouds tend to show no significant asymmetry at all. A wider survey of bright-rimmed clouds is required to determine if they indeed have significantly less blue excess than other YSOs.

4.2.2 The Role of Temperature Gradient in Line Formation

Why do we not detect infall in more bright-rimmed clouds? Does the incoming shock front produce conditions that alter the shape of the emergent line profile? An isolated Bok globule usually has an excitation temperature profile which drops from a value on the order of 20–50K at the core center to 10K at the edge of the core (Launhardt & Henning, 1997). Bright-rimmed clouds, however, are stripped of their molecular envelopes and heated by UV flux from O stars. This may be expected to flatten or in some cases invert the temperature profile, so that the center of the cloud core may still have a physical temperature around 20K, but the edge of the cloud core may have a physical temperature of several hundred K. Since the gas throughout the core is fairly excited, it would eliminate the self-absorption which characterizes the blue line asymmetry typically associated with infall. This inversion of the excitation temperature gradient could even lead to absorption of the blue-shifted gas by denser, yet less excited gas closer to the core. Figure 4.2 illustrates the effect of inverting the temperature gradient on a free-falling infall region. The model presented in that figure is a collapsing region following the theoretical model proposed for a collapsing non-rotating free-falling sphere proposed by Shu (1977). There is a peak molecular hydrogen density of 10^7 cm^{-3} at the center of the cloud, which drops down to a density

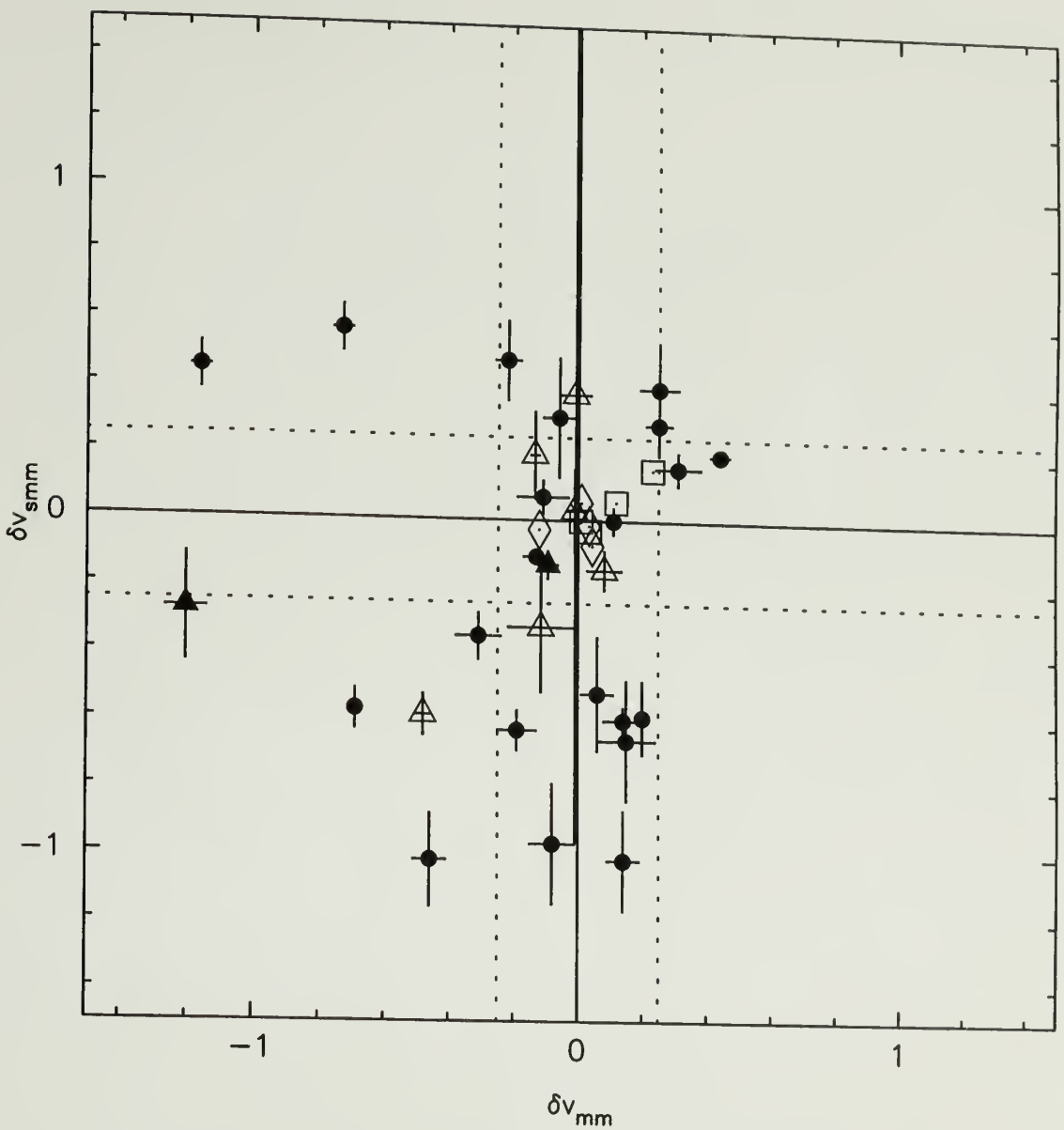

Figure 4.1 The line asymmetry parameter (δV) towards the star forming core measured in both millimeter (x–axis) and submillimeter (y–axis) molecular transitions. The open triangles are the bright-rimmed clouds reviewed in this dissertation observed in the millimeter transition HCO^+ ($J = 1 \rightarrow 0$) and the submillimeter transition HCO^+ ($J = 3 \rightarrow 2$). The filled triangles are the Bok globules we observed in the same transitions as the bright-rimmed clouds. Models of the asymmetry parameters are presented as open squares for timesteps in VC simulation F and open diamonds for timesteps of VC simulation Q. The filled circles are class I and class 0 sources observed in the millimeter CS ($J = 2 \rightarrow 1$) transition by Mardones et al. (1997) and in the submillimeter HCO^+ ($J = 3 \rightarrow 2$) transition by Gregersen et al. (2000).

of 3×10^4 cm^{-3} at a distance 8000 AU. The beam we use to observe the simulated cloud has a width of about 3000 AU. The only difference between the models we simulate is the temperature gradient within the cloud. The "Standard Infall" model assumes the standard temperature gradient from the Shu (1977) model, which peaks at 115 K in the center and drops to 14 K at 8000 AU. The "Inverted Infall" model assumes a linear temperature gradient which is 10 K at the center of the cloud, and 150 K at 800 AU. The 150 K temperature is typical of the temperatures near the edges of the molecular cores in the VC hydrodynamic models. Our "Mixed Infall" model is a combination of the Shu (1977) temperature gradient, which dominates near the center of the cloud, and our linear gradient which dominates in the outer regions of the cloud. In this case we have chosen the greater of either the "Standard Infall" model or "Inverted Infall" model temperature.

We have simulated the modeled profiles in Figure 4.2 using the LTE and LVG methods which we developed as well as with the Hogerheijde & van der Tak (2000) one dimensional Monte Carlo model. All three models indicate that the blue-asymmetric line profile, easily observed in the "Standard Infall" model is suppressed in both the "Inverted Infall" and "Mixed Infall" models. This may explain why we see less evidence of infall asymmetry in bright-rimmed clouds than in Bok globules. Our model shows that heating of the envelope of a collapsing cloud can lessen or remove entirely the blue-asymmetric line signature of a collapsing molecular cloud. This calls into question the long established procedure of finding infalling regions by looking for a blue-asymmetric line profile. In complex regions, where the temperature gradient might not always be peaked at the center of a collapsing cloud core, one cannot rely on the blue-asymmetric line profile to identify regions of collapse.

Another result of our modeling is how well the LVG approximated line profiles match the line shape of the more rigorous Monte Carlo models. The overall intensity of the LVG modeled line profiles is about a factor of 2 below the Monte Carlo models.

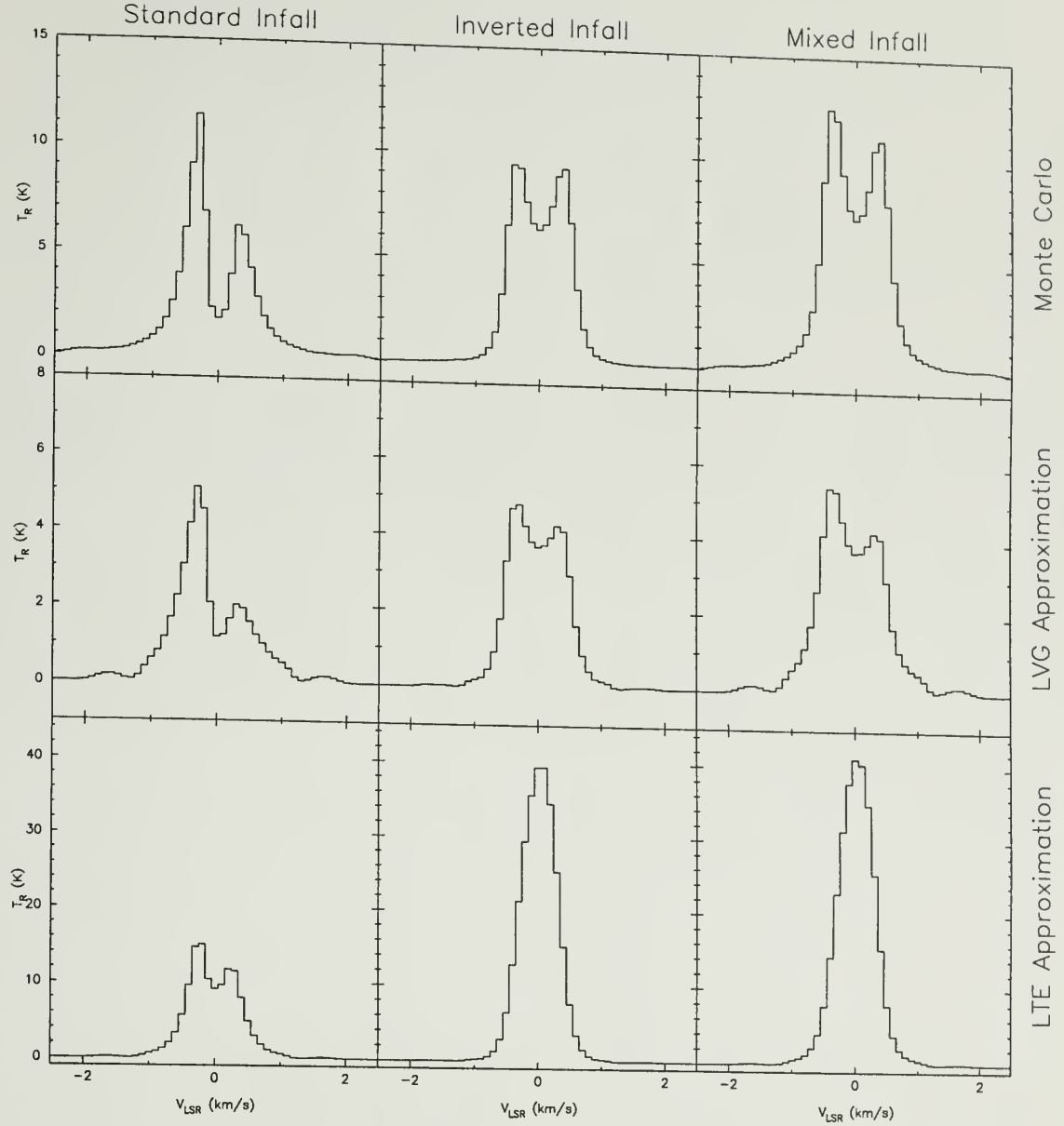

Figure 4.2 Effect of temperature gradient on infall asymmetry. Modeled spectra of the effect of changing the temperature gradient for an inside-out collapsing spherical cloud (Shu, 1977). The first column is the modeled HCO^+ ($J = 3 \rightarrow 2$) line profile assuming the standard Shu (1977) model and an HCO^+relative abundance of 2×10^{-9}. The second column is equal to the Shu (1977) model except the temperature gradient increases linearly from 10 K at the center of the cloud to 150 K at the outer edge. The third column uses the Shu (1977) model again, but has a temperature gradient that matches the Shu (1977) in the core before increasing to 150 K at the edge. The first row employs Hogerheijde & van der Tak (2000) Monte Carlo radiative transfer, the second row employs our LVG approximation, and the third row employs the LTE approximation.

This is due to the fact that much of the excitation to the $J = 3$ rotational level population of the HCO^+ molecule is due to stimulated excitation from radiation arising from other cloud radii. Our LVG model simulates only the effect of local stimulated absorption and can not completely reproduce the level population, but even without fully reproducing the level populations, the LVG model simulates the trends in the level populations well enough to capture the change in line shapes as a result of varying the temperature profile. The LTE approximation on the other hand shows no self-absorption dips at all in the "Inverted Infall" and "Mixed Infall" models as in those cases the emission in the LTE cases is dominated by the hot outer radius of the cloud.

4.2.3 Observed Temperature Gradients in Bright-Rimmed Clouds

In order to test the assumption that the ionization front may be raising the temperature near the edge of the cloud, we estimate the variation of excitation temperature with radius in a bright-rimmed cloud core and a Bok globule. We have smoothed the HCO^+ ($J = 3 \rightarrow 2$) map to the same resolution as the HCO^+ ($J = 1 \rightarrow 0$) in both a bright-rimmed cloud (SFO 25) and a Bok globule (CB 3) which we observed (from Chapter 3). We assume thermodynamic equilibrium between these transitions, as well as a low optical depth in order to derive the excitation temperature across the core. SFO 25 has fairly gaussian lines, centered at the same velocity as their isotopic counterparts, indicating that the HCO^+ emission for this source may be optically thin. In CB 3, as in all the Bok globules we observed, we know the HCO^+ emission is not optically thin, however this would tend to wash out the excitation temperature to the cloud core, so in regions where the emission is optically thick we can consider the derived excitation temperature to be a lower limit. Towards the edge of the CB 3 core the HCO^+ emission does become optically thin making this a good assumption. In the case of SFO 25 we derive the excitation temperature along a line which cuts

through both the ionization front and the star forming core, and plot that excitation temperature profile in Figure 4.3a. The center (0″) offset represents the star forming core position, and the ionization front is in the negative direction. Figure 4.3b shows the excitation temperature profile around the core of CB 3, however we averaged annuli around the central core in order to derive the plotted values, rather than take a cut straight across in order to maximize our signal to noise ratio. In the case of SFO 25, the excitation temperature peaks near the edge of the cloud core, while in CB 3 the excitation temperature peaks near the center. Although it is likely that the cores of these bright-rimmed clouds are collapsing in a similar manner to other class 0 or class I sources, the heating due to the nearby HII region may dampen their spectral line infall signature.

4.3 Velocity Shears in Models and Observations

When an HII region is formed by a new star, the resulting ionization front is preceded by a shock front. The molecular gas core can serve to retard the progress of the ionization front, but the shock front should have passed through the region before the ionization front. Does the shock front which precedes the ionization front play a role in creating the morphologies we observe? One way we may approach this question is to study the velocity field of the molecular gas well behind the ionization front to see if it carries and kinematic signature of the initial shock.

There are several other factors which may contribute to apparent velocity shears in the molecular emission. If we rely on the centroid maps to look for velocity shears then effects such as rotation and variable self-absorption due to density gradients in the cloud can create apparent shears even in molecular gas without a systematic velocity gradient across it. The molecular gas in the type B and type C morphologies is also partially or fully surrounded by ionized gas. It is not possible to observe a line of sight into the molecular gas in these cases without looking through the boundary

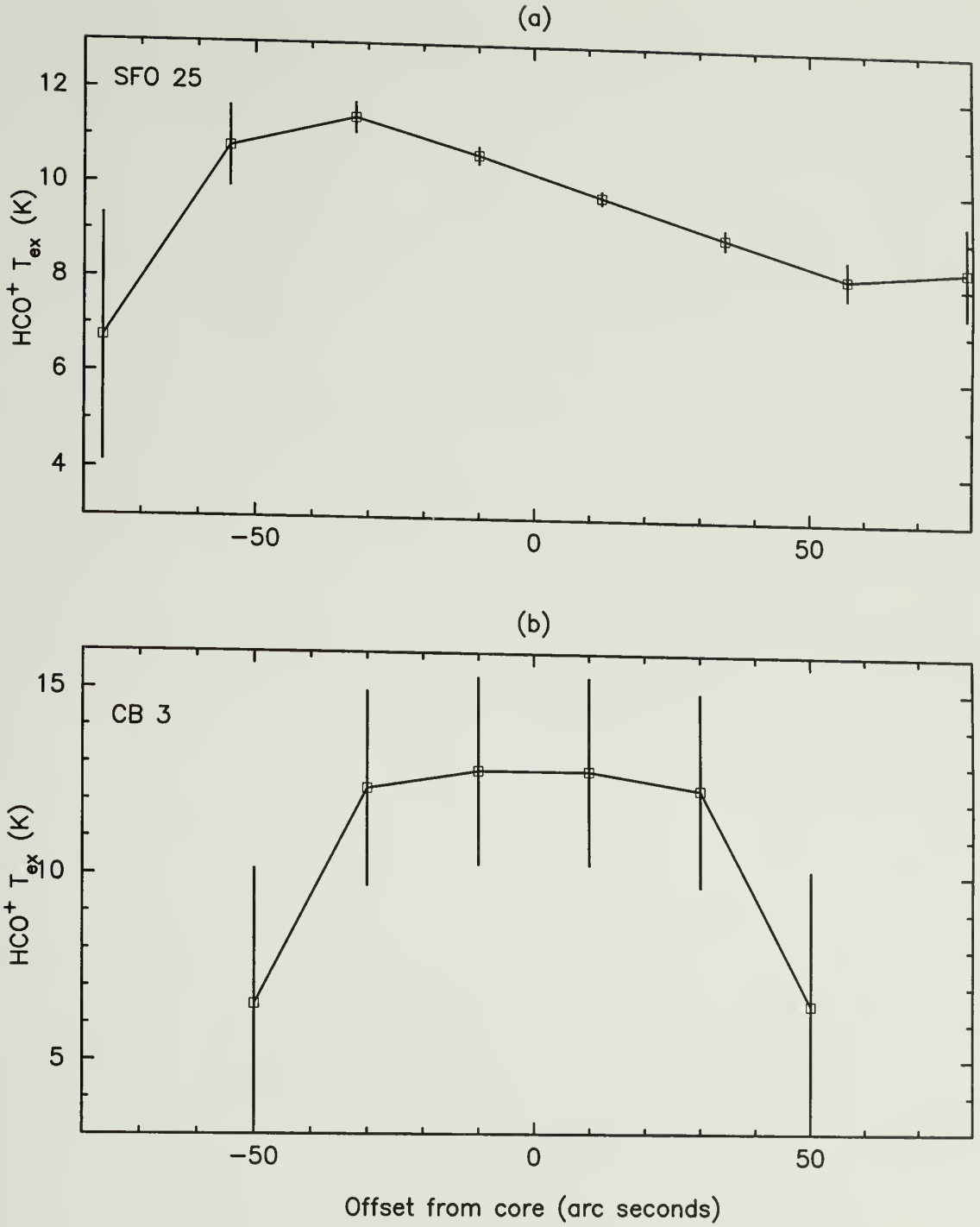

Figure 4.3 Excitation temperature profiles measured across an observed bright-rimmed cloud and a Bok globule. Under the assumption of thermodynamic equilibrium and low optical depth we derive the excitation temperature profiles across both a bright-rimmed cloud (SFO 25, a) and a Bok globule (CB 3, b). For the bright-rimmed cloud our cut ran along the line from the ionizing source to the core, with the shock front on the negative side of the core. For the Bok globule we averaged annuli around to core and calculated the excitation temperature in each annulus.

layer where the kinematic effects of the interaction of the molecular cloud and the ionization front are superimposed on the kinematic signature of the shielded molecular gas.

By looking at a molecular tracer which is not well excited by shocks and optically thin we can alleviate the above concerns and look for velocity shears imposed by the shock which precedes the ionization front. Our synthetic observations in §2.5 indicate that HCO^+ velocity centroids are largely influenced by the swept up molecular gas. Even though the molecular gas shielded from the wind by the molecular cloud core does not have any imposed velocity, we see velocity shears from the swept up gas along the line of sight. Our models indicate that HCO^+ is not a suitable tracer for examining this effect. We must perform more modeling to identify a tracer which traces the undisturbed molecular gas in the cometary tail rather than the swept up gas surrounding the tail and then observe bright-rimmed clouds using this tracer in order to observe kinematic effect of a shock front which precedes the ionization front on bright-rimmed clouds.

4.4 Head-Tail Intensity Contrast as an Indicator of Star Formation

Although we have engaged in a detailed survey of bright-rimmed clouds, and we have made synthetic observations of hydrodynamic models of wind blown implosion, we do not see a simple observational signature which indicates whether a cloud core will be induced to form a star. We have, however, noticed a trend in those modeled cores which do form stars. As we saw in Chapter 2, the ratio of submillimeter line emission intensity of the head or core of bright-rimmed clouds modeled by VC relative to the emission in the tail tends to be higher in those clouds in which stars form than in those in which the core is ripped apart by the shock front. In this section we will

quantify those ratios in the models and compare them to those we observe in our survey of bright-rimmed clouds.

We present the ratio of core to tail intensity in HCO^+ ($J = 3 \rightarrow 2$) emission in Table 4.2. We choose HCO^+ ($J = 3 \rightarrow 2$) emission as we find that the effect is greatest in the higher submillimeter transitions of HCO^+, and we have HCO^+ ($J = 3 \rightarrow 2$) data for all the bright-rimmed clouds in our sample, but only HCO^+ ($J = 4 \rightarrow 3$) data from a couple of clouds. We note in the hydrodynamic models that the two runs which formed a single core (F and Q) have the highest ratio of head to tail emission intensity, while the two runs which did not collapse (O and K) have a lower ratio. Run I, which formed a binary system, also has a small ratio of head to tail emission intensity. This is a more complex region which we will ignore for the time being. In many of our observations we do not manage to detect the tail HCO^+ ($J = 3 \rightarrow 2$) emission as it would have required much longer integration times, however the data we have allows us to set a lower limit on the head to tail intensity ratio. We find that most of the cores have a minimum intensity ratio of approximately 2 or 3. This is the same ratio as those hydrodynamic models which did not collapse to form self-gravitating cores, although it is probable that the actual ratio is higher. In two of the clouds we observed, SFO 13 and SFO 37, we do detect HCO^+ ($J = 3 \rightarrow 2$) emission from the tail. And in both of these cases the ratio of head to tail emission is 2, however the presence of an IRAS source within each core implies that star formation is occurring. How do we explain this apparent discrepancy? This is due to the fact that SFO 13 and SFO 37 are two of the most distant sources and as a result beam-dilution is lowering our observed ratio in these sources. The hydrodynamic models were all synthetically observed at a simulated distance of only 400 pc, while SFO 37 is at nearly twice that distance and SFO 13 is at 5 times that distance. One source, SFO 25, has quite a large ratio of head to tail intensity despite being quite a distant source.

Table 4.2. Ratio of core to tail intensity of HCO^+ ($J = 3 \rightarrow 2$) emission

Name	Morphological Type	Intensity Ratio
VC Run F[a]	C	5
VC Run O[b]	C	2
VC Run Q[a]	B	5
VC Run K[b]	A	3
VC Run I[c]	C	2
SFO 4	B	> 2
SFO 13	B	2
SFO 16	A	> 3
SFO 18	A	> 2
SFO 20	C	> 3
SFO 25	B	> 11
SFO 37	C	2

[a]Collapsed to a self-gravitating core.

[b]Did not become self-gravitating.

[c]Formed two self-gravitating cores.

Since we call into question the method of looking for a blue-asymmetric line profile or a blue-bulge signature to find infall regions, it may be worthwhile to investigate this intensity ratio in more detail as a way of finding infalling cores. The method is of limited use however in more complex regions where identifying a tail or a head to a cometary cloud may not be possible.

CHAPTER 5

CONCLUSIONS AND FUTURE WORK

5.1 Conclusions

Our modeling and millimeter and submillimeter observations of bright-rimmed clouds constitute the first detailed combined observational and theoretical study of bright-rimmed clouds. All of the 7 bright-rimmed clouds we observe share morphological similarities to the VC modeled clouds. Among the observed clouds, 6 seem to share traits similar with other low to intermediate mass star forming regions. Our analysis of these bright-rimmed clouds has yielded the principal results that follow.

1. From our models we see that he observed morphologies of bright-rimmed clouds are the result of a evolution from type A through type B to type C as the result of an advancing ionization which sweeps up the molecular gas into a ridge which curves around a molecular cloud core.

2. Our models indicate that bright-rimmed clouds in which the core is gravitationally bound tend to have more ordered centroid velocity gradients than those in which the core is transient.

3. Our synthetic observations of a binary system reveal that even if we observe a bright-rimmed cloud in which a binary system is forming with a telescope beam that does not resolve the system, the line profiles in the direction of the binary system will be more complex than in a core forming only one star.

4. Overall, the line profiles of our modeled bright-rimmed clouds are more symmetric and less self absorbed than in more isolated star forming cores.

5. New FCRAO CO ($J = 1 \rightarrow 0$), $C^{18}O$ ($J = 1 \rightarrow 0$), HCO^+ ($J = 1 \rightarrow 0$), $H^{13}CO^+$ ($J = 1 \rightarrow 0$), and N_2H^+ ($J = 1 \rightarrow 0$) observations along with new HHT CO ($J = 2 \rightarrow 1$), HCO^+ ($J = 3 \rightarrow 2$), HCO^+ ($J = 4 \rightarrow 3$), $H^{13}CO^+$ ($J = 3 \rightarrow 2$), and $H^{13}CO^+$ ($J = 4 \rightarrow 3$) observations of 7 bright-rimmed clouds and 3 Bok globules were presented. These observations constitute the most detailed millimeter and submillimeter study of bright-rimmed clouds to date.

6. The millimeter CO and HCO^+ emission tends to terminate abruptly at the ionization front. As a result, the overall morphology of the CO and HCO^+ millimeter integrated intensity maps are similar with the optical morphologies identified by SFO. These morphologies are also consistent with modeled observations of shock induced collapse (VC).

7. The millimeter HCO^+ tends to show the dense swept up ridge behind the ionization front, as well as the star forming core around the embedded IRAS source. In some of the bright-rimmed clouds the HCO^+ ($J = 1 \rightarrow 0$) emission also traces other overdense clumps which may later be triggered to collapse by the ionization front, resulting in sequential star formation.

8. The millimeter and submillimeter HCO^+ lines from many of the bright-rimmed clouds appear nearly gaussian, with little evidence of infall asymmetry. The only exceptions to this are SFO 18, which shows significant blue asymmetry, and SFO 16 which shows a slight red asymmetry relative to optically thin tracers.

9. The core masses derived for the bright-rimmed clouds using both N_2H^+ and HCO^+ are typical for low and intermediate mass star formation regions. The N_2H^+ and HCO^+ results also tend to agree to within an order of magnitude.

10. The overall blue excess of the sample of bright-rimmed clouds is slightly less than that of the class 0 and class I sources observed by Mardones et al. (1997) and Gregersen et al. (2000), though the small number of bright-rimmed clouds we observed does not make this difference statistically significant. A larger survey of bright-rimmed clouds is required to determine if this is a significant finding. We do however make a case for the fact that the heating of the collapsing cloud by the adjacent HII region could dampen the infall signature, lowering the blue excess of bright-rimmed clouds.

11. We observed outflows around 5 of the 7 bright-rimmed clouds, including new detections of outflows around SFO 13 and SFO 25. These outflows appear to have similar properties to other outflows detected in millimeter and submillimeter emission.

12. The ratio of submillimeter HCO^+ emission from the head of a cometary cloud to its tail is generally higher for clouds which have formed self-gravitating cores than for clouds which have not.

We do not see direct evidence of triggering in these sources. We can not determine if star formation was induced in these clouds or if we are seeing the collapse of pre-existing clumps. We do know that the environment has a profound effect on these regions. Our observations appear morphologically similar to shock-driven collapse models and show a similar reduction in the blue-asymmetric infall signature.

5.2 Future Work

We have completed an extensive modeling and observational program in order to begin to understand star formation in bright-rimmed clouds. This study is a step towards the understanding of star formation in clusters where winds and ionization fronts play an important role. Although this first phase of our research is complete

there is still much work to do to improve our understanding of these regions. Here we summarize the new modeling and observational programs that could improve upon the work described in this thesis.

We have the following modeling priorities.

1. We should apply our radiative transfer models to hydrodynamic models of ionization fronts moving through molecular cloud cores. The VC hydrodynamic models depict the effect of a kinematic shock moving through a cloud, which is not exactly analogous to the regions we observed. We may find noticeable differences between the synthetic observations of kinematically triggered star formation and radiation-driven implosion. The radiation-driven implosion model of Bertoldi (1989) and static cometary cloud model of Bertoldi & McKee (1990) would make good starting points for a theoretical investigation of the differences between kinematic and radiation-driven shocks.

2. We would like to model the effect of increased resolution on our observations of bright-rimmed clouds. Interferometers and larger telescopes may provide the ability to detect centroid velocity gradients or line profile signatures which may help to distinguish cores which are or may become gravitationally bound from those which are not and will not become bound. We also may be able to study binary and sequential star formation is more detail using higher resolution telescopes, but these effects must be modeled.

3. A final improvement we can make in our modeling of the line profiles of model molecular clouds is to employ a three-dimensional Monte Carlo technique to populate the rotational quantum levels. Although our current techniques are computationally inexpensive, they do not accurately model the emission from molecular clouds in which radiation generated in one part of the cloud is absorbed in another part of the cloud. This radiative coupling between regions

in a molecular cloud is ignored in our LVG and LTE models. As computers become more powerful and computing clusters become more prevalent, use of the Monte Carlo technique will become more widespread.

Our observational priorities are as follows.

1. We should increase the number of bright-rimmed clouds we have observed in millimeter and submillimeter molecular lines. Our statistical arguments for the relative lack of infall signatures in bright-rimmed clouds compared to Bok globules is tenuous because they are based on only 7 data points. Further investigation would help us to make more definite and accurate statements regarding the infall asymmetry. A wide range of sources would also help us to get a more general sense of the statistical differences between morphological types. As of right now we have observations of only two to three bright-rimmed clouds in each morphological type and are unable to distinguish the unique properties of individual clouds from the more general properties of that type.

2. We should use current millimeter and submillimeter interferometers to survey more distant bright-rimmed clouds in order to increase our sample. Most of the bright-rimmed clouds are at greater distances from us than Bok globules which have been studied to date. In order to obtain comparable resolution observations of bright-rimmed clouds interferometric maps are required. Interferometric observations may allow us to get a detailed view of the core and in conjunction with our high resolution modeling may provide definitive evidence that triggering is responsible for the collapse of a particular bright-rimmed cloud.

BIBLIOGRAPHY

Anglada, G., Rodríguez, L. F., Canto, J., Estalella, R., & Torrelles, J. M. 1992, ApJ, 395, 494

Bachiller, R. 1996, ARA&A, 34, 111

Bachiller, R. & Pérez Gutiérrez, M. 1997a, in IAU Symp. 182: Herbig-Haro Flows and the Birth of Stars, ed. B. Reipurth & C. Bertout, Vol. 182, 153–162

Bachiller, R. & Pérez Gutiérrez, M. 1997b, ApJ, 487, L93

Beichman, C. A. 1986, in ASSL Vol. 124: Light on Dark Matter, ed. F. P. Israel (Dordrecht: Reidel), 279–292

Benson, P. J., Caselli, P., & Myers, P. C. 1998, ApJ, 506, 743

Benz, W., Bowers, R. L., Cameron, A. G. W., & Press, W. H. 1990, ApJ, 348, 647

Bergin, E. A. & Langer, W. D. 1997, ApJ, 486, 316

Bernes, C. 1979, A&A, 73, 67

Bertoldi, F. 1989, ApJ, 346, 735

Bertoldi, F. & McKee, C. F. 1990, ApJ, 354, 529

Boss, A. P. 1995, ApJ, 439, 224

Boss, A. P. & Foster, P. N. 1997, in Astrophysical Implications of the Laboratory Study of Presolar Materials, ed. T. J. Bernatowicz & E. Zinner (Woodbury: AIP), 649

Cameron, A. G. W., Höflich, P., Myers, P. C., & Clayton, D. D. 1995, ApJ, 447, L53

Cameron, A. G. W. & Truran, J. W. 1977, Icarus, 30, 447

Cameron, A. G. W., Vanhala, H., & Höflich, P. 1997, in Astrophysical Implications of the Laboratory Study of Presolar Materials, ed. T. J. Bernatowicz & E. Zinner (Woodbury: AIP), 665

Carpenter, J. M., Heyer, M. H., & Snell, R. L. 2000, ApJS, 130, 381

Caselli, P., Myers, P. C., & Thaddeus, P. 1995, ApJ, 455, L77

Chandler, C. J., Gear, W. K., Sandell, G., Hayashi, S., Duncan, W. D., Griffin, M. J., & Hazella, S. 1990, MNRAS, 243, 330

Chandler, C. J. & Sargent, A. I. 1993, ApJ, 414, L29

Clemens, D. P. & Barvainis, R. 1988, ApJS, 68, 257

Codella, C. & Bachiller, R. 1999, A&A, 350, 659

Codella, C. & Muders, D. 1997, MNRAS, 291, 337

Cohen, M. 1980, AJ, 85, 29

Duvert, G., Cernicharo, J., Bachiller, R., & Gómez-González, J. 1990, A&A, 233, 190

Elmegreen, B. G. 1992, in Star Formation in Solar Systems III Canary Inslands Winter School of Astrophysics, ed. G. Tenorio-Tagle, M. Prieto, & F. Sánchez (Cambridge: Cambridge University Press), 381

Elmegreen, B. G. 1998, in ASP Conf. Ser. 148: Origins, ed. C. E. Woodward, J. M. Shull, & H. A. Thronson, Jr. (San Fransisco: ASP), 150

Elmegreen, B. G., Efremov, Y., Pudritz, R. E., & Zinnecker, H. 2000, in Protostars and Planets IV, ed. V. G. Mannings, A. P. Boss, & S. S. Russel (Tucson: University of Arizona Press), 179

Evans, N. J. 1999, ARA&A, 37, 311

Flower, D. R. 1999, MNRAS, 305, 651

—. 2001, J. Phys. B., 34, 2731

Forveille, T., Guilloteau, S., & Lucas, R. 1989, CLASS Manual, IRAM

Foster, P. N. & Boss, A. P. 1996, ApJ, 468, 784

—. 1997, ApJ, 489, 346

Fukui, Y. 1989, in ESO Conference and Workshop Proceedings, Vol. 33, Low Mass Star Formation and Pre-main Sequence Objects, ed. B. Reipurth (Garching bei Munchen, F.R.G.: European Southern Observatory), 95

Gregersen, E. M., Evans, N. J., Mardones, D., & Myers, P. C. 2000, ApJ, 533, 440

Hernquist, L. & Katz, N. 1989, ApJS, 70, 419

Heyer, M. H. & Schloerb, F. P. 1997, ApJ, 475, 173

Hodapp, K. & Ladd, E. F. 1995, ApJ, 453, 715

Hogerheijde, M. 1998, PhD thesis, Leiden University

Hogerheijde, M. R. & van der Tak, F. F. S. 2000, A&A, 362, 697

Hogerheijde, M. R., van Dishoeck, E. F., Salverda, J. M., & Blake, G. A. 1999, ApJ, 513, 350

Juvela, M. 1997, A&A, 322, 943

Lada, C. J. 1985, ARA&A, 23, 267

Lada, C. J. & Lada, E. A. 1991, in ASP Conference Series, Vol. 13, The Formation and Evolution of Star Clusters, ed. K. Janes, 3–22

Larson, R. B. 1969a, MNRAS, 145, 271

—. 1969b, MNRAS, 145, 297

Launhardt, R. & Henning, T. 1997, A&A, 326, 329

Lefloch, B. & Lazareff, B. 1994, A&A, 289, 559

—. 1995, A&A, 301, 522

Lefloch, B., Lazareff, B., & Castets, A. 1997, A&A, 324, 249

Lynds, B. T. 1965, ApJS, 12, 163

Mardones, D., Myers, P. C., Tafalla, M., Wilner, D. J., Bachiller, R., & Garay, G. 1997, ApJ, 489, 719

Monaghan, J. J. 1992, ARA&A, 30, 543

Myers, P. C., Heyer, M., Snell, R. L., & Goldsmith, P. F. 1988, ApJ, 324, 907

Narayanan, G. 1997, PhD thesis, University of Arizona

Narayanan, G., Moriarty-Schieven, G., Walker, C. K., & Butner, H. M. 2002, ApJ, 565, 319

Narayanan, G. & Walker, C. K. 1998, ApJ, 508, 780

Narayanan, G., Walker, C. K., & Buckley, H. D. 1998, ApJ, 496, 292

Ogura, K. & Sugitani, K. 1998, Publications of the Astronomical Society of Australia, 15, 91

Ogura, K. & Sugitani, K. 1999, in Star Formation 1999, ed. T. Nakamoto (Nobeyama, Japan: Nobeyama Radio Observatory), 381–382

Park, Y.-S. & Hong, S. S. 1995, A&A, 300, 890

Park, Y.-S., Hong, S. S., & Minh, Y. C. 1996, A&A, 312, 981

Pickett, H. M., Poynter, R. L., Cohen, E. A., Delitsky, M. L., Pearson, J. C., & Müller, H. S. P. 1998, J. Quant. Spec. Radiat. Transf., 60, 883

—. 2000, Submillimeter, Millimeter, and Microwave Spectral Line Catalog, http://spec.jpl.nasa.gov/

Podosek, F. A. & Nichols, R. H. 1997, in Astrophysical Implications of the Laboratory Study of Presolar Materials, ed. T. J. Bernatowicz & E. Zinner (Woodbury: AIP), 617

Pratap, P., Dickens, J. E., Snell, R. L., Miralles, M. P., Bergin, E. A., Irvine, W. M., & Schloerb, F. P. 1997, ApJ, 486, 862

Pudritz, R. E. 2002, Science, 295, 68

Reipurth, B. 1983, A&A, 117, 183

Rybicki, G. B. & Hummer, D. G. 1978, ApJ, 219, 654

Saraceno, P., Andre, P., Ceccarelli, C., Griffin, M., & Molinari, S. 1996, A&A, 309, 827

Scoville, N. Z. & Solomon, P. M. 1974, ApJ, 187, L67

Shu, F. H. 1977, ApJ, 214, 488

Shu, F. H., Adams, F. C., & Lizano, S. 1987, ARA&A, 25, 23

Shu, F. H., Lizano, S., Ruden, S. P., & Najita, J. 1988, ApJ, 328, L19

Snell, R. L. & Loren, R. B. 1977, ApJ, 211, 122

Snell, R. L., Scoville, N. Z., Sanders, D. B., & Erickson, N. R. 1984, ApJ, 284, 176

Stenholm, L. G. & Pudritz, R. E. 1993, ApJ, 416, 218

Sugitani, K., Fukui, Y., Mizuni, A., & Ohashi, N. 1989, ApJ, 342, L87

Sugitani, K., Fukui, Y., & Ogura, K. 1991, ApJS, 77, 59

Sugitani, K. & Ogura, K. 1994, ApJS, 92, 163

Sugitani, K., Tamura, M., & Ogura, K. 1995, ApJ, 455, L39

Sugitani, K., Tamura, M., & Ogura, K. 1999, in Star Formation 1999, ed. T. Nakamoto (Nobeyama, Japan: Nobeyama Radio Observatory), 358–364

Tomita, Y., Saito, T., & Ohtani, H. 1979, PASJ, 31, 407

Truelove, J. K., Klein, R. I., McKee, C. F., Holliman, J. H., Howell, L. H., Greenough, J. A., & Woods, D. T. 1998, ApJ, 495, 821

Turner, B. E. 1995, ApJ, 449, 635

Vanhala, H. A. T., Boss, A. P., Cameron, A. G. W., & Foster, P. N. 1998, in Lunar and Planetary Institute Conference, Vol. 29, 1470

Vanhala, H. A. T. & Cameron, A. G. W. 1998, ApJ, 508, 291

Walker, C. K., Lada, C. J., Young, E. T., & Margulis, M. 1988, ApJ, 332, 335

Walker, C. K., Narayanan, G., & Boss, A. P. 1994, ApJ, 431, 767

Walsh, J. R., Ogura, K., & Reipurth, B. 1992, MNRAS, 257, 110

Ward-Thompson, D. 2002, Science, 295, 76

Yamaguchi, R., Saito, H., Mizuno, N., Mine, Y., Mizuno, A., Ogawa, H., & Fukui, Y. 1999, PASJ, 51, 791

Yun, J. L. & Clemens, D. P. 1992, ApJ, 385, L21

—. 1994, ApJS, 92, 145

Zhou, S. 1992, ApJ, 394, 204

—. 1995, ApJ, 442, 685

Zhou, S., Evans, N. J., Kömpe, C., & Walmsley, C. M. 1993, ApJ, 404, 232

—. 1994, ApJ, 421, 854